Non-equilibrium Superconductivity in THz-driven Two-band Superconductor MgB_2

Dissertation
zur Erlangung des Grades
Doktor der Naturwissenschaften (Dr. rer. nat.)
am Fachbereich Physik, Mathematik und Informatik
der Johannes Gutenberg-Universität Mainz

von:
Sergei Sobolev
geboren in Sankt-Petersburg (Russland)
Mainz, 2023

Sergei Sobolev

Non-equilibrium Superconductivity in THz-driven Two-band Superconductor MgB_2

Datum der mündlichen Prüfung: *25th April 2023*

Gutachter: Aus Datenschutzgründen entfernt / Removed due to data privacy

Kommission: Aus Datenschutzgründen entfernt / Removed due to data privacy

Johannes Gutenberg Universität Mainz
AG Demsar Institut für Physik
Staudingerweg 7
55128, Mainz

EIDESSTATTLICHE ERKLÄRUNG

Hiermit erkläre ich an Eides statt, dass ich meine Dissertation selbständig und ohne fremde Hilfe verfasst und keine anderen als die von mir angegebenen Quellen und Hilfsmittel zur Erstellung meiner Dissertation verwendet habe. Die Arbeit ist in vorliegender oder ähnlicher Form bei keiner anderen Prüfungsbehörde zur Erlangung eines Doktorgrades eingereicht worden.

Mainz, den

Sergei Sobolev

ABSTRACT

The phenomenon of superconductivity has attracted the attention of both the fundamental science community and industry and technology for more than a century. Effects related to the macroscopic manifestation of quantum mechanical order give rise to a better understanding of the processes occurring in the micro-world and lead to new opportunities for applied science such as, for example, creation of the Superconducting QUantum Interference Device [1] – SQUID – allowing for measuring very low magnetic fields, based on Josephson effect. Superconducting electromagnets create extremely high magnetic field and are used in magnetic resonance imaging (MRI) and nuclear magnetic resonance (NMR) machines, fusion reactors such as tokamaks etc.

The experimental studies of superconductivity in the non-equilibrium started soon after the observation of the superconducting energy gap in optical spectroscopy [2] and the development of the microscopic theory of superconductivity by Bardeen, Cooper and Schrieffer [3]. The first experiments were performed in the quasi-continuous excitation regime, without direct access to the dynamics of superconductors [4]. Later on, with the advent of femtosecond laser technology, time-resolved experiments were utilized to investigate the evolution of the optical properties of superconductors on an ultrafast timescale [5].

This thesis presents the results of the studies on the two-band superconductor MgB_2 utilizing time-resolved spectroscopy in the Terahertz (THz) range of electromagnetic radiation. We conducted systematic experiments to obtain the dynamics of the superconducting order in the two-band superconductor MgB_2 as a function of temperature, excitation energy density with the resolution in time- and frequency-domain using different excitation and probing methods.

Our results show that the initial Cooper-pair breaking dynamics driven by the resonant THz excitation exhibits unexpected slowing down on the tens-of-picoseconds timescale implying strongly non-thermal distribution of the photoexcited quasiparticles. The initial suppression of superconductivity is followed by the recovery of the superconducting state, and the recovery dynamics exhibit temperature and absorbed energy density dependence of the recovery time, both for the case of the resonant excitation with intense THz pulses and the off-resonant exci-

tation with near infrared (NIR) laser pulses.

The most non-trivial observation is the temperature dependence of the relative photoinduced gap suppression, which experiences a dip around $0.6 \cdot T_c$ instead of a monotonous increase following the quasi-thermal suppression of the gap. This observation suggests the existence of a process competing with the photoinduced gap suppression, leading to a dynamic "cooling" of a superconductor. Such a process can be a consequence of a non-thermal QP distribution considered by Eliashberg in the 1970's [6]. Compared to the enhancement of superconductivity with microwave radiation, where an increase in T_c of ≈ 1 % was demonstrated, we observe the decrease in the pair-breaking efficiency by a factor of ≈ 2.

The spectrally-resolved conductivity dynamics shows that the technique is sensitive to the spectral features associated with the superconducting gap and can provide rich information about the non-equilibrium optical properties of the superconductor and help to better understand the complex ground state of the multi-band superconductivity. Detailed interpretation of the obtained results, however, requires further theoretical analysis of both equilibrium and non-equilibrium electrodynamics of multi-band superconductors.

KURZFASSUNG

Das Phänomen der Supraleitung zieht, seit seiner Entdeckung vor über einem Jahrhundert, großes Interesse auf sich, sowohl von Grundlagenforschung als auch von Industrie und Technologie. Die Effekte, welche mit der Bildung einer makroskopischen, quantenmechanischen Ordnung einhergehen, bieten nicht nur tiefe Einblicke in Effekte und Mechanismen auf mikroskopischer Ebene, sie ermöglichen ebenso neue Möglichkeiten in der angewandten Wissenschaft. Wie beispielsweise Supraleitende Quanten INterferenc Geräte(/Devices) [1] – SQUIDs –, welche eine Messung kleinster Magnetischer Felder, basierend auf dem Josephson Effekt, erlauben. Ein weiteres Beispiel sind supraleitende Elektromagnete mit ihren extrem starken magnetischen Feldern, welche unter Anderem in Magnetresonanztomographie (MRT) und nuklearer, magnetischer Resonanz (NMR) und Fusionsreaktoren, wie Tokamaks ihre Anwendung finden.

Experimentelle Untersuchungen an Supraleitern im nicht-Gleichgewicht begannen kurz nach der durch optische Spektroskopie entdeckten supraleitenden Energielücke [2] und der Formulierung einer mikroskopischen Theorie durch Bardeen, Cooper und Schrieffer [3]. Die ersten dieser Experimente wurden im quasi-kontinuierlichen Anregungsregime, ohne direkten Zugang zur Dynamik der Supraleiter, durchgeführt [4]. Später, mit dem Aufkommen von Femtosekunden Lasern, konnten Zeitaufgelöste Experimente die Zeitentwicklung der ultraschnellen Dynamiken in Supraleitern zu untersuchen [5].

In dieser Dissertation werden die Ergebnisse von zeitaufgelösten Spektroskopischen Untersuchungen im Terahertzbereich (THz) der elektromagnetischen Strahlung am Zweibandsupraleiter MgB_2 vorgestellt. Wir haben systematische Messungen durchgeführt, um die Dynamiken der Supraleitenden Ordnung des Zweibandsupraleiters MgB_2 als Funktion von Temperatur und Anregungsenergiedichte mit Zeit- und Frequenzauflösung mit verschiedenen Anregungs- und Abfragemethoden analysieren zu können.

Unsere Ergebnisse zeigen, dass die Anfangsdynamik des Brechens der Cooper-Paare im Falle von resonanter THz-Anregung eine unerwartete Verlangsamung auf einer Zeitskala von dutzenden von Pikosekunden hervorruft, was eine starke, nicht-thermische Verteilung der pho-

toinduzierten Quasiteilchen impliziert. Die auf die anfängliche Unterdrückung des supraleitenden Zustandes folgende Erholung zeigt eine Abhängigkeit von Temperatur und absorbierter Energiedichte, sowohl bei resonanter als auch nicht resonanter Anregung mit hochintensiven THz-, sowie NIR (Nah-Infraroten) Pulsen.

Hervorzuheben ist die Beobachtung der Temperaturabhängigkeit der relativen, photoinduzierten Unterdrückung der supraleitenden Energielücke, welche bei ca. 0.6 T_c überraschend absinkt, statt einem der quasi-thermalen Unterdrückung der supraleitenden Energielücke folgenden monotonen Anstieg. Diese Erkenntnis legt die Existenz eines Prozesses nahe, welcher mit der photoinduzierten Unterdrückung der supraleitenden Energielücke wetteifert und so eine Art dynamisches "Abkühlen" des Supraleiters hervorruft. Solch ein Prozess kann eine Konsequenz der nicht-thermalen Quasiteilchenverteilung, wie in den 1970ern von Eliashberg beschrieben, sein [6]. Verglichen mit der Verstärkung der Supraleitung durch Mikrowellenbestrahlung, wo eine Erhöhung der T_c von $\approx 1\%$ gezeigt wurde, beobachten wir eine Verringerung der Effizienz des Cooper-Paar-Brechens um einen Faktor von ≈ 2.

Die frequenzaufgelösten Dynamiken der optischen Leitfähigkeit zeigen, dass mit dieser Technik spektrale Charakteristiken, welche auf die supraleitende Energielücke zurückzuführen sind, betrachtet werden können. Somit können wertvolle Informationen über die optischen Eigenschaften des Supraleiters im nicht-Gleichgewichtszustand gewonnen werden, welche zu einem besseren Verständnis des komplexen Grundzustands der Multiband-Supraleitung beitragen. Eine detaillierte Interpretation unserer Ergebnisse benötigt allerdings weiterführende theoretische Beschreibung der Elektrodynamiken von Multiband-Supraleitern sowohl im Gleichgewicht als auch im nicht-Gleichgewicht.

CONTENTS

List of acronyms

AED	absorbed energy density
ARPES	angle-resolved photoemission spectroscopy
BCS	Bardeen-Cooper-Schrieffer
BPD	balanced photodiode
CP	Cooper pair
DOS	density of states
EO	electro-optic
FEL	free-electron laser
FFT	fast Fourier transform
FWHM	full width at half-maximum
GL	Ginzburg-Landau
HFP	high-frequency phonons
HZDR	Helmholtz Zentrum Dresden - Rossendorf
NIR	near infrared
OAPM	off-axis parabolic mirror
OPTP	optical pump – THz probe
PCA	photoconductive antenna
PP	Pump-Probe
QP	quasiparticle
RT	Rothwarf and Taylor
S/NR	signal-to-noise ratio
STE	spintronic emitter
STS	scanning tunneling spectroscopy
TBR	thermal boundary resistance
THG	third-harmonic generation
THz	Terahertz
THzTDS	Terahertz time-domain spectroscopy
NbTHzPP	narrow-band THz pump – narrow-band THz probe
TPTP	THz pump – THz probe
TFF	thin-film formula
TFM	two-fluid model

INTRODUCTION

> A man goes to knowledge as he goes to war: wide-awake, with fear, with respect, and with absolute assurance. Going to knowledge or going to war in any other manner is a mistake, and whoever makes it might never live to regret it.
>
> C. Castaneda. The Teachings of Don Juan [7]

The world is essentially governed by the peculiar laws of quantum mechanics, but how often this manifestation is observed, or it would be more correct to say, how often do we notice the quantum mechanical nature? The majority of the daily-life phenomena can be described within the deterministic Newton mechanics and even the microscopic processes down to the level of molecules can often be treated classically leaving the quantum-mechanical correlations aside.

However, there are certain phenomena whose properties are essentially macroscopic manifestation of the microscopic quantum mechanical nature. One and perhaps the most famous of such phenomena is the superconductivity. Extensive studies for more than a century showed that the vanishing of electrical resistivity is only the tip of the iceberg containing the rich physics of the phenomenon, together with the perspective technical applications.

Historically, investigation of superconductivity had necessarily required using liquid helium (boiling point of 4.2 K) to reach temperatures below the critical temperature T_c. An increase in T_c by each Kelvin with the discovery of new superconducting compounds counted as an advance. The discovery of high-T_c superconductivity in cuprates, for example, in YBCO with $T_c \approx 90$ K [8], enabled superconducting operation at temperatures above the boiling point of liquid nitrogen (77 K).

Recently, within the studies on superconductivity under high pressures the critical temperature of 250 K was achieved in lanthanum hydride at a pressure of about 170 GPa [9]. Indeed, this discovery spurred people from the scientific community to try their best in the competition for being the first in the search for the room temperature superconductivity [10], which has not

been reliably reported so far.

Within the framework of this thesis, we will (literally) shed light on the superconducting state from the point of view of its dynamics upon ultrafast excitation, both resonantly and off-resonantly with respect to the superconducting gap.

In the Chapter 1 we will start with the relevant theoretical aspects necessary for basic understanding of the superconductivity phenomenon and for interpretation of the experimental data reported in Chapters 3 and 4.

Chapter 2 presents the experimental techniques which are applied for studying the dynamics of a perturbed superconductor. Utilizing THz radiation is the key aspect of the techniques since the superconducting gap in most of the superconductors and particularly the superconductor MgB_2 (which is in the scope of this work) is located in the THz region of electromagnetic radiation. The linear time-domain THz spectrometer can be complemented with resonant and off-resonant excitation schemes providing access to the superconductivity in the out-of-equilibrium.

The experimental results on the energy gap dynamics are represented in the Chapter 3. Using the FEL-based THz pump-probe experimental layout at the large-scale facility Helmholtz Zentrum Dresden - Rossendorf (HZDR) we conducted systematic studies of the dynamics of the superconducting gap in the two-band superconductor MgB_2. The completeness of our data allowed us to reveal the non-trivial behavior of a superconductor upon resonant excitation with THz pulses.

Chapter 4 demonstrates the experimental results on spectrally-resolved optical conductivity dynamics of MgB_2 upon resonant THz and off-resonant NIR ultrafast excitation. Detailed analysis of the obtained results is still in progress and the interpretation of the non-equilibrium optical conductivity, on one hand, will require better understanding of the ground state of the multi-band superconductor while, on the other hand, can help to achieve this understanding.

CHAPTER 1

SELECTED THEORETICAL ASPECTS OF SUPERCONDUCTIVITY

> Well, if everything speaks for an hypothesis and nothing against it – is it then certainly true? One may designate it as such. – But does it certainly agree with reality, with the facts? With this question you are already going round in a circle.
>
> Ludwig Wittgenstein. On Certainty [11]

In this Chapter, the quantum mechanical fundamentals of the microscopic theory of superconductivity will be followed by the aspects relevant to time-resolved/non-equilibrium studies of the phenomenon. The derivations of the main formulas in this Chapter follow those in the Ref. [12].

In 1908, Kamerlingh-Onnes [13] achieved the liquifying of helium – the lightest of the noble gases with the boiling temperature of 4.2 K – which enabled access to the investigation of the material properties at temperatures close to absolute zero, and the temperature dependence of electrical resistance was of great interest among other.

In contrast to common assumptions of that time, the experiment in 1911 showed that electrical resistance of mercury experienced a discontinuity at T = 4.2 K [14] dropping below the noise level. The fact that Kamerlingh-Onnes was awarded by a Nobel prize only 5 years later underlines the importance of this discovery.

1.1 MICROSCOPIC ORIGINS OF SUPERCONDUCTIVITY

The microscopic theory explaining the nature of superconductivity was developed only in 1957 [3], 46 years after the experimental discovery. The theory is based on the observation of the isotope effect and an energy gap in optical spectroscopy. The keystone of the theory was the effect of electrons forming pairs, discovered by Cooper in 1956 [15]. Cooper showed that the behaviour of two electrons, which experience attractive interaction provided by electron-phonon interaction, differs substantially from the other "normal" electrons, fully occupying the Fermi sphere following the Pauli principle. Derivations showed that the two electrons form a bound state, having smaller energy than two uncorrelated electrons, which is separated from the ground state by a binding energy. The energy of the ground state corresponds to the configuration of coupled electrons having antiparallel spin alignment and equal but opposite momenta, thus, forming a coherent state of Cooper pairs.

1.1.1 BARDEEN-COOPER-SCHRIEFFER THEORY

Bardeen, Cooper and Schrieffer generalized the Cooper model for the case, when all the electrons are paired. Then each electron, on the one hand, creates constraints for the allowed values of the wave vectors of other electrons, supporting the pair formation even though the attraction may be weak. On the other hand, each electron itself is a part of a pair.

According to the Bardeen-Cooper-Schrieffer (BCS) theory, half-width of the energy gap at zero temperature limit is defined as:

$$\Delta = 2\hbar\omega_D \; exp\left[-\frac{1}{U \cdot N(E_F)}\right] \tag{1.1}$$

where $U > 0$ is the potential of the electron-phonon interaction, $N(E_F)$ is the density of states (DOS) at the Fermi level and ω_D is the Debye frequency.

From the detailed calculations it follows that the critical temperature T_c (the temperature of the phase transition from normal to superconducting state) is connected to the value of the energy gap as:

$$2\Delta \approx 3.5 k_B T_c \tag{1.2}$$

An interesting observation can be made from equation 1.1 – in normal metals, the conductivity is inversely proportional to the value of U, while in superconductors, the critical temperature increases with U. This implies that some materials being very good metals (in terms of high conductivity) are bad superconductors (in gold or copper superconducting, phase transi-

tion was not observed, in aluminium T_c = 1.2 K). In contrast, some of the bad metals, like Nb or Pb (DC conductivity an order of magnitude lower), have T_c of 9.2 K and 7.2 K, respectively.

The BCS theory implies that in order to create two uncoupled electrons (excited states) in a superconductor a minimum energy of 2Δ must be applied to break a Cooper pair (CP), thus each excitation and a corresponding quasiparticle (QP) will carry energy of at least Δ. The energy of a QP is then given by the following expression:

$$\epsilon_p = \sqrt{\left(\frac{p^2}{2m} - E_F\right) + \Delta^2} \tag{1.3}$$

where E_F is the Fermi energy.

The BCS theory accounts for the electronic spectrum of superconductors, and nearly all the properties of superconductors can be predicted in the framework of this theory. In the case of "conventional" superconductors (with phonon-mediated pairing mechanism), the theory matches the experiment on a qualitative and quantitative level. For the case of high-T_c superconductors (cuprates, pnictides), the pairing mechanism has not yet been established and the quantitative agreement with the BCS-theory is not so good.

1.1.2 A COOPER PAIR

Let us consider interaction of two electrons within a fully occupied Fermi sphere. We can use an analogy of quasiparticles concept used in considering the normal metals. Electron states close to Fermi energy are similar to usual particles so it is natural to measure energies from the Fermi level. The Schrödinger equation for two interacting quasiparticles with equal absolute wave vectors $|\vec{k}|$ reads:

$$[\mathscr{H}_0(\vec{r}_1) + \mathscr{H}_0(\vec{r}_2) + U(\vec{r}_1, \vec{r}_2)]\,\Psi(\vec{r}_1, \vec{r}_2)) = E\Psi(\vec{r}_1, \vec{r}_2)) \tag{1.4}$$

wave function Here $\mathscr{H}_0(\vec{r})$ is a Hamiltonian of a single free particle and the Schrödinger equation for it reads:

$$\mathscr{H}_0(\vec{r})\psi_{\vec{k}}(\vec{r}) = |\xi_{\vec{k}}|\psi_{\vec{k}}(\vec{r}) \tag{1.5}$$

where the wave function for a free particle reads: $\psi_{\vec{k}}(\vec{r}) = V^{-1/2} exp(i\vec{k}\vec{r})$. In the ground state the total momentum and the total spin should be equal to zero so the wave function is

$$\Psi(\vec{r}_1, \vec{r}_2) = V^{-1/2} \sum_{\vec{k}} c_{\vec{k}} \psi_{\vec{k}\uparrow}(\vec{r}_1)\psi_{-\vec{k}\downarrow}(\vec{r}_2) \tag{1.6}$$

Substituting 1.6 to 1.4 we obtain:

$$2|\xi_{\vec{k}}|c_{\vec{k}} + \sum_{\vec{k}'} U_{\vec{k}\vec{k}'} c_{\vec{k}'} = E\, c_{\vec{k}} \tag{1.7}$$

Let us consider the simplest model:

$$U_{\vec{k}\vec{k}'} = \begin{cases} -g \text{ at } k_F - \omega_D/v_F < k, k' < k_F + \omega_D/v_F \\ 0 \text{ outside the interval} \end{cases} . \tag{1.8}$$

describing the attractive potential between two electrons. Introducing the notation

$$I = \sum_{|\vec{k}'|=k_F-\omega_D/v_F}^{|\vec{k}'|=k_F+\omega_D/v_F} c_{\vec{k}'} \tag{1.9}$$

we obtain

$$c_{\vec{k}'} = \frac{gI}{2|\xi_{\vec{k}}| - E} \tag{1.10}$$

Substituting 1.10 into 1.9 we arrive to the self-consistent equation

$$I = \sum_{|\vec{k}'|=k_F-\omega_D/v_F}^{|\vec{k}'|=k_F+\omega_D/v_F} \frac{gI}{2|\xi_{\vec{k}'}| - E} \tag{1.11}$$

We want to find the ground state with *negative* energy (compared to $2E_F$ for two non-interacting electrons). Introducing $E = -2\Delta$ and turning the sum into an integral we obtain

$$1 = gN(E_F) \ln\frac{\hbar\omega_D}{\Delta} \tag{1.12}$$

Hence,

$$\Delta = \hbar\omega_D \exp(-\frac{1}{gN(E_F)}) \tag{1.13}$$

We can see that $\Delta \neq 0$ for any attraction force.

1.1.3 Excitation spectrum

In the Cooper model, the two interacting electrons differ from all other electrons because they form a pair while the rest are considered to be in a non-interacting state. But in reality, one has to consider rearrangement of all electron states. On the one hand, every electron following the Pauli principle creates restrictions for the allowed $\vec{k}$ values of other electrons which allows for

pairing despite the weak attraction. On the other hand, this electron itself is a part of one of these pairs.

To calculate the energy spectrum of elementary excitations we use the second quantization, i.e. occupation numbers representation. The goal is to minimize the free energy. We calculate the ground state energy for the case of attraction between electrons counting their energy from the chemical potential μ, so that $\xi_{\vec{k}} = \frac{\hbar^2 k^2}{2m} - \mu$.

As a Hamiltonian of N electrons in the volume V we choose:

$$\mathscr{H} = \sum_{\vec{k},\sigma} \xi_{\vec{k}} a^+_{\vec{k},\sigma} a_{\vec{k},\sigma} - \frac{1}{2V} \sum_{\vec{k},\vec{k}',\sigma} U_{\vec{k},\vec{k}'} a^+_{\vec{k}',\sigma} a^+_{-\vec{k}',-\sigma} a_{-\vec{k},-\sigma} a_{\vec{k},\sigma} \tag{1.14}$$

where a^+ and a are the creation and annihilation operators, $U_{\vec{k},\vec{k}'}$ is the matrix element of the interaction energy of two electrons. The first term of the Hamiltonian represents the energy of free electrons. The second term is the energy of the interaction between the electrons, where in each term of the sum, two electrons with opposite spins (σ and -σ) and momenta ($\vec{k}$ and -$\vec{k}$) annihilate and two electrons with ($\vec{k}'$ and -$\vec{k}'$) and (σ and -σ) are created.

Given that the terms that differ only in σ contribute equally we can rewrite 1.14

$$\mathscr{H} = 2\sum_{\vec{k}} \xi_{\vec{k}} a^+_{\vec{k},1/2} a_{\vec{k},1/2} - \frac{1}{V} \sum_{\vec{k},\vec{k}'} U_{\vec{k},\vec{k}'} a^+_{\vec{k}',1/2} a^+_{-\vec{k}',-1/2} a_{-\vec{k},-1/2} a_{\vec{k},1/2} \tag{1.15}$$

The problem of defining the ground state and excitation spectrum of the system with Hamiltonian 1.15 can be solved using different methods: Bogoliubov transformation, summation of the Feynman's diagrams, method of spin analogy, etc. Let us use a canonical Bogoliubov transformation introducing the QP operators $A_{\vec{k}0}$, $A_{\vec{k}1}$ defined as:

$$a_{\vec{k},1/2} = u_{\vec{k}} A_{\vec{k}0} + v_{\vec{k}} A^+_{\vec{k}1},\ a_{-\vec{k},-1/2} = u_{\vec{k}} A_{\vec{k}1} - v_{\vec{k}} A^+_{\vec{k}0} \tag{1.16}$$

where $u_{\vec{k}}$ and $v_{\vec{k}}$ are the real functions symmetric with respect to a transformation $\vec{k} \to -\vec{k}$. For all Fermi-operators the transposition relations for anticommutators must be satisfied: $\{a^+_i a_k\} = \delta_{ik}, \{a_i a_k\} = \{a^+_i a^+_k\} = 0$, and similarly for A. These requirements are fulfilled if

$$u^2_{\vec{k}} + v^2_{\vec{k}} = 1 \tag{1.17}$$

Then 1.15 is transformed into

$$\mathscr{H} = E_0 + \mathscr{H}^0_0 + \mathscr{H}_1 + \mathscr{H}_2, \tag{1.18}$$

where

$$E_0 = 2\sum_{\vec{k}} \xi_{\vec{k}} v^2_{\vec{k}} - \frac{1}{V} \sum_{\vec{k},\vec{k}'} U_{\vec{k},\vec{k}'} u_{\vec{k}'} v_{\vec{k}'} u_{\vec{k}} v_{\vec{k}} \tag{1.19}$$

is the constant term independent of the Fermi-operators and corresponding to the ground state energy;

$$\mathscr{H}_0^0 = \sum_{\vec{k}} \left[\xi_{\vec{k}}(u_{\vec{k}}^2 - v_{\vec{k}}^2) + \frac{2u_{\vec{k}}v_{\vec{k}}}{V} \sum_{\vec{k}'} U_{\vec{k},\vec{k}'} u_{\vec{k}'} v_{\vec{k}'} \right] (A_{\vec{k}0}^+ A_{\vec{k}0} + A_{\vec{k}1}^+ A_{\vec{k}1}) \tag{1.20}$$

is the diagonal part of the Hamiltonian;

$$\mathscr{H}_1 = \sum_{\vec{k}} \left[2\xi_{\vec{k}} u_{\vec{k}} v_{\vec{k}} + \frac{1}{V}(u_{\vec{k}}^2 - v_{\vec{k}}^2) \sum_{\vec{k}'} U_{\vec{k},\vec{k}'} u_{\vec{k}'} v_{\vec{k}'} \right] (A_{\vec{k}0}^+ A_{\vec{k}0} + A_{\vec{k}1}^+ A_{\vec{k}1}) \tag{1.21}$$

is the off-diagonal part of the Hamiltonian containing products of two Fermi-operators. The operator $\mathscr{H}_2$ contains products of four new Fermi-operators and may be neglected, when considering low-energy excitation limit.

We can choose $u_{\vec{k}}$ and $v_{\vec{k}}$ so that 1.21 equals to zero, then the following condition must be fulfilled:

$$2\xi_{\vec{k}} u_{\vec{k}} v_{\vec{k}} = \frac{1}{V}(u_{\vec{k}}^2 - v_{\vec{k}}^2) \sum_{\vec{k}'} U_{\vec{k},\vec{k}'} u_{\vec{k}'} v_{\vec{k}'} \tag{1.22}$$

This equation is also a condition of the minimum of the ground state energy if 1.17 is fulfilled. Let us introduce a notation

$$\Delta_{\vec{k}} = \frac{1}{V} \sum_{\vec{k}'} U_{\vec{k},\vec{k}'} u_{\vec{k}'} v_{\vec{k}'} \tag{1.23}$$

Then combining 1.17 and 1.22 we can express $u_{\vec{k}}$ and $v_{\vec{k}}$ via $\xi_{\vec{k}}$ and $\Delta_{\vec{k}}$:

$$u_{\vec{k}}^2 = \frac{1}{2}\left[1 + \frac{\xi_{\vec{k}}}{\sqrt{\xi_{\vec{k}}^2 + \Delta_{\vec{k}}^2}}\right] \; ; \; v_{\vec{k}}^2 = \frac{1}{2}\left[1 - \frac{\xi_{\vec{k}}}{\sqrt{\xi_{\vec{k}}^2 + \Delta_{\vec{k}}^2}}\right] \tag{1.24}$$

Substituting 1.24 into 1.22 we obtain a non-linear self-consistent equation for $\Delta_{\vec{k}}$:

$$\Delta_{\vec{k}} \equiv \frac{1}{2V} \sum_{\vec{k}'} \frac{U_{\vec{k}\vec{k}'} \Delta_{\vec{k}'}}{\sqrt{\xi_{\vec{k}'}^2 + \Delta_{\vec{k}'}^2}} \tag{1.25}$$

Substituting 1.23 and 1.24 into 1.20 we convert the diagonal part of the Hamiltonian as:

$$\mathscr{H}_0^0 = \sum_{\vec{k}} \sqrt{\xi_{\vec{k}}^2 + \Delta_{\vec{k}}^2} (A_{\vec{k}0}^+ A_{\vec{k}0} + A_{\vec{k}1}^+ A_{\vec{k}1}) \tag{1.26}$$

Thus, due to the interaction of electrons with each other their excitation spectrum has the form:

$$\epsilon_{\vec{k}} = \sqrt{\xi_{\vec{k}}^2 + \Delta_{\vec{k}}^2} \tag{1.27}$$

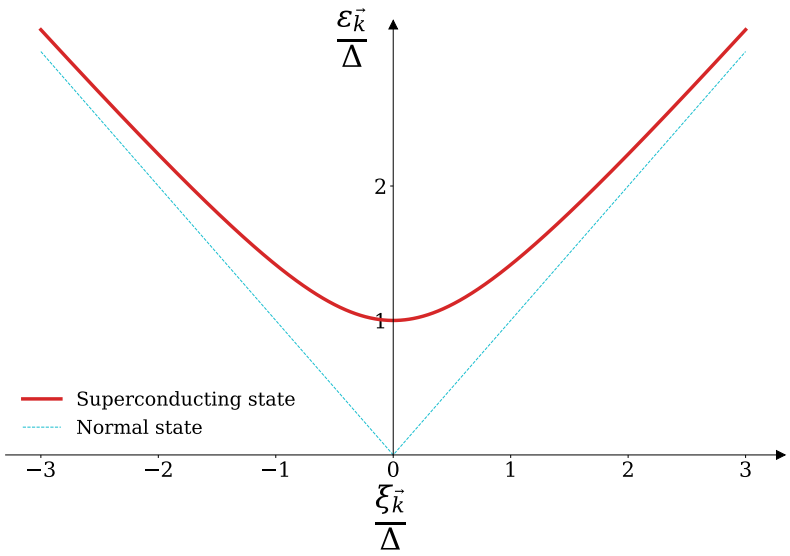

Figure 1.1: Dispersion of elementary excitation for normal and superconducting states.

The energy of an elementary excitation has a minimum value equal to Δ, corresponding to an energy gap in the excitation spectrum (Fig. 1.1).

Each value of momentum $\vec{k}$ corresponds to two types of excitations related with creation operators $A^{+}_{\vec{k}0}$ and $A_{\vec{k}1}$. The change in the single-particle spectrum caused by interaction is governed by $\Delta_{\vec{k}}$, a root of equation 1.25.

Equation 1.25 has a trivial solution $\Delta_{\vec{k}} = 0$ corresponding to the normal state. Let us consider the other solutions for the simplest case we already introduced:

$$U_{\vec{k}\vec{k}'} = \begin{cases} -g \text{ at } k_F - q < k, k' < k_F + q \\ 0 \text{ outside the interval} \end{cases} . \tag{1.28}$$

In this case, following from equation 1.25, within the specified interval, $\Delta_{\vec{k}}$ is constant ($\Delta_{\vec{k}} = \Delta$) and equation 1.25 can be simplified to:

$$1 = \frac{g}{2} \sum_{\vec{k}} \frac{1}{\sqrt{\xi^2_{\vec{k}} + \Delta^2}} \tag{1.29}$$

Assuming the chemical potential equal to $\mu = E_F = \frac{\hbar^2 k_F^2}{2m}$ we obtain

$$\xi_{\vec{k}} = \frac{\hbar^2 (k^2 - k_F^2)}{2m} \approx \hbar^2 k_F (k - k_F)/m \tag{1.30}$$

Let $\delta \equiv k - k_F$, then replacing the sum with an integral, according to $\sum_{\vec{k}} ... = (2\pi)^{-3} \int ... d^3k$, and for spherical Fermi surface with $d^3\vec{k} = 4\pi k_F^2 dk$ equation 1.29 reads:

$$1 = \frac{g k_F^2}{4\pi} \int_{-q}^{q} \left[\Delta^2 + \left(\frac{\hbar^2 k_f}{m} \delta \right)^2 \right]^{-1/2} d\delta \tag{1.31}$$

Calculating the integral and resolving the equation for Δ, we obtain

$$\Delta = \frac{2\hbar^2 k_F q}{m \left(exp\left[\frac{1}{gN(E_F)} \right] - 1 \right)} \tag{1.32}$$

where $N(E_F) = \frac{m k_F}{2\pi^2 \hbar^2}$ is the DOS at the Fermi level.

Maximum change of the electron wave vector, q, corresponds to maximum (Debye) frequency of the virtual phonon ω_D: $q = \frac{\omega_D}{v_F}$. In the weak coupling limit $gN(E_F) << 1$ we finally obtain:

$$\Delta(T=0) = 2\hbar\omega_D exp\left(-\frac{1}{gN(E_F)} \right) \tag{1.33}$$

It is getting clear why the theory of superconductivity could not have been created within the perturbation theory formalism to account for interactions. The perturbation theory provides corrections to the energy in the form of degrees of small interaction energy g, while the obtained value of Δ tends to zero as $exp\left(-\frac{1}{gN(E_F)}\right)$ and at small values of g cannot be expanded in series.

In order to find out the physical meaning of Δ, let us express the ground state energy E_0 by substituting 1.23 and 1.24 into 1.19:

$$E_0 = \sum_{\vec{k}} \frac{\xi_{\vec{k}} \left(\sqrt{\xi_{\vec{k}}^2 + \Delta_{\vec{k}}^2} - \xi_{\vec{k}} \right) - \Delta_{\vec{k}}^2 / 2}{\sqrt{\xi_{\vec{k}}^2 + \Delta_{\vec{k}}^2}}. \tag{1.34}$$

The trivial solution $\Delta_{\vec{k}} = 0$ corresponds to normal state with $E_0 = 0$. If $\Delta_{\vec{k}} \neq 0$ the ground state energy $E_0 < 0$ which is energetically more favorable than the normal state. Replacing the sum with an integral one can obtain that the energy difference between the superconducting and normal state equals $N(E_F)\Delta^2/2$, this quantity is called condensation energy.

With $\Delta_{\vec{k}} \neq 0$, the functions $u_{\vec{k}}$ and $v_{\vec{k}}$ simultaneously differ from zero, and the fermionic operators A_0^+ and A_1^+ correspond to creation of new elementary excitations (QPs). Here, the values $u_{\vec{k}}$ and $v_{\vec{k}}$ characterize the probabilities of different states: $u_{\vec{k}}^2$ is the probability that in the absence of excitations the electronic states with $\vec{k}$ and $-\vec{k}$ are simultaneously unoccupied, and $v_{\vec{k}}^2 = \frac{1}{2}\left[1 - \frac{\xi_{\vec{k}}}{\sqrt{\xi_{\vec{k}}^2 + \Delta_{\vec{k}}^2}} \right]$ is the probability of $\vec{k}$ and $-\vec{k}$ states being occupied.

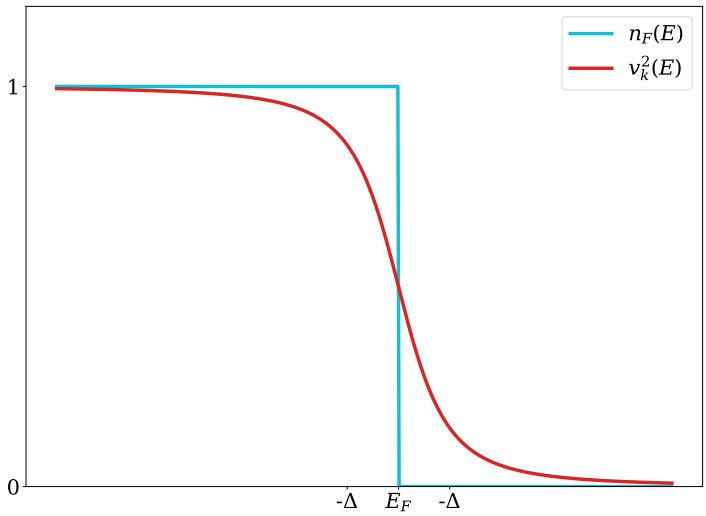

Figure 1.2: Energy distribution of occupation probability for single electron state in a normal metal and in the ground state of a superconductor.

Now we can find the momentum and energy distribution of QPs. Upon transition from normal state to the superconducting state the amount of electrons in the volume V remains conserved but these electrons do not fill the Fermi sphere anymore. Cyan line in the Figure 1.2 shows the probabilities of occupation of the single-electron state with energy E in the normal metal; red curve depicts $v_{\vec{k}}^2$ – the probability of occupying the states with $\vec{k}$ and $-\vec{k}$ in the ground state of a superconductor. We can see that inside the energy gap single-electron states of a superconductor are occupied. In other words, the gap exists in the energy of elementary excitations and not in the energy of single-electron states.

Let us find the DOS in the excitation spectrum of a superconductor, i.e. the amount of QP states per unit energy. Excitation states of a normal state are rearranged in the superconductor due to the presence of the gap. Given, that the total amount of states is conserved we can write:

$$N_n \, d\xi_{\vec{k}} = N_s \, d\epsilon_{\vec{k}} \tag{1.35}$$

Using 1.27 and assuming the DOS in the normal state close to the Fermi level is constant we obtain

$$N_s(\epsilon) = N(E_F) \, \frac{\epsilon}{\sqrt{\epsilon^2 - \Delta^2}} \tag{1.36}$$

As mentioned above, we neglected the operator $\mathscr{H}_2$ containing the product of four QP

Fermi-operators. This assumption is valid if the amount of excitations is small. However if the temperature is not equal to zero, the $\mathscr{H}_2$ operator must be taken into account (that is why in 1.33 Δ, is given in the zero temperature limit). The strict calculation yields the expressions:

$$2\xi_{\vec{k}}\, u_{\vec{k}}\, v_{\vec{k}} = (u_{\vec{k}}^2 - v_{\vec{k}}^2)\Delta \tag{1.37}$$

$$\Delta = g\sum_{\vec{k}'} u_{\vec{k}}\, v_{\vec{k}}(1 - n_{\vec{k}0} - n_{\vec{k}1}) \tag{1.38}$$

Equation 1.38 shows that the value of the energy gap Δ depends on the number of QPs and their distribution function. Let us calculate the temperature dependence of Δ. The QPs are distributed according to Fermi-Dirac statistics:

$$n_{\vec{k}'} = \frac{1}{exp(\epsilon_{\vec{k}} \,/\, k_B T) + 1} \tag{1.39}$$

Substituting 1.37 and 1.39 into 1.38 and proceeding to integral form we obtain:

$$1 = \frac{gN(E_F)}{2}\int_0^{\hbar\omega_D} \frac{tanh\frac{\sqrt{\xi^2+\Delta^2}}{2k_BT}}{\sqrt{\xi^2+\Delta^2}} d\xi \tag{1.40}$$

The temperature dependence $\Delta(T)$ calculated according to formula 1.40 is represented in Fig. 1.3. Remarkably, the value of the ratio $\frac{\Delta(T=0)}{k_B T_c} \approx 3.5$ (already introduced in Section 1.1.1, equation 1.2) is independent of the material properties being a characteristic invariant for BCS superconductors.

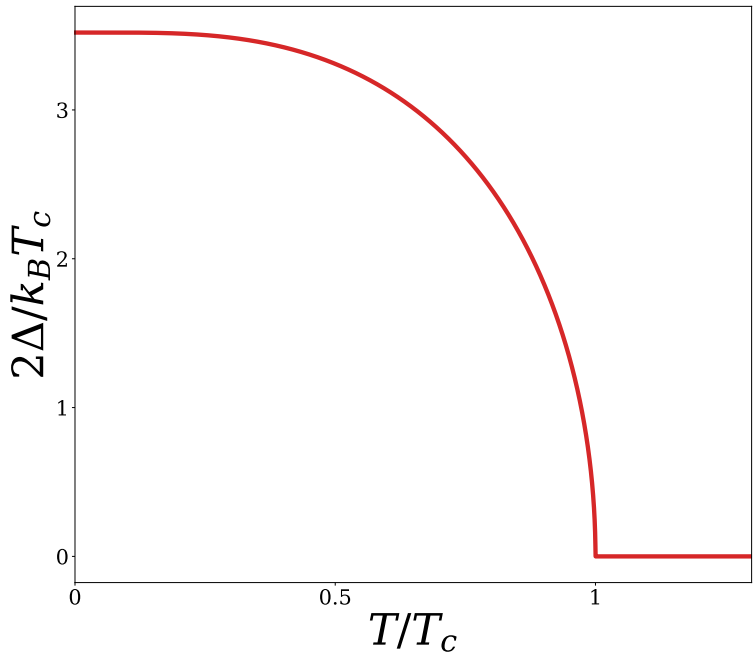

Figure 1.3: Temperature dependence of the energy gap in a BCS superconductor.

1.2 TWO TYPES OF SUPERCONDUCTIVITY

In 1935, 20 years before the microscopic BCS theory Fritz and Heinz London showed [16] that in the limit of low fields and currents slowly changing in space, the minimum free energy condition leads to a simple relation between fields and currents. The London theory was based on a two-fluid model, elaborated below in Section 1.4.2, assuming existence of two types of electrons – "normal" with concentration $n_n(T)$ and "superconducting" with concentration $n_s(T)$. The supercurrent is then provided by the non-dissipative motion of superconducting electrons, the rest behave in a usual way.

Let us consider a clean metal with parabolic conduction band; the effective mass of electrons equals to m^*. The free energy then reads:

$$F = \int F_s dV + E_k + E_m \tag{1.41}$$

where F_s is the electron energy in the ground state (per unit volume), E_k – kinetic energy corresponding to supercurrents, E_m – energy corresponding to the magnetic field. The drift velocity of the electrons in the position $\vec{r}$ is expressed via current density $\vec{j}_s$ as follows:

$$n_s \cdot e \cdot \vec{v}(\vec{r}) = \vec{j}_s(\vec{r}) \tag{1.42}$$

The kinetic energy is then:

$$E_k = \frac{1}{2}\int n_s m^* v^2 dV \tag{1.43}$$

Expression 1.43 is valid if $\vec{v}(\vec{r})$ is a slowly changing function of coordinates.

The energy related to the magnetic field $\vec{h}(\vec{r})$ can be expressed as follows (with magnetic permeability equal to 1):

$$E_m = \frac{\mu_0}{2}\int h^2 dV \tag{1.44}$$

Maxwell equation defines the relation between magnetic field $\vec{h}(\vec{r})$ and supercurrent density:

$$\vec{\nabla} \times \vec{h} = \vec{j}_s \tag{1.45}$$

Now, using 1.43 – 1.45 the free energy reads:

$$F = F_0 + \frac{\mu_0}{2}\int \left(h^2 + \lambda_L^2 |\vec{\nabla} \times \vec{h}|^2\right) dV \tag{1.46}$$

where $F_0 = \int F_s dV$ and λ_L having a dimension of length is defined as[1] :

$$\lambda_L \equiv \sqrt{\frac{m^*}{\mu_0 n_s e^{*2}}} \tag{1.47}$$

Let us consider a superconductor to be infinite in the direction of the applied magnetic field and minimize the free energy F from 1.46 with respect to the field distribution $\vec{h}(\vec{r})$. With the magnetic field change of $\delta\vec{h}(\vec{r})$ the change in the free energy δF reads:

$$\delta F = \mu_0 \int \left(\vec{h} \cdot \delta\vec{h} + \lambda_L^2\, \vec{\nabla} \times \vec{h} \cdot \vec{\nabla} \times \delta\vec{h}\right) dV = \mu_0 \int \left(\vec{h} + \lambda_L^2\, \vec{\nabla} \times\ \vec{\nabla} \times \vec{h}\right) \delta\vec{h}\, dV \tag{1.48}$$

Hence, the field configuration yielding minimum of the free energy must satisfy the equation:

$$\vec{h} + \lambda_L^2\, \vec{\nabla} \times\ \vec{\nabla} \times \vec{h} = 0 \tag{1.49}$$

[1]The Londons assumed that the supercurrent is formed by single electrons. However, later on it turned out that the electrons are paired, hence in the equation 1.47 $m^* = 2m_e, e^* = 2e, n_s = n/2$. Substituting these values into 1.47 does not change the result though. For simple metals like Al, Sn etc. $\lambda_L \approx 0.05\ \mu$m

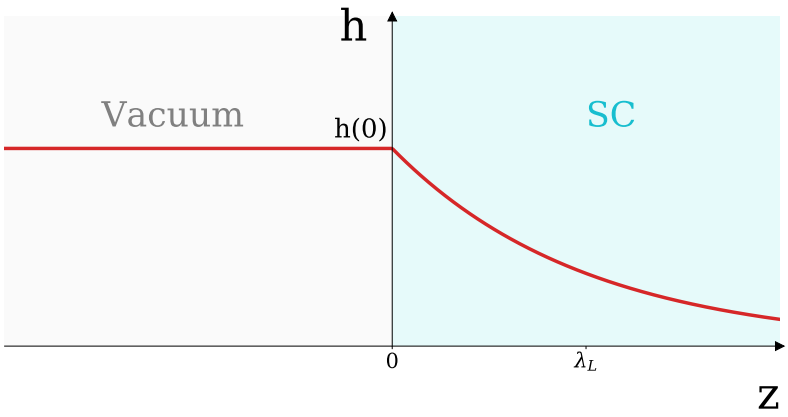

Figure 1.4: Exponential decay of the external magnetic field at the vacuum/SC interface, with the external magnetic field parallel to the surface. λ_L is the penetration depth.

It can be rewritten using Maxwell equation 1.45 as follows:

$$\vec{\nabla} \times \vec{j} = -\frac{\vec{h}}{\lambda_L^2} \tag{1.50}$$

Equation 1.49 or 1.50 is called the London equation. Let us now apply this equation to the case of the magnetic field trying to penetrate into the superconductor. In the simplest geometry where the surface of the superconductor coincides with the xy plane and the semi-space $z < 0$ is empty the magnetic field $\vec{h}$ and supercurrent density $\vec{j}_s$ are the 1D functions of z. From 1.50 follows that $h_z = 0$ (since $\vec{j}_s$ is independent on x and y). Let us choose the direction of the applied magnetic field along x axis. From the Maxwell equation $\vec{\nabla} \times \vec{h} = \vec{j}_s$ it follows that $\vec{j}_s$ is parallel to the y axis: $dh/dz = j_s$.

Finally, the equation 1.49 gives:

$$\frac{d^2h}{dz^2} = \frac{h}{\lambda_L^2} \tag{1.51}$$

Finite solution of this equation inside the superconductor reads:

$$h(z) = h(0) \cdot exp\left(-\frac{z}{\lambda_L}\right), \tag{1.52}$$

i.e. magnetic field exponentially decays in the superconductor with the characteristic length-scale λ_L called the penetration depth (Fig. 1.4). Given that λ_L is small, one can say that magnetic field is expelled from the macroscopic sample leading to the Meissner effect.

The derivation of London equations was carried out under an assumption of $\vec{j}(\vec{r})$ "slowly" changing in space. Let us now elaborate this point. In a condensed system the velocities of two electrons are correlated if the distance between them is smaller than certain quantity, let us call this distance ξ_0. To estimate ξ_0 we note that the area of substantial momentum values of electrons in a superconductor is given by:

$$E_F - \Delta < \frac{p^2}{2m} < E_F + \Delta, \tag{1.53}$$

where E_F is the Fermi energy and Δ is the energy gap.

Corresponding range of momenta equals $\delta p = 2\Delta/v_F$, where $v_F = p_F/m$ is the electron Fermi velocity. From the uncertainty principle we can estimate spatial dimension of the wave packet $\delta x \approx \hbar/\delta p$. Thus, a characteristic length can be introduced called a coherence length:

$$\xi_0 = \frac{\hbar v_F}{\pi\Delta} \tag{1.54}$$

Thus, the validity criteria for London equations is $\lambda_L >> \xi_0$. The superconductors for which the London equation is valid, i.e. $\lambda_L >> \xi_0$, are called historically the superconductors of the second type. In simple metals penetration depth λ_L is small (tens of nanometers) while the Fermi velocity is high (thousands of km/s) and hence, ξ_0 is also a large number – for aluminum $\xi_0 = 1$ μm. In the case of $\lambda_L << \xi_0$ the London equation 1.50 must be replaced by a more complicated form put forward by Pippard. The superconductors obeying this condition are the superconductors of the first type.

1.3 GINZBURG-LANDAU THEORY

In 1950 Ginzburg and Landau came up with an approach to treat superconductivity based on a theory of second order phase transitions put forward by Landau earlier [17]. In this theory, no heat absorption or generation occurs upon such a phase transition. Instead, Landau introduced a quantity – the order parameter – that gradually decreases to zero as the temperature increases to critical value T_c. As an order parameter in a superconductor Ginzburg and Landau considered a wave function $\psi(\vec{r})$ such that $|\psi(\vec{r})|$ equals concentration of superconducting electrons. The Ginzburg-Landau (GL) theory is a phenomenological approach valid when $T \rightarrow T_c$.

To start with, let us consider the superconducting free energy F_s in the case of zero external magnetic field and ψ being independent on coordinates. F_s can be expanded as powers of $|\psi|$:

$$F_s = F_N + \alpha|\psi|^2 + \frac{1}{2}\beta|\psi|^4 + ... \tag{1.55}$$

where F_N is the normal state free energy. When the temperature equals T_c the order parameter $\psi\Big|_{T=T_c} = 0$, thus, the free energy equals that of the normal state.

When $T < T_c$ α must be negative because the energy of the superconducting state F_s must be less than F_N. From the same considerations, α must be positive above T_c which implies that $\alpha\Big|_{T=T_c} = 0$.

The transition point must be stable, i.e. with α=0 the free energy $F(|\psi|)\Big|_{\psi=0}$ must have minimum. This implies that the third order term in Taylor expansion must be equal to zero and the fourth order term (third term in Eq. 1.55) must be positive implying that $\beta > 0$.

Close to T_c we can limit the expansion to $|\psi|^4$. Then coefficients α and β can be expressed via a thermodynamical critical field B_c and CP density $n_s(\infty) = |\psi_\infty|^2$ at large enough distance from the boundary considering that $F_N - F_s = \frac{\mu_0 H_c^2}{2}$ [4]:

$$F_s - F_N = \alpha|\psi_\infty|^2 + \frac{1}{2}\beta|\psi_\infty|^4 = -\frac{1}{2\mu_0}B_c^2 \tag{1.56}$$

The second equation for α and β we can obtain from the condition of minimum of F_s in equilibrium $\frac{\partial F_s}{\partial|\psi|^2} = 0$ which results in:

$$\alpha + \beta|\psi_\infty|^2 = 0 \tag{1.57}$$

Solving these coupled equations we find:

$$\alpha = -\frac{1}{\mu_0}\frac{B_c^2}{n_s(\infty)} \tag{1.58}$$

$$\beta = \frac{1}{\mu_0}\frac{B_c^2}{n_s^2(\infty)} \tag{1.59}$$

To gain further insight let us now allow for the order parameter to change slowly in space. In this case, additional terms will appear in free energy F_s (1.55): $\frac{1}{2m^*}|(-i\hbar\vec{\nabla} - e^*\vec{A})\psi|^2$ and $\frac{B^2}{2\mu_0}$, where $m^* = 2m_e$ and $e^* = 2e$ – mass and charge of a CP. The first term corresponds to the kinetic energy when replacing momentum of particle by the generalized momentum in the magnetic field with vector potential $\vec{A}$. The second term corresponds to the energy of the magnetic field.

The distribution of the magnetic field, with given external currents, can be found by minimizing the thermodynamical Gibbs potential $G_s = (F_s - BH) - (-\frac{B_{ext}^2}{2\mu_0})$, where B_{ext} is the external magnetic field. For the case of an infinite superconducting rod and magnetic field applied along its axis the expression for G_s reads:

$$G_s = F_N + \alpha|\psi|^2 + \frac{1}{2}\beta|\psi|^4 + \frac{(B-B_{ext})^2}{2\mu_0} + \frac{1}{2m^*}|(-i\hbar\vec{\nabla} - e^*\vec{A})\psi|^2 \tag{1.60}$$

Integrating over the sample volume and minimizing the result with respect to ψ and $\vec{A}$ by means of variational method we come to the GL equations:

$$\alpha\psi + \beta|\psi|^2\psi + \frac{1}{2m^*}|-i\hbar\vec{\nabla} - e^*\vec{A}|^2\psi = 0 \tag{1.61}$$

$$\vec{j}_s = \frac{e^* i\hbar}{2m^*}\left(\psi\vec{\nabla}\psi^* - \psi^*\vec{\nabla}\psi\right) - \frac{e^{*2}}{m^*}|\psi|^2\vec{A} \tag{1.62}$$

Let us show that equations 1.61–1.62 contain two characteristic parameters with a dimension of length. At first, we consider the case of absent currents and magnetic fields. We choose the gauge when $\psi(\vec{r})$ is real and consider one-dimensional case for simplicity. Then equation 1.61 reads:

$$\alpha\psi + \beta\psi^3 - \frac{\hbar^2}{2m^*}\frac{d^2\psi}{dx^2} = 0 \tag{1.63}$$

This equation has two obvious solutions: 1) $\psi = 0$ describing the normal state; 2) $\psi^2 = \psi_0 = -\frac{\alpha}{\beta}$ corresponding to the superconducting state. The second solution exists and corresponds to a lower energy when $\alpha < 0$, i.e. $T < T_c$.

In a more general case $\psi(x)$ can differ from ψ_0 at a certain point in space. Let us find $\psi(x)$ in the vicinity of this point.

Introducing the dimensionless variable $f = \psi/\psi_0$ and the notion $\xi^2(T) \equiv \frac{\hbar^2}{2m^*|\alpha|}$, where $\xi(T)$ has a dimension of length, the equation 1.63 reads

$$-f + f^3 - \xi^2(T)\frac{d^2 f}{dx^2} = 0 \tag{1.64}$$

Thus, $\xi(T)$ is a characteristic length-scale of changes in the function f. It can be also called a coherence length for a given temperature T. One can show that for clean metals

$$\xi(T) \approx 0.74\left(1 - \frac{T}{T_c}\right)^{-0.5}\xi_0\,, \tag{1.65}$$

where ξ_0 is defined by the equation 1.54.

Another characteristic length shows up if we consider effects of magnetic field penetration into the superconductor. If the applied field is small, $|\psi|^2$ can be replaced by $|\psi_0|^2$ for the absent field. Applying $\vec{\nabla}\times$ operator to the 2$^{\text{nd}}$ GL equation 1.62 and considering that $\vec{\nabla}\times\vec{A} = \mu_0\vec{h}$, we come to the London-type equation because ψ_0 is independent on coordinates:

$$\vec{\nabla} \times \vec{j} = -\frac{e^{*2}}{m^*}\psi_0^2 \mu_0 \vec{h} \tag{1.66}$$

From equation 1.66 and London equation 1.50 one can obtain, for the case of a clean metal:

$$\lambda(T) = \sqrt{\frac{m^*}{\mu_0 n_s e^{*2}}} = \frac{1}{\sqrt{2}} \left(1 - \frac{T}{T_c}\right)^{-0.5} \lambda_L \tag{1.67}$$

where $\lambda_L = \sqrt{\frac{m}{\mu_0 n e^2}}$ is the London penetration depth.

The two characteristic lengths $\xi(T)$ and $\lambda(T)$ for $T \to T_c$ scale as $(T_c - T)^{-0.5}$ hence their T-independent ratio $K = \frac{\xi(T)}{\lambda(T)}$, called Ginzburg-Landau parameter, is a characteristic for a given material. Depending on the value of K superconductor can be of either first ($\lambda < \frac{1}{\sqrt{2}}\xi$) or second ($\lambda > \frac{1}{\sqrt{2}}\xi$) type.

1.4 ELECTRODYNAMICS OF SUPERCONDUCTORS

Here we will discuss theoretical basics of the electrodynamics of superconductors. We start with the Drude-model, describing the complex conductivity in metals on a classical level, and extend it for the case of a superconductor in the two-fluid model (TFM) approximation. Later on we present analytical description of optical conductivity $\tilde{\sigma}(\omega)$ derived in the BCS framework.

1.4.1 THE DRUDE MODEL

Three years after discovery of an electron Paul Drude came up with the first, indeed purely classical, model of motion of electrons in a metal which could well account for the DC and AC electrical conductivity, Hall effect and thermal conductivity [18]. Electrons in a metal are considered as classical particles forming an electron gas. Each electron is supposed to move along straight lines between the collision events, whilst each collision results in change of the electron speed – similarly to the kinetic gas theory.

Electrical conductivity is governed by an important parameter of the model – the scattering rate τ^{-1} – the inverse mean time between the collision events. The current response of a metal to an AC electric field as a function of frequency is a complex value called AC or optical conductivity, and is given by the following expression:

$$\tilde{\sigma}(\omega) \equiv \sigma_1(\omega) - i\sigma_2(\omega) = \frac{\sigma_0}{1 + i\omega\tau} \tag{1.68}$$

where $\sigma_0 = \frac{ne^2\tau}{m^*}$ with n being the concentration of electrons, e and m^* are the charge and (effective) mass of the electron.

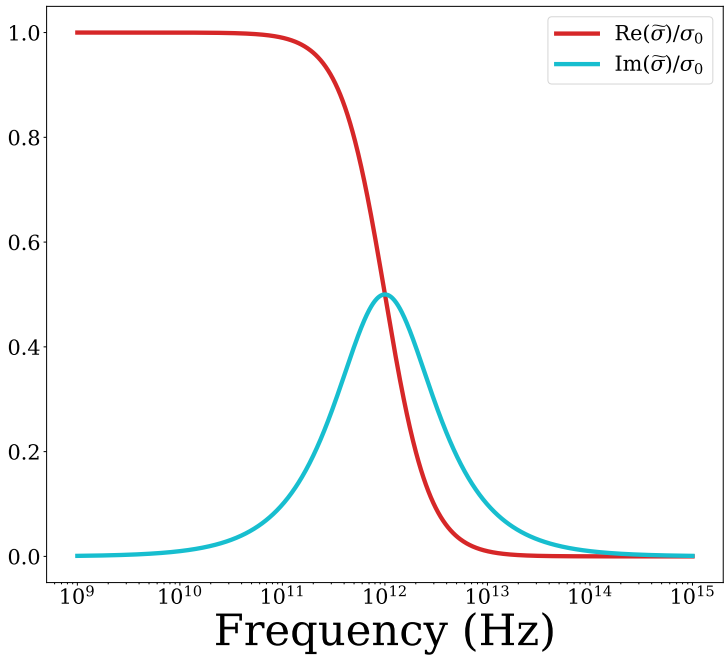

Figure 1.5: Real and imaginary part of the optical conductivity as a function of frequency for $\tau^{-1} = 1$ THz in the simple Drude model with the scattering rate and mass being independent on frequency.

The frequency dependence of real part, σ_1, and imaginary part (taken with negative sign) σ_2 of the optical conductivity is represented in Fig. 1.5.

1.4.2 THE TWO-FLUID MODEL

The very basic approach to treat electrodynamics of a superconductor is a model where the total electron density n is assumed to split into n_s and n_n, the densities of superconducting and normal electrons correspondingly. These electrons are supposed to possess different Drude scattering rates τ_s^{-1} and τ_n^{-1} and the AC-response $\tilde{\sigma}^s(\omega)$ and $\tilde{\sigma}^n(\omega)$. In the simplest case one assumes $\tau_s \to \infty$, then in DC response $\sigma_1^s(\omega = 0) \to \infty$ while the AC part of σ_1^s tends to zero at lower and lower frequency giving rise to a δ-function-like frequency dependence. The imaginary part of the optical conductivity σ_2^s is equivalent to the first London equation [4, 16].

Indeed, this model applies to frequencies below the energy gap, and usually, in this case an assumption $\omega\tau_n << 1$ is also valid. Then the response of a superconductor in a two-fluid model reads:

$$\sigma_1(\omega) = \sigma_1^s + \sigma_1^n = \frac{\pi}{2}\frac{n_s e^2}{m^*}\delta(\omega) + \frac{n_n e^2 \tau_n}{m^*} \tag{1.69}$$

$$\sigma_2(\omega) = \frac{n_s e^2}{m^* \omega} \tag{1.70}$$

This approximation provides qualitative description of a superconducting response to the applied electric field (within the specified limitations). It was put forward decades before the microscopic theory of superconductivity but still can serve as a starting framework for the basic understanding of the electromagnetic response.

1.4.3 OPTICAL CONDUCTIVITY CALCULATION WITHIN THE BCS THEORY

Mattis and Bardeen [19] derived the equations for the frequency dependent optical conductivity of a superconductor in the framework of a BCS theory for frequencies comparable to $\Delta/\hbar$ assuming the "dirty"-limit superconductor with scattering rate $\tau^{-1} \to \infty$ and $l << \xi_0, \lambda$ where l is a mean-free path. In the zero-temperature limit the derived expressions have an analytic form:

$$\frac{\sigma_1}{\sigma_N} = \left(1 + \frac{2\Delta}{\hbar\omega}\right) E(k) - 2\left(\frac{2\Delta}{\hbar\omega}\right) K(k) \tag{1.71}$$

$$\frac{\sigma_2}{\sigma_N} = \frac{1}{2}\left[\left(\frac{2\Delta}{\hbar\omega} + 1\right) E(k') + \left(\frac{2\Delta}{\hbar\omega} - 1\right) K(k')\right] \tag{1.72}$$

where $K(k)$ and $E(k)$ are the complete elliptical integrals of the 1st and 2nd kind respectively and k and k' read:

$$k = \left|\frac{2\Delta - \hbar\omega}{2\Delta + \hbar\omega}\right|, \quad k' = \sqrt{1 - k^2}$$

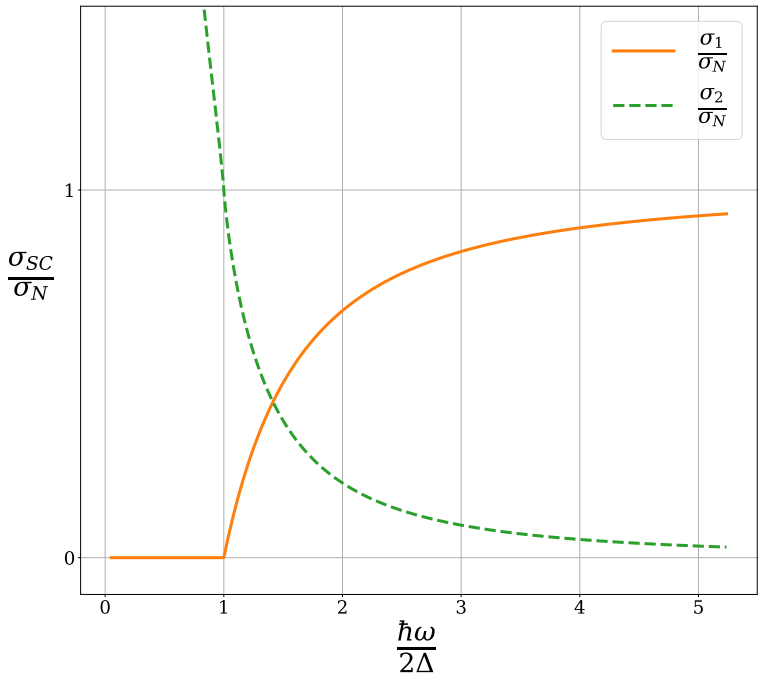

Figure 1.6: Real and imaginary part of the optical conductivity of a superconductor at T=0, given by Mattis-Bardeen formulas for a dirty-limit superconductor.

Fig. 1.6 shows the calculated frequency dependence of σ_1 and σ_2 normalized to the corresponding normal state optical conductivity (in the zero temperature limit). In the low-frequency region equations are similar to the two-fluid approximation. However, for the electromagnetic field frequencies above 2Δ the absorption (indicated by an increase in σ_1) takes place caused by breaking of CPs.

The Mattis-Bardeen expressions have been extended for the case of arbitrary τ^{-1} 30 years later by Zimmerman [20].

1.5 MULTI-BAND SUPERCONDUCTIVITY: THE CASE OF MgB_2

In the conventional BCS theory discussed in Section 1.1.1 electron-phonon interaction is assumed to be constant over the Fermi surface, implying a single energy gap, and in many materials this assumption is valid. However, any good rule has its exclusions, and the BCS theory is not an exception. If the material a) possesses several electronic bands crossing the Fermi energy, b) the critical temperature of the superconducting phase transition is finite and c) the coupling

between the bands is weak, several energy gaps can be observed. Studies on several compounds – pnictides [21], Kagome superconductors [22], Chevrel phases [23] – showed opening of a superconducting gap in multiple electronic bands giving rise to intriguing phenomena. One of such materials, being in the scope of this dissertation is the magnesium diboride (MgB_2), a BCS superconductor with exceptionally high T_c = 39 K having two superconducting gaps in π and σ bands of boron [24–26]. The main evidence of the phonon-mediated mechanism of superconductivity – the isotope effect – was confirmed in MgB_2 [27, 28].

Experimental data, obtained in the scanning tunneling spectroscopy (STS) [29] shown in Fig. 1.7, panels **a** and **b**, reveal the two energy gaps (Δ_π= 2.2 meV, $\Delta_\sigma \approx$7 meV) in MgB_2. The gap in the σ-band is present only in the spectra with the tunneling current, perpendicular to the c-axis of the crystal. In particular, this means that coupling to the two-dimensional σ-band is highly suppressed for tunneling parallel to the c-axis, whereas the 3D π-band can be observed for all tunneling directions.

The electronic structure of MgB_2 in the superconducting state was studied using angle-resolved photoemission spectroscopy (ARPES) [30] soon after discovery of superconductivity in this material. These studies clearly showed the existence of the two-band superconductivity in MgB_2, the superconducting gaps in σ and π bands were separately observed. ARPES spectra in the vicinity of Fermi energy, E_F, for temperatures below and above T_c are presented in Fig. 1.7**c**. The sizes of the σ and π gaps were estimated by numerical fitting the spectrum using the BCS spectral function, resulting in $\Delta_\sigma = 6.5 \pm 0.5$ meV and $\Delta_\pi = 1.5 \pm 0.5$ meV.

In a number of studies [30–35] utilizing theoretical and experimental methods the values of both gaps and their temperature dependence were evaluated. Remarkably, in all the studies both gaps close in a second order phase transition fashion with the single T_c, implying the presence of a finite coupling between the two bands. Fig. 1.8 represents Δ_σ (green) and Δ_π (red) as a function of reduced temperature T/T_c. The temperature dependence of the gaps is obtained using the BCS formula with $\Delta_\pi(T=0)$ = 2.1 meV, $\Delta_\sigma(T=0)$ = 7.2 meV. These values are the average values of the gaps from several references [32, 33, 35].

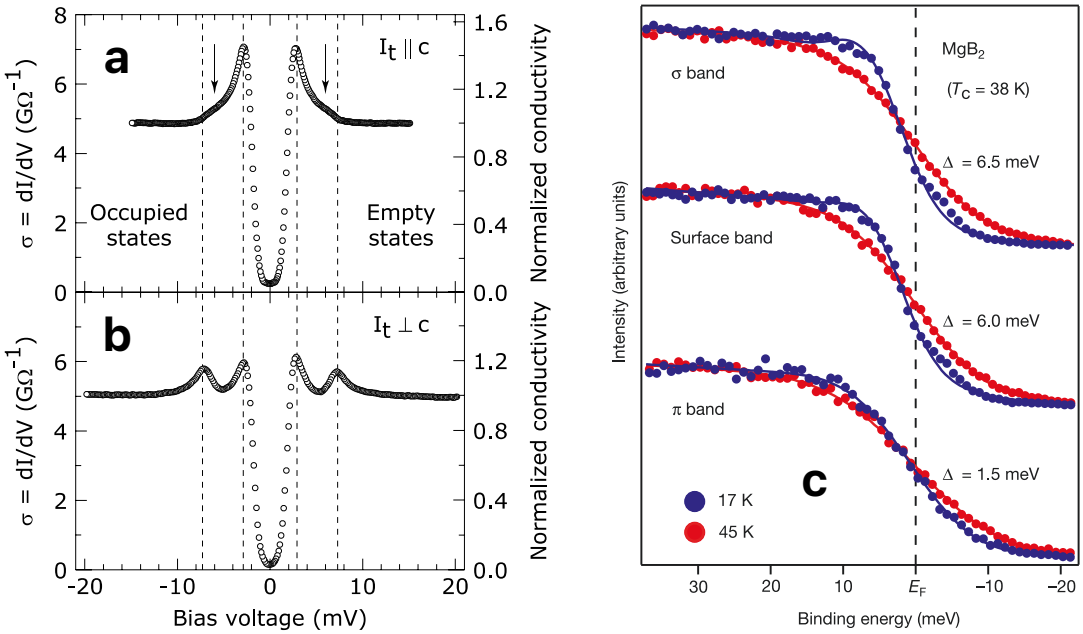

Figure 1.7: Left panels: Zero-field superconducting spectra of MgB_2 obtained in STS. **a** parallel and **b** perpendicular to the c-axis at T = 0.3 K. In the direction of the tunneling current, perpendicular to the c-axis (panel **b**), both superconducting gaps are clearly visible, shown by the dashed lines. Reprinted from [29], with permission from Elsevier. **c** Temperature dependence of ARPES spectra near E_F of MgB_2 at three values of the wave vector, corresponding to the σ-band, the surface band and the π-band. Measurements were done at 17 K (blue circles) and 45 K (red circles), with blue and red lines on the spectra showing the results of numerical fitting [30]. Reproduced with permission from Springer Nature.

Because of two bands involved in superconductivity the electron-phonon coupling constant turns into 2×2 matrix:

$$\begin{pmatrix} \lambda_{\pi\pi} = 0.448 & \lambda_{\pi\sigma} = 0.213 \\ \lambda_{\sigma\pi} = 0.155 & \lambda_{\sigma\sigma} = 1.017 \end{pmatrix} \tag{1.73}$$

and the total $\lambda = 0.87$; the values are the results of calculation reported in Ref. [36]. Clearly, the electron-phonon coupling is stronger for σ-band, weaker for π-band and even weaker, but not negligible, between the two bands.

Time-domain THz spectroscopy provides access to the optical conductivity in the THz range, and the opening of a superconducting gap can be observed directly. In the early time-resolved experiments, the dynamics of the order parameter in MgB_2, following the femtosecond NIR excitation, was studied in both optical-probe and THz-probe configuration [37].

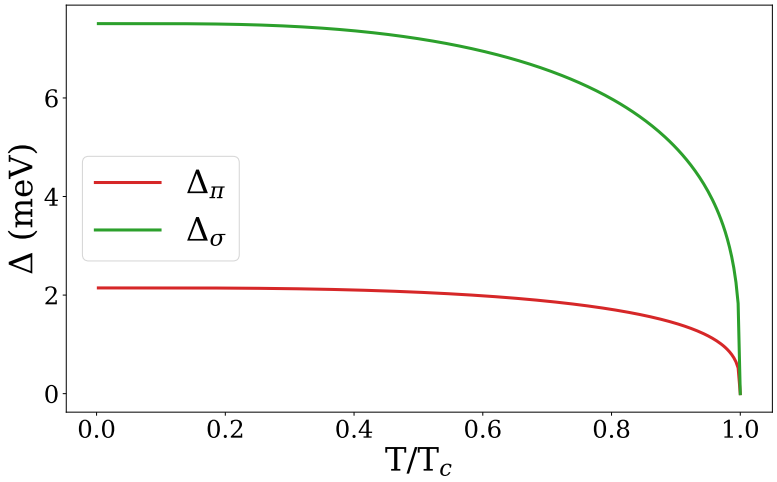

Figure 1.8: Temperature dependence of superconducting gaps in MgB_2, the temperature axis is normalized to T_c. Δ_π(T=0) = 2.1 meV, Δ_σ(T=0) = 7.2 meV. Remarkably, both gaps close at single T_c, implying finite coupling between the two bands.

The photoinduced pair-breaking shown in Fig. 1.9a was found to be temperature-dependent and excitation energy density dependent, with the pair-breaking process being faster upon increasing of either of these two parameters. Such dependence is a strong evidence of the pair-breaking process dynamics being governed by energy exchange between QPs and high-frequency phonons on the picosecond timescale. For comparison, the pair-breaking dynamics in a single-gap superconductor NbN is depicted in panel 1.9b.

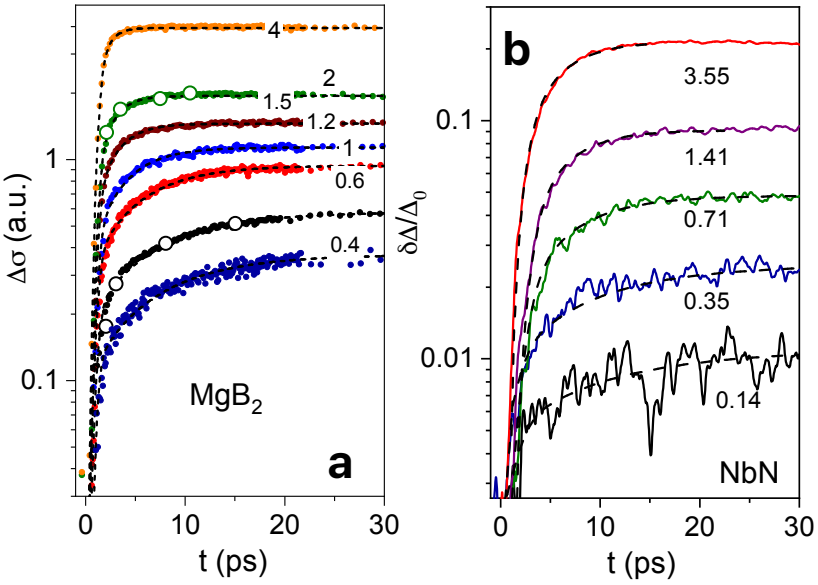

Figure 1.9: **a** Superconducting state depletion dynamics in MgB_2 taken at various excitation densities (in $\mu J/cm^2$) at 7 K [37]. **b** Superconducting depletion dynamics, shown as the relative change of the gap, $\delta\Delta/\Delta_0$, recorded at 4.3 K on NbN film for various excitation densities in mJ/cm^3 at 4.3 K. The experimental methods will be elaborated in Chapter 2.

Interesting effects compared to single-gap superconductors can be considered in the context of two (coupled) order parameters $\Psi_\pi = \Delta_\pi e^{i\Theta_\pi}$ and $\Psi_\sigma = \Delta_\sigma e^{i\Theta_\sigma}$ with, in general, non-zero phase difference $\Theta = \Theta_\pi - \Theta_\sigma$. A collective excitation, the so-called *Leggett mode* [38], can occur due to fluctuations of Θ.

The frequency of the Leggett mode can be calculated via electron-phonon coupling constants and values of the two gaps [39]:

$$\omega_0^2 = \frac{\lambda_{\pi\sigma} + \lambda_{\sigma\pi}}{\lambda_{\pi\pi}\lambda_{\sigma\sigma} - \lambda_{\pi\sigma}\lambda_{\sigma\pi}} 4\Delta_\pi\Delta_\sigma \tag{1.74}$$

For the case of MgB_2 using electron-phonon coupling constants from Ref. [36] and values of $\Delta_\pi = 2$ meV and $\Delta_\sigma = 7.5$ meV the Leggett mode frequency is $\hbar\omega_0 = 7.2$ meV. Experimentally, the emergence of the Leggett mode below T_c was observed in MgB_2 using polarized Raman spectroscopy [40]. A broad peak around 9.4 meV implies a short lifetime of the Leggett mode. In another work [41] authors used intense THz pulses to trigger Raman-like collective excitations which can be attributed to the Leggett mode. The Leggett mode frequency at low temperature was discovered to be $\sim$ 2.5 THz (10.4 meV) matching the previous experimental results and theoretical estimates.

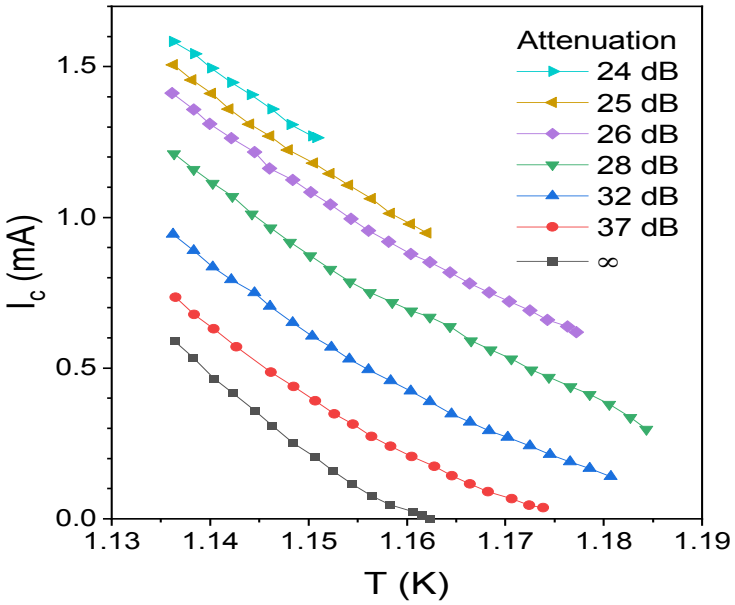

Figure 1.10: Temperature dependence of the critical current in Al for various levels of microwave power at 3 GHz (attenuations are shown on the plot, with ∞ corresponding to the absence of microwave radiation). The presented data were adapted from Ref. [5].

1.6 NON-EQUILIBRIUM SUPERCONDUCTIVITY

In this Section we will briefly review the behaviour of a superconductor beyond equilibrium: upon irradiating with sub-gap electromagnetic radiation (microwaves) (Section 1.6.1) and following an ultrafast excitation (Section 1.6.4), i.e. when the electronic state of a superconductor is changed using external perturbation. We present relevant models describing the superconductor in non-equilibrium that are used in Chapter 3 for analyzing and interpreting the experimental data and performing the supplemental simulations.

A non-equilibrium state may occur in a superconductor upon external perturbation, and in the case of perturbation with electromagnetic radiation, two scenarios can be realized. If the photon energy $\hbar\omega_{ph}$ is bigger than the energy gap 2Δ, direct absorption will take place since the photon energy is enough to break a CP with creation of two QPs. However, if the $\omega_{ph} > 2\Delta/\hbar$ no direct absorption of the incident photon can occur. The studies on conventional superconductors such as Al and Sn upon irradiation with microwaves showed [42–44] that an increase in critical current and T_c can be observed (Fig. 1.10), even though the effect was small – in equilibrium in aluminum T_c = 1.17 K and upon irradiation with continuous radiation at the frequency of 3 GHz the critical temperature increased to 1.184 K [44].

1.6.1 ELIASHBERG MECHANISM OF SUPERCONDUCTIVITY ENHANCEMENT

Following experimental studies [42] on microwave stimulated enhancement of superconductivity, Eliashberg [6] considered effects of non-thermal QP distribution included in the self-consistent gap equation

$$\Delta = g \int_{\Delta}^{\hbar\omega_D} d\epsilon \frac{\Delta}{\sqrt{\epsilon^2+\Delta^2}} \left[1-2f(\epsilon)\right] \tag{1.75}$$

which defines the dependence of the energy gap Δ on the distribution function $f(\epsilon)$. In equilibrium the QP distribution function obeys Fermi-Dirac statistics: $f(\epsilon) = \frac{1}{e^{\epsilon/k_B T}+1}$. Electromagnetic field with angular frequency $\omega < 2\Delta/\hbar$ being absorbed by elementary excitations (QPs) shifts the $f(\epsilon)$ towards higher ϵ while keeping the total number of excitations unchanged. Such a shift, according to 1.75, will lead to an increase of Δ. Actual change in $n(\epsilon)$ will be proportional to electromagnetic field intensity E^2 (if E is not too big) and inversely proportional to the QP relaxation time τ_0.

In general, upon applied electromagnetic field Δ is a time-dependent quantity. However, for frequencies of interest, the amplitude of gap oscillation is significantly less than the averaged over time amplitude $\langle\Delta\rangle_t$ [45]. Under this assumption, the goal is to define $f(\epsilon)$ in the presence of the electromagnetic field. In the case of moderate field intensity, it is enough to take into account second order terms of potential $A(t) = A_\omega cos(\omega t)$. As a result, the equation for the averaged Δ reads [6]:

$$\left\{\frac{T_c-T}{T} - \frac{7\zeta(3)}{8(\pi T_c)^2}\Delta^2 - \frac{\pi}{6T_c}\frac{l\ v\ e^2}{\hbar c^2}\left[A_0^2 + \frac{A_\omega^2}{2}\left(1-\frac{\hbar\omega}{2\pi\gamma}f(\frac{\hbar\omega}{\Delta})\right)\right]\right\}\Delta = 0 \tag{1.76}$$

where l is the mean free path, A_0 is the potential representing constant magnetic field or current, $\gamma = \hbar\tau_0^{-1}$. The function $f(\frac{\hbar\omega}{\Delta})$ is complicated and in the two limiting cases reads [6]:

$$f(u) \approx u ln\frac{8}{u},\ \ u << 1 \tag{1.77}$$

$$f(u) \approx \frac{\pi}{u},\ \ u >> 1 \tag{1.78}$$

$$\tag{1.79}$$

where $u = \frac{\hbar\omega}{\Delta}$. As one can see from 1.76 and 1.77, the alternating field will lead to an increase in Δ if $\omega > \omega_c$, where ω_c reads:

$$\omega_c^2 ln\frac{8\Delta}{\hbar\omega_c} = \frac{2\pi}{\hbar^2}\gamma\Delta \tag{1.80}$$

The change in the gap as a result of changes in the QP distribution can be expressed as follows [46]:

$$\frac{\delta\Delta}{\Delta_0} \approx -C \int_{\Delta}^{\hbar\omega_D} d\xi \frac{\delta f(\xi)}{\sqrt{\xi^2+\Delta_0^2}} \tag{1.81}$$

where C is a positive dimensionless constant that generally depends on temperature. An increase in the gap $\delta\Delta > 0$ may be observed if the QPs at the gap edge are transferred to higher energies.

It should be noted, however, that there is a natural limitation for a possible increase of Δ – a redistribution of thermally excited QPs that leads to an enhancement of the gap with alternating electromagnetic field takes place at finite temperatures, i.e., if the thermally-excited QPs are already present.

1.6.2 SUPERCONDUCTING GAP DYNAMICS IN NBN DRIVEN BY PHOTOEXCITATION

The investigation of non-equilibrium properties of a superconductor can be performed using an ultrafast excitation to perturb the studied system. In the work [47] authors studied the time-resolved dynamics of the energy gap in NbN, which is a BCS superconductor with the T_c = 15.4 K. The optical pump - THz probe spectroscopy was utilized, resulting in the time evolution of the superconducting state as a function of time delay between the optical pump pulse and the THz probe pulse or of the spectrally-resolved dynamics of optical conductivity over a large range of temperatures and excitation densities.

It was demonstrated that the pair-breaking process and the recovery of the superconducting state depend on the excitation density following the Rothwarf-Taylor model, elaborated below. Extracting the microscopic parameters allowed to determine the electron-phonon constant for this material in good agreement with the literature value. The time evolution of the superconducting obtained in optical pump - THz probe spectroscopy is presented in Fig. 1.11.

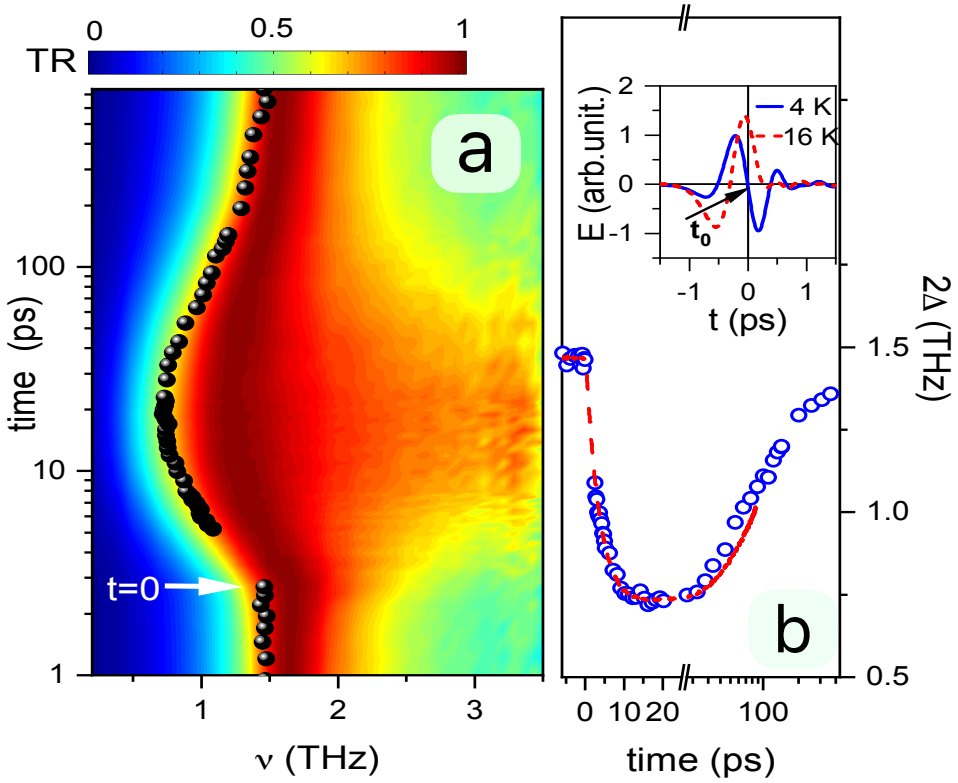

Figure 1.11: **a** The time evolution of the gap (black spheres), determined at each time delay from $\Delta\sigma(\omega,t)$. The contour-plot presents the corresponding ratio of the spectral THz transmission in the superconducting and normal state. **b** The gap dynamics, obtained from the spectrally-resolved conductivity (open circles) and using spectrally integrated approach (red dashed line). The experimental methods will be elaborated in Chapter 2. The presented data were adapted from Ref. [5].

1.6.3 ROTHWARF-TAYLOR MODEL

Upon excitation in the so-called energy-mode (i.e. charge-neutral), e.g., with photons having $\omega_{ph} > 2\Delta/\hbar$, the pair-breaking process builds up with generation of QPs. Two excited QPs can relax back to the superconducting condensate (Fi) releasing their energy to one phonon with $\omega_b > 2\Delta/\hbar$ (Fig. 1.12a). In turn, this high-frequency phonons (HFP) can break one CP, resulting in again creation of two QPs (Fig. 1.12b). However, if the HFP experiences an anharmonic decay creating phonons with $\omega_b < 2\Delta/\hbar$(Fig. 1.12c), it cannot break CPs anymore and take part in the bi-particle energy exchange.

The model, accounting for the interplay between excited QPs and HFPs ($\Omega_{phonon} > 2\Delta/\hbar$) in the case of above-gap photoexcitation, was proposed by Rothwarf and Taylor (RT) [48]. A

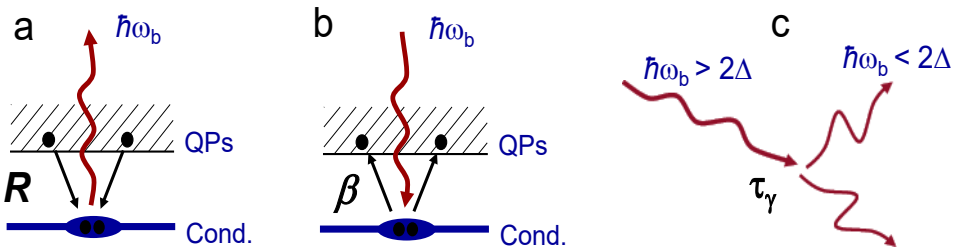

Figure 1.12: Different processes governing the relaxation dynamics of photo-excited QPs in a superconductor: **a** recombination of two QPs into the condensate via emission of 2Δ boson (phonon), **b** pair-breaking by absorption of a boson, **c** decay of high energy bosons. The latter can proceed via decay of bosons into the (dielectric) substrate of via anharmonic decay into low-energy bosons, with energy less than 2Δ.

set of two coupled differential equations for QP density n and HFP density N can describe the dynamics of an excited superconductor:

$$\frac{dn}{dt} = Q_0 \cdot \delta(t) + \beta N - Rn^2 \tag{1.82}$$

$$\frac{dN}{dt} = P_0 \cdot \delta(t) - \beta\frac{N}{2} + R\frac{n^2}{2} - \gamma(N - N_T)\,. \tag{1.83}$$

Here β is the probability of pair-breaking via absorption of HFP, R is the bare QP recombination rate with creation of HFP, Q_0 and P_0 are the initial QP and HFP densities, N_T is the concentration of HFPs at temperature T in thermal equilibrium and γ is their decay rate. There are two possible channels of HFPs decay: via anharmonic decay to low-frequency ($\omega < 2\Delta$) phonons that do not have enough energy to break CPs [49] or by diffusion HFPs into the substrate [50]. As it will be shown below, R and β (namely, their ratio) are the microscopic parameters that govern the dynamics of a superconductor on the ultrafast timescale.

If the decay of HFPs is the limiting factor that governs the recovery of superconductivity the so-called phonon-bottleneck scenario [48] is realized. In the first approximation, when considering only rise-time dynamics – initial stage of superconductivity quenching upon photoexcitation – the decay of HFPs may be neglected. Then, we may drop the last term in Eq. 1.82 and reduce the equations to:

$$\frac{dn}{dt} = Q_0 \cdot \delta(t) + \beta N - Rn^2 \tag{1.84}$$

$$\frac{dN}{dt} = P_0 \cdot \delta(t) - \beta\frac{N}{2} + R\frac{n^2}{2} \tag{1.85}$$

Here, $Q_0 \cdot \delta(t)$ and $P_0 \cdot \delta(t)$ reflect the quasi-instantaneous excitation of the system. The early stage of relaxation of superconducting system, following the perturbation, will result in thermalization of QPs and HFPs reaching a quasi-equilibrium state characterized by the effective temperature T^*. This T^* model was originally proposed by Parker [51] in 1975, within the framework of his modified heating theory developed to interpret the experimental results on out-of-equilibrium superconductivity [52–55]. The HFPs (which are relevant to the dynamics of QPs) in this model are assumed to have similar temperature with QPs, i.e. temperature T^*, while the low-frequency phonons with $\Omega_{phonon} < 2\Delta/\hbar$, being unable to break CPs, are assumed to be a "cold" bath characterized by the ambient temperature T. This allows one to treat a photoexcited superconductor as a superconductor with a quasi-temperature T^* *at every moment in time* with an assumption $T^* = T^*(t)$ is indeed relevant in the case of ultrafast photo-excitation. While such an approximation may not be valid on the sub-ps timescale, it was shown to describe the dynamics of conventional superconductors like NbN on the picosecond timescale [47].

The detailed balance conditions of the photoexcited superconductor are then $Rn^2_{T^*} = \beta N_{T^*}$ [5]. The thermal densities of QPs and HFPs can be found from the following expressions [56]:

$$n_T \approx N(0)\sqrt{2\pi\Delta k_b T}\, exp\left(-\frac{\Delta}{k_b T}\right) \tag{1.86}$$

$$N_T = \frac{36\nu\Delta^2 T}{\omega_D^3} exp\left(-\frac{2\Delta}{k_b T}\right) \tag{1.87}$$

Given that the exponential factor in the HFP density (1.87) is 2 times larger than in the equation for QP density, 1.86, in equilibrium at $T \to 0$ most of the energy is in the QP channel. From the balance condition $Rn^2 = \beta N$ it follows that the ratio $\frac{\beta}{R}$ is a characteristic concentration.

Introducing the reduced QP and HFP concentrations $q \equiv Rn/\beta$ and $p \equiv RN/\beta$ and time in the units of inverse HFP relaxation rate: $\Theta = \beta t$ we transform Eq. 1.84 to the form [57]:

$$\frac{dq}{dt} = p - q^2 \tag{1.88}$$

$$\frac{dp}{dt} = -\frac{p}{2} + \frac{q^2}{2} \tag{1.89}$$

with initial conditions $q(0) = q_0$ and $p(0) = p_0$. These coupled equations 1.88 can be solved analytically yielding the time evolution of (reduced) QP and HFP concentration $q(\Theta)$ and $p(\Theta)$ following the photoexcitation [37, 57]. We focus our attention on the dynamics of QP density because it is directly related to the dynamics of the superconducting energy gap, which is a topic of the thesis.

The analytic solution for $q(\Theta > 0)$ reads with an assumption $\gamma \to 0$ (see 1.82):

$$q(\Theta) = -\frac{1}{4} - \frac{\xi^{-1}}{2} + \frac{\xi^{-1}}{1 - Kexp(-\Theta/\xi)}, \tag{1.90}$$

where $\xi^{-1} = \sqrt{1/4 + 4p_0 + 2q_0}$ and $K = \frac{4q_0+1-2\xi^{-1}}{4q_0+1+2\xi^{-1}}$ are the dimensionless parameters expressed via initial conditions $[q_0, p_0]$. For $\Theta \to \infty$ (and neglecting decay of the photoexcitated state) $q^2(\infty) = p(\infty)$ and $q(\infty) = \sqrt{1/16 + q_0 + p_0/2} - 1/4$.

We can assume that initial amount of energy right after the photoexcitation on QP and HFP systems can be described by

$$q_0 = \frac{R}{\beta}\frac{Ap}{\Delta} \tag{1.91}$$

$$p_0 = \frac{R}{\beta}\frac{A(1-p)}{2\Delta}, \tag{1.92}$$

where A is the absorbed energy density, and p is the fraction of energy initially going to the QP system. The dynamics of QP density following the photoexcitation and the initial avalanche process giving rise to an excess densities pf QPs and HFPs are represented in Fig. 1.13. The microscopic parameters, used in the simulation, are: A = 1 mJ/cm^3, Δ = 2 meV, N(E_F) = 0.67 states·eV^{-1}u.c.V^{-1}, β^{-1} = 50 ps, R = 100 ps^{-1} u.c.V. Here u.c.V is the unit cell volume of MgB_2 equal to 29 Å^3 [58]).

1.6.4 TRANSIENT ENHANCEMENT OF SUPERCONDUCTIVITY

Experiments with superconductivity enhancement upon irradiation with electromagnetic waves at radio-frequencies [42] were performed on Sn having $T_c \approx 3.85$ K, corresponding to the BCS energy gap (eq. 1.2) of $2\Delta \approx 1.17$ meV or 280 GHz, which is a limiting photon frequency for sub-gap excitation. In the case of a superconductor with larger gap THz excitation can be used to study similar effects.

In the work [59] energy gap dynamics in a BCS superconductor NbN was studied on a picosecond timescale following sub-gap excitation with intense narrow-band THz pulses. Experiments were performed in a transmission pump-probe geometry, and the changes in the sample

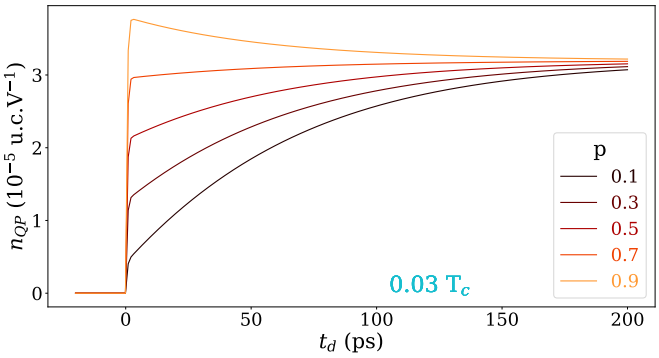

Figure 1.13: Simulation of the delayed pair-breaking dynamics upon photoexcitation in the low perturbation limit, T $\ll$T$_c$. The fraction of energy, initially going to the QP subsystem, p, (in the legend), is varied from "most of the energy is initially in the HFP subsystem" (black curve) to "most of the energy is initially in the QP subsystem" (orange curve). The microscopic parameters, used in the simulation, are: A = 1 mJ/cm^3, Δ = 2 meV, N(E_F) = 0.6narrow-band7 states·eV^{-1}u.c.V^{-1}, R = 100 ps^{-1} u.c.V, β^{-1} = 50 ps.

transmission were associated with changes in the superconducting gap. The transient amplification of superconductivity was argued to be especially pronounced at temperatures near T$_c$.

For pump frequency ν = 1.26 THz < $2\Delta(0)/h$ at the initial stage of pump-probe signal build-up a non-trivial dynamics is observed having an opposite sign to the predicted behaviour by simulation if only the photoinduced suppression of superconductivity is assumed (Fig. 1.14a). This fact was attributed to the Eliashberg-type of enhancement of superconductivity being observed on an ultrafast timescale.

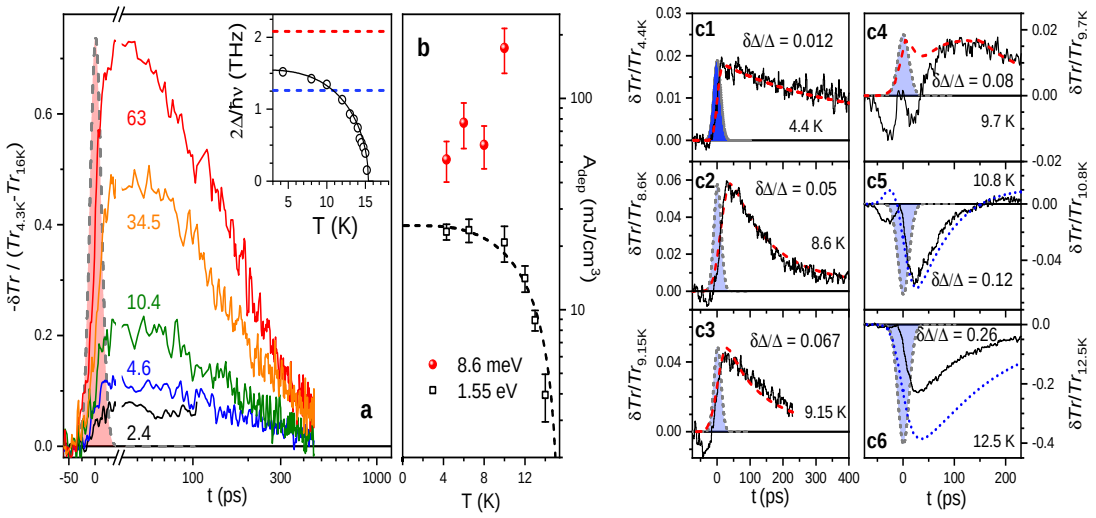

Figure 1.14: Dynamics in NbN films driven by narrow-band THz excitation. **a** Dynamics of the relative change in Tr (normalized to $\mathrm{Tr}_{4.3K} - \mathrm{Tr}_{16K}$) at 4.3 K when pumping with 2.08 THz pulses of different absorbed energy densities A (in mJ/cm^3). Inset shows the T-dependence of gap with the two frequencies used in narrow-band THz pump-probe experiments by the dashed lines. **b** Comparison of the absorbed energy density required to deplete superconductivity, measured with near-infrared pumping at 1.55 eV [47] and THz pumping at 8.3 meV (2.08 THz). The dashed line represents the condensation energy as a function of temperature. **c1** – **c6** Recorded traces of differential transmission for pumping at 1.26 THz at different temperatures (black solid lines). Red dash lines and the blue dotted lines depict the predicted evolution of transmission following the T* model. The blue shaded regions represent cross-correlation of the THz pulses. Around 10 K there is a major difference between the predicted behaviour by the T* model and the experimental data, suggesting that on the 50 ps timescale there is a process, competing with the photoinduced pair-breaking, that governs the dynamics. Adapted from Ref. [5].

In Ref. [60], the dynamics of the optical conductivity in the iron-based superconductor $FeSe_{0.5}Te_{0.5}$, following the NIR optical excitation, was studied by means of pump-probe THz time-domain spectroscopy and by observing the third-harmonic generation in the THz range. The authors discovered that at a very short timescale of a few picoseconds after photo-excitation an increase in σ_2 is observed, speaking in favor of ultrafast enhancement of superconductivity (Fig. 1.15a).

Moreover, the authors studied the third-harmonic generation (THG) in the THz range and its pump-induced dynamics, utilizing NIR pump – THG probe technique. Experimental results, confirmed by simulations, suggest that on the early timescale upon photoexcitation (Fig. 1.15b) an increase in the THG signal can be attributed to a process of an ultrafast transient increase in the superconducting order parameter.

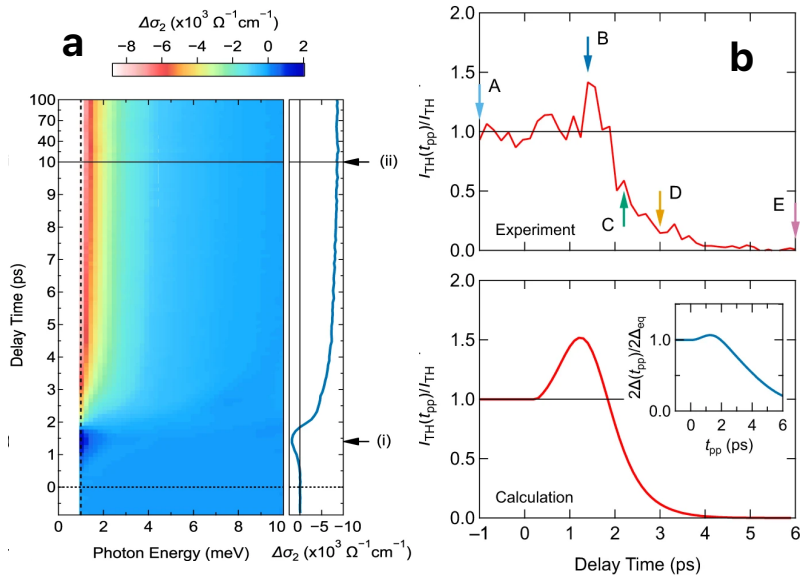

Figure 1.15: **a** Time evolution of the pump-induced conductivity change. **b** Time evolution of the third-harmonic (TH) intensity, normalized by the TH intensity in equilibrium. Top panel represents the experimental data, the bottom panel represents the results of the simulation. An increase in σ_2 shown by arrow (i) and in THG intensity (indicated by arrow B) suggests an enhancement of superconductivity on the picosecond timescale after optical excitation. Adapted from the open-access article [60] under the terms of Creative Commons license.

1.7 SUMMARY

In this Chapter, the theoretical foundations of the superconductivity phenomenon were summarized. We started with the BCS-theory providing the quantum-mechanical description of the "conventional" phonon-mediated superconductivity. The key idea of electrons forming bound pairs via exchange with virtual phonons – Cooper pairs – was discussed first, followed by the BCS model of a coherent state of CPs. Additionally, other theories and models important from the historical or practical aspects or helping to develop understanding of the phenomenon were addressed, such as the GL-theory and the two-fluid model.

Special topics of multi-band superconductivity and out-of-equilibrium phenomena in the superconducting state relevant for the scope of the thesis were also discussed. These, together with the phenomenological Rothwarf-Taylor model, discussed in Section 1.6.3, will be used for analysis and interpretation of the experimental results.

CHAPTER 2

EXPERIMENTAL TECHNIQUES UTILIZED TO STUDY THE SUPERCONDUCTIVITY IN NON-EQUILIBRIUM

> All measuring processes in quantum mechanics may be divided into two classes. In one, which embraces the majority of measurements, we find those which do not, in any state of the system, lead with certainty to a unique result. The other class contains measurements such that for every possible result of measurement there is a state in which the measurement leads with certainty to that result. These latter measurements, which may be called predictable, play an important part in quantum mechanics.
>
> L. Landau, E. Lifshitz: Quantum Mechanics [61]

In this Chapter, we introduce various experimental techniques allowing to shed light on the dynamics of superconductors on the picosecond timescale. We start our discussion with a linear time-domain THz spectroscopy and then complement it with one more dimension provided by time-resolved methods.

2.1 BROADBAND TERAHERTZ TIME-DOMAIN SPECTROSCOPY WITH HIGH SIGNAL-TO-NOISE RATIO

The advent of femtosecond lasers in past decades gave rise to the whole new field - Terahertz time-domain spectroscopy (THzTDS). The main feature of this technique is the phase sensitivity of the method since the electric field is detected. This fact leads to a simpler and hence more robust data analysis directly yielding access to the complex optical conductivity in the THz range without necessity of Kramers-Kronig analysis (and its approximations). The experimental realization of the method consists of the following steps:

- generation of a pulse of electromagnetic radiation narrow in time domain (hence, broad in frequency domain) via nonlinear optical process with the spectrum centered around 1 THz (the *THz pulse*);
- passing through (or reflecting off) the investigated sample, where electric field of the THz pulse acquires changes related to the sample properties
- detection of the transmitted THz pulse utilizing time-domain methods by preserving the phase information.

Different methods to convert the femtosecond optical pulses to phase-stable THz radiation can be utilized: optical rectification in a crystal with the second order of nonlinearity [62], difference-frequency generation yielding high electric fields [63], photoconductive switches [64,65], four-wave mixing in air-plasma based sources [66,67], spintronic emitters [68] etc. The choice of the appropriate THz generation method depends on the task at hand. For example, if high electric fields are required for driving nonlinear effects, such as photoinduced phase transitions, magnonic excitations and more, one can use THz generation in periodically-poled $LiNbO_3$ using mJ-level femtoseond pulses at kHz repetition rate [69]. On the contrary, for the time-domain THz spectroscopy of superconductors, high electric field of the probe pulse is undesirable since the order parameter can be affected by the probe, here, the key parameter to aim at is the high signal-to-noise ratio (S/NR).

2.1.1 OPTICAL LAYOUT OF THE THZ TIME-DOMAIN SPECTROMETER

The experimental layout of the THzTDS used in the experiments described in this thesis is presented in Figure 2.1. As a femtosecond laser source we use amplified laser system (Coherent Rega 9050) being a compromise solution with high repetition rate and pulse energy high

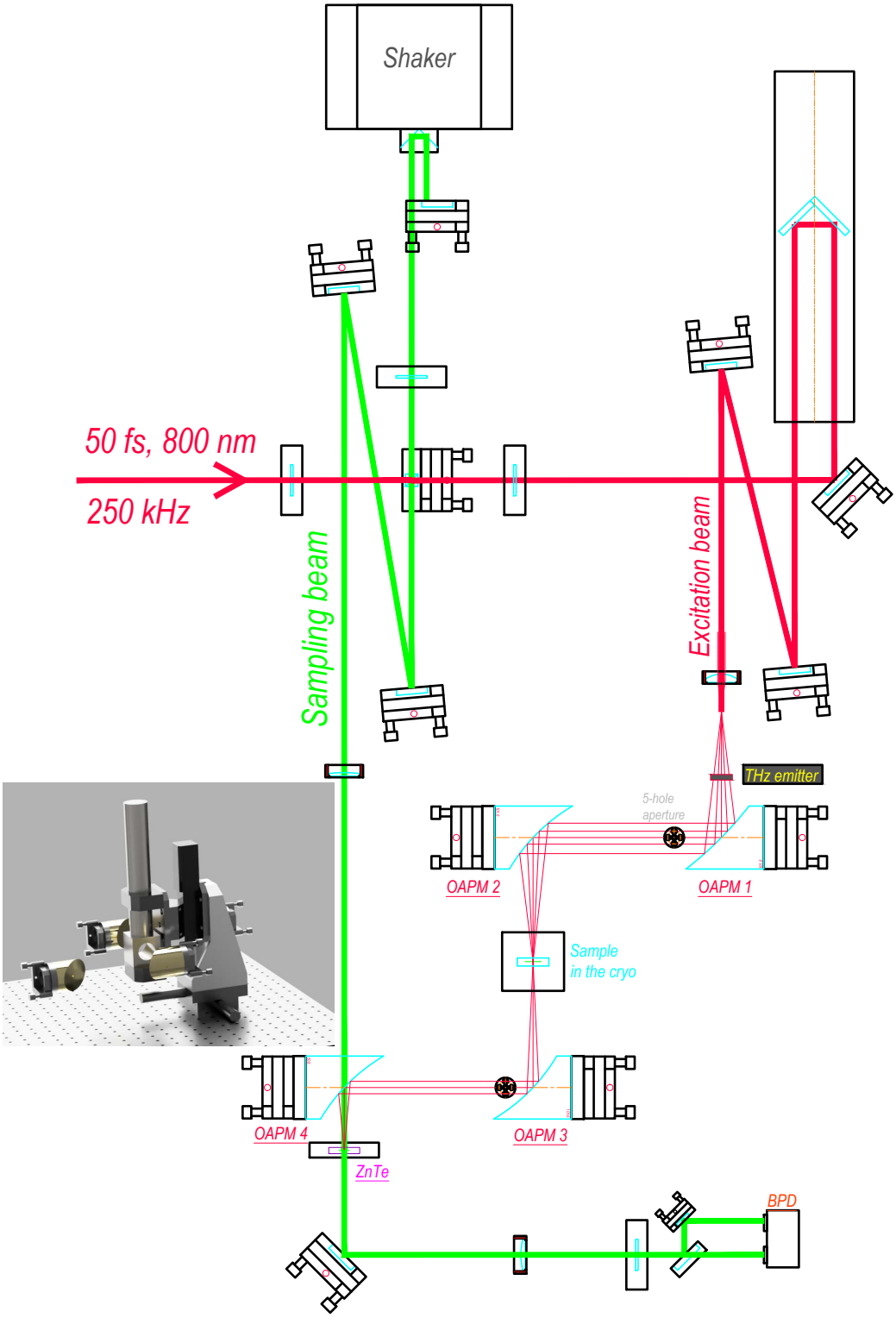

Figure 2.1: Schematic layout of a THz time-domain spectrometer. The incoming laser beam is split into excitation beam that drives the generation of the THz radiation and sampling beam used to the detect the electric field of the THz pulse.

enough to drive nonlinear effects required for efficient THz generation for the purposes of time-domain spectroscopy. Repetition rate of 250 kHz provides lower noise operation compared to 1 kHz systems because one can accumulate a factor of 250 more averages within the same time averaging. Additionally, the spectrum of (mechanical) vibrations contributing to the noise decays towards hundreds of kHz.

The laser beam is split into two: an "excitation" beam and "sampling" beam, with the majority of the laser pulse energy in the "excitation" beam (about 2 μJ). Excitation beam is expanded with a two-lens telescope (not shown) and focused with a short-focus lens. Behind the focal plane of the focusing lens the THz emitter is placed, a nonlinear element converting femtosecond NIR radiation into THz pulses. The distance between the focal point and the emitter is optimized for maximum efficiency of the THz radiation output. We tried different types of THz emitters, the best performance was achieved with the photoconductive antenna (PCA), with a detailed discussion and comparison presented in Section 2.1.2.

Design and alignment of an optical layout for THz radiation is challenging because of several reasons:

a) use of refractive optics is not reasonable because most of the transparent materials have high refractive index in the THz range, this leads to Fresnel losses up to 30% on each surface;

b) broad spectrum of a few THz leads to dispersion broadening of the THz pulse, this is a second argument against using transmission optics;

c) long wavelength of about 100–500 μm forces the use of large aperture optics to avoid diffraction effects;

d) visualizing the THz beam requires expensive cameras, whose sensitivity allows to image only high-power THz beams.

To overcome the mentioned problems a confocal layout was developed and assembled based on 2" aperture off-axis parabolic mirror (OAPM) for guiding and forming the THz beam. The amount of optical elements in the THz beam path was chosen to be minimum necessary because every element contributes to losses and aberrations. The THz radiation propagates through the layout in the following way: a diverging THz beam coming out of the emitter is collimated and guided as a parallel beam with the first OAPM towards the second OAPM. Second OAPM focuses the THz beam, creating the beam waist at the sample position (the sample is typically mounted in the cryostat). After the sample, the diverging THz beam is again collimated and guided with the third OAPM towards the last OAPM. The last OAPM focuses the THz beam into the electro-optic (EO) detection crystal. In the EO crystal THz radiation meets the sampling laser beam which passes through a 3 mm hole in the center of the OAPM and reaches the EO crystal. The focal distance of the first three OAPMs is chosen to be 100 mm from

mechanical design considerations. The last OAPM has focal distance of 50 mm. This allows to achieve 2 times smaller THz beam diameter in the EO crystal in order to increase the sensitivity of the detecting scheme via increasing the electric field of the THz radiation.

Broad spatial frequency range requires precise alignment of the parabolic mirrors, since misalignment-caused aberrations increase the beam size at the focus points, hence, decreasing the electric field strength and overlap quality. Given that the emitted THz radiation follows the excitation beam wavefront, the alignment can be done with the laser beam; alignment technique based on the five-hole diaphragm was developed (see Appendix A for details).

The sampling beam (green line in Figure 2.1) is passing through the fast-scan delay stage – the so called "shaker". Shaker provides the modulation of the time delay between the sampling and excitation pulses within a shaker range of about 2 mm and the frequency of 19 Hz. The double-pass configuration yields in the available time-window of ≈ 25 ps. After the shaker, the sampling beam passes a polarizer to ensure linear polarization state and is focused onto the EO crystal along with the THz beam.

The THz radiation in the EO crystal can be assumed as an electric field (or voltage) applied to the crystal. If the inversion symmetry of the EO crystal is broken, the Pockels effect comes into play, and the THz-induced birefringence in the EO crystal causes the depolarization of the transmitted sampling beam. This depolarization follows the THz electric field waveform. We used 2 mm thick ZnTe as EO crystal, the advantage of this crystal is that the phase velocity of the THz radiation matches the group velocity of the sampling 800 nm pulse allowing to use thick crystals increasing the detection efficiency. However, THz radiation with frequency above 4 THz is absorbed due to the optical phonon resonance of the ZnTe.

After passing the EO crystal, the THz-induced depolarization of the sampling beam is read out in a balance detection scheme: the sampling beam passes the $\lambda/2$ wave-plate oriented at ~ 22.5°and is split by a polarizer into two orthogonally polarized beams which are recorded by two photodiodes of the balanced photodiode (BPD). The orientation of the $\lambda/2$ wave-plate is tuned in a way that the signal at the differential output of the BPD equals zero when there is no THz radiation coming to the EO crystal or when the sampling and THz pulse do not overlap in time. Balanced detection scheme is especially sensitive to small changes in the polarization of the sampling beam providing high dynamic range of the spectrometer. The signal from the BPD is demodulated and projected on the time axis provided by the shaker using the acquisition software.

A typical THz pulse, recorded using this scheme, is presented in Figure 2.2. The reason for an echo-pulse, seen in the transient, is the double reflection of the THz pulse inside the emitter substrate. The time-delay between the main and the echo pulses equals to $\frac{2d_{sub} \cdot n_{THz}}{c}$, where

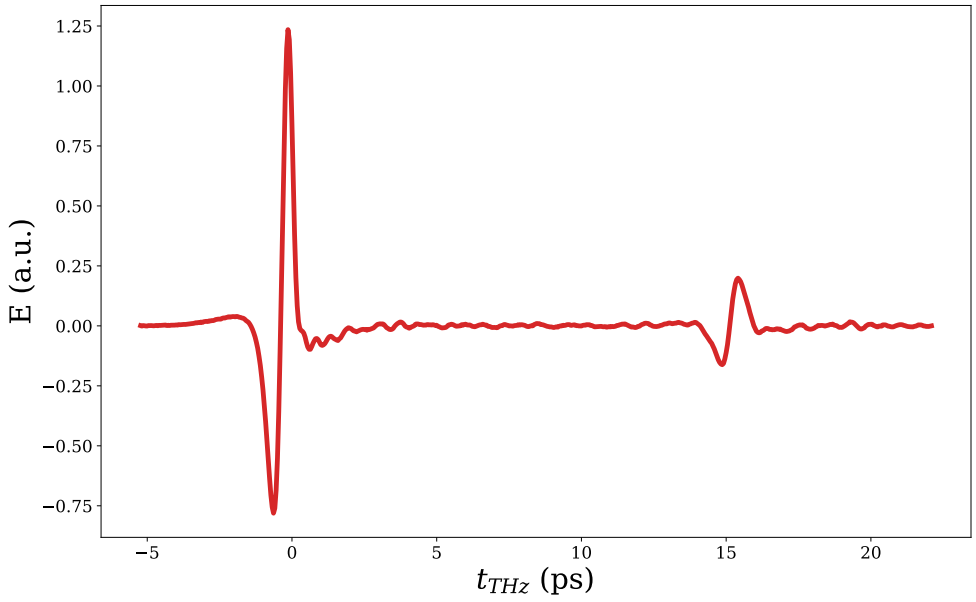

Figure 2.2: Single-cycle broadband THz pulse. A parasitic echo-pulse, delayed by about 15 ps after the main pulse, is a result of a double reflection of the main THz pulse from the front and back surfaces of the THz emitter.

d_{sub} and n_{THz} are the thickness and the refractive index of the substrate in the THz range, and c is the speed of light. In general, the echo pulse is a parasitic phenomenon, either limiting the width of the time-window or leading to the complicated analysis of the data.

2.1.2 THE THZ GENERATION

Nowadays, table-top nonlinear conversion of the ultrashort laser pulsed radiation into the THz radiation is an established technique, and different physical principles are used to provide characteristics required in the every specific case. Some of these methods, such as four-wave mixing in air plasma [70, 71], or difference frequency generation [72, 73], require laser pulses with energy in the mJ range and are not discussed here, since the output pulse energy of our laser system is $\approx 6\ \mu J$.

The THz generation with interdigitated PCA as an emitter is an established technique in our lab, a lot of effort was put in the performance optimization [64, 74]. THz radiation is generated via acceleration of photoinduced carriers in the semiconductor upon applied bias electric field. For this purpose, a comb-like microstructure of interdigitated finger electrodes is formed on the LT-GaAs substrate having the size of 10×10 mm^2. The spacing between the electrodes as small

as 5 μm allows to achieve high electric field strength with the bias applied voltage of ~ 15 V. As shown in [64] the dependence of the output THz electric field on the incident laser excitation energy density saturates earlier when the laser beam is smaller, hence, large illuminated area of the PCA THz emitter allows to achieve higher conversion efficiency.

As it was shown earlier [64, 75], the emitted THz radiation follows the wavefront of the excitation laser beam. Given that the wavelength of the THz radiation is ≈ 300 times larger than that of the NIR, the diffraction effects cannot be neglected even for the "macroscopic" THz beams with the diameter of ≈ 10 mm (the size of the PCA emitter). Therefore, excitation of the THz emitter with the collimated laser beam having a diameter of ≈ 10 mm is suboptimal, because compensation of the diffraction-caused divergence will complicate the layout with additional optical elements, thus making it bulky and less efficient.

Instead, we place the PCA THz emitter in the excitation laser beam focused with a 35 mm lens at the distance of 50 mm after the focal plane of the focusing lens. Here the beam diverges to ≈ 10 mm to efficiently use the entire area of the PCA. The back focal plane of the first OAPM matches the focal plane of the 35 mm lens, providing collimation of the emitted THz radiation with the first OAPM (described in Section 2.1).

Another novel approach in THz generation is based on using of a spintronic emitter (STE), which utilizes the ultrafast inverse spin-Hall effect in the ferromagnetic/heavy-metal multilayer film on a substrate [76]. The main idea is the following: the femtosecond laser pulse hits the ferromagnetic material placed in an external magnetic field. The photoinduced current is spin-polarized and enters the HM material with high spin-orbit coupling. The photocurrent is split into spin-up and spin-down electrons due to the relativistic spin-orbit coupling propagating with the angle called spin-Hall angle, thus generating a transverse charge current. The transverse charge current, having a picosecond timescale, leads to antenna-like generation of the radiation lying in the THz range. The reported bandwidth of such a radiation is gapless and covers from 1 to 30 THz range. The STE is a bi-(or tri-)layer thin film which is easier and cheaper to fabricate compared to, for example, growing the ZnTe crystal, or processing the microstructure on a semiconductor. An interesting feature of the STE is that external magnetic field defines the polarization of the emitted THz radiation.

We tried the STE similar to reported in [68], a trilayer sandwich of W/CoFeB/Pt on a sapphire substrate. The STE was mounted in a special device with permanent magnets creating external magnetic field with the possibility of rotating the magnets with respect to the STE to control the polarization of the output THz radiation. We observed that with rotating the magnetic field by 180°the THz pulse changes sign. However, the amplitude of the THz signal is substantially smaller compared to the PCA emitter (Fig. 2.3b), even though the bandwidth is broader. Per-

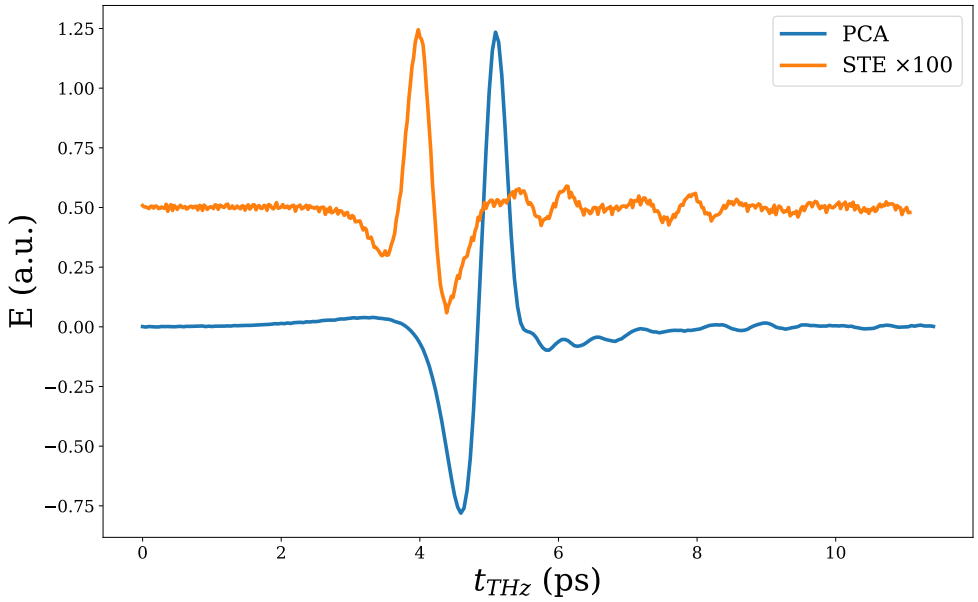

Figure 2.3: THz pulses, generated by STE and PCA, separated vertically for clarity. The amplitude of the THz pulse, generated by the STE, is substantially lower, compared to the PCA, and is multiplied by 100. From the S/NR considerations, using of the PCA is beneficial.

haps the degradation of the STE thin film took place, or the parameters of the excitation laser pulses were suboptimal for the STE performance. Thus, the PCA emitter was our work horse in carrying out THz spectroscopy experiments.

One more aspect speaks in favor of the PCA emitter. A well-established technique for reducing the noise based on the modulation of the signal, i.e., the so called "dark control" can be implemented by modulating the voltage applied to the PCA. The principle of the *dark control* operation is the following: the voltage applied to the PCA is a sequence of pulses synchronized with the laser repetition rate, with the duty cycle of about 10% to reduce the heating of the PCA. Odd pulses have opposite polarity with respect to even pulses, and so do the THz pulses. The noise of the detection scheme is supposed to be independent on the voltage polarity applied to the PCA, so the data acquisition software subtracts even pulses from the odd ones resulting in cancelling of stochastic noise and additional increasing of the S/NR by a factor of 2 due to the polarity switching.

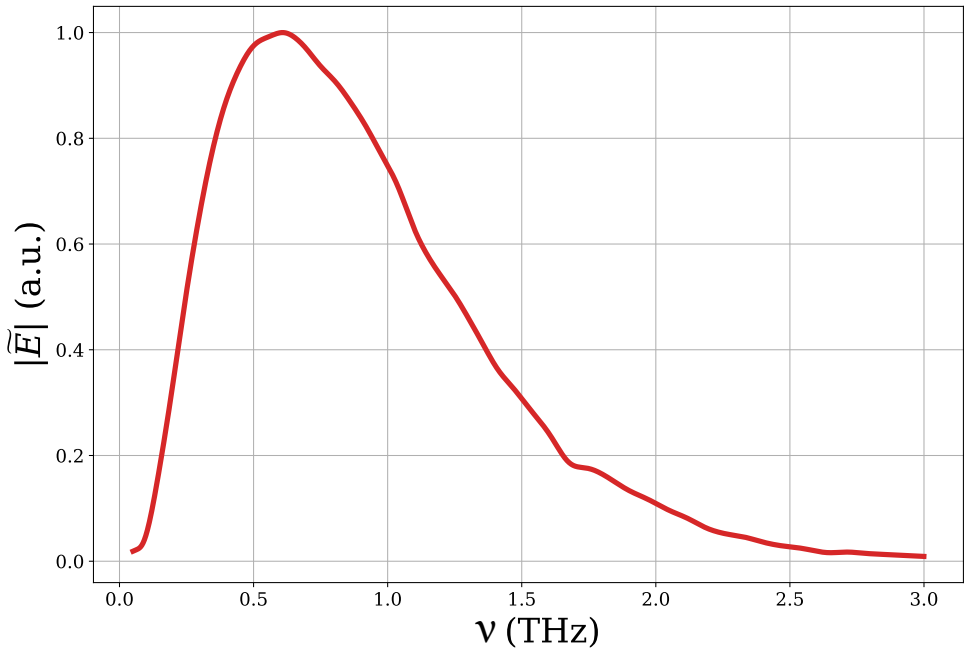

Figure 2.4: The absolute of the spectrum $|\widetilde{E}(\nu)|$ of the THz pulse represented in Fig. 2.2.

2.1.3 Extracting the complex optical conductivity

Typically, to investigate the complex optical conductivity of the material by means of THzTDS a thin film is deposited on a substrate transparent in the THz range and the transmission of the THz radiation is recorded through this sample and through the bare substrate (reference). Applying the Fourier transformation to the time-domain signal (Figure 2.2) provides with the complex spectrum of the transmitted radiation (the absolute of the spectrum is shown in Figure 2.4). By dividing the complex spectra of sample and reference the complex transmission is obtained

$$\widetilde{T}r(\omega) = \frac{\widetilde{E}_{sample}(\omega)}{\widetilde{E}_{reference}(\omega)}. \tag{2.1}$$

The complex transmission contains all the information about the optical properties of the material. In the case of a metal it is common to use complex optical conductivity $\widetilde{\sigma} = \sigma_1 - i\sigma_2$ (not the complex dielectric function $\widetilde{\epsilon}$). In general, one has to numerically solve the following equation 2.4 to fit $\widetilde{T}r_{model}(\omega)$ to the experimental $\widetilde{T}r_{exp}(\omega)$, extract complex refractive index $\widetilde{n}_s(\omega) = n(\omega) + i \cdot k(\omega)$ and recalculate to optical conductivity $\sigma_1(\omega)$ and $\sigma_2(\omega)$ (which is more

common in the case of a metal) using textbook formulas [18, 74, 77]:

$$\widetilde{T}r_{model} = 2\widetilde{n}_s(n_1+n_3)(\widetilde{n}_s+n_1)^{-1}(\widetilde{n}_s+n_3)^{-1}\times \tag{2.2}$$

$$\times\, e^{i\omega d(\widetilde{n}_s-n_1)/c}\cdot e^{i\omega(n_3-n_1)\Delta L/c}\times \tag{2.3}$$

$$\times\left[1-\frac{\widetilde{n}_s-n_1}{\widetilde{n}_s+n_1}\cdot\frac{\widetilde{n}_s-n_3}{\widetilde{n}_s+n_3}\cdot e^{2i\omega d\widetilde{n}_s/c}\right]^{-1} \tag{2.4}$$

where n_1 is a refractive index of the air/vacuum, n_3 is a refractive index of the substrate, d is a thickness of the film, ΔL is a substrate thickness difference between the sample and the reference, c is the speed of light in vacuum.

The situation may be simplified if the sample is a metallic thin film with high conductivity deposited on a transparent dielectric substrate and placed in vacuum. In this case the problem of finding optical conductivity has an analytical solution:

$$\widetilde{\sigma} = \frac{(1+n_3)}{Z_0 d}\cdot\left[\frac{e^{i\omega(n_3-1)\Delta L/c}}{\widetilde{T}r_{exp}(\omega)}-1\right] \tag{2.5}$$

where $Z_0 \approx 377\ \Omega$ is the vacuum impedance. This equation is called a *thin-film formula (TFF)*, the criteria of its validity are the following: $\omega\widetilde{n}_s d/c << 1$ and $\widetilde{n}_s >> n_3 > 1$. These conditions are fulfilled for the experiments described in this thesis, so the TFF 2.5 may be applied for calculating the optical conductivity.

Fig. 2.5 shows real and imaginary part of optical conductivity of MgB_2 in the normal state (above T_c) measured prior to the time-resolved THz spectroscopy. By fitting the conductivity with Drude model, we find the scattering rate $\tau^{-1} = 1.4$ THz, similar to the value reported in [78].

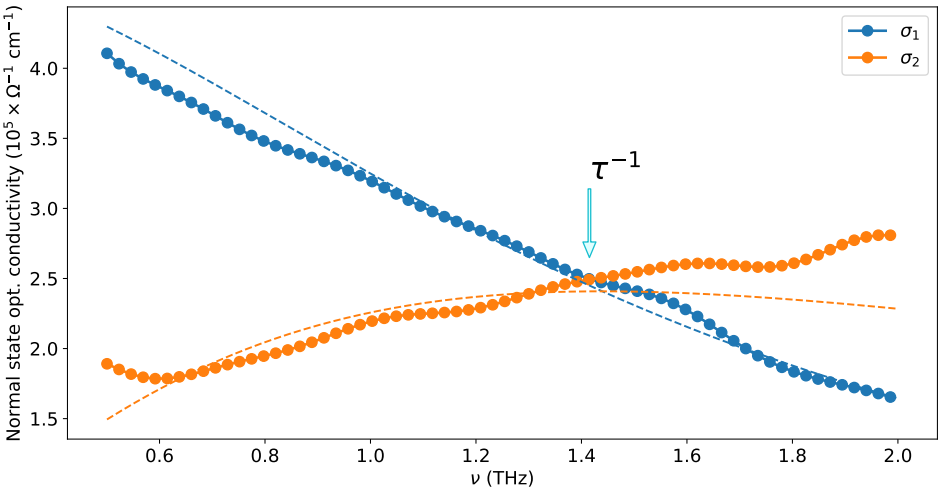

Figure 2.5: Real and imaginary part of the optical conductivity of MgB_2 obtained in THzTDS for T = 36 K > T_c. The dashed lines represent the fit with the Drude model. An arrow points at the scattering rate τ^{-1} = 1.4 THz.

2.2 TIME-RESOLVED EXPERIMENTS IN THE THZ RANGE

With such a powerful probing tool in the THz range it is natural to expand the THzTDS complementing it with the temporal dimension. Namely, quasi-instantaneous excitation (*pump*) synchronized with the *probe* may be utilized, and the medium properties driven by an ultrafast excitation are studied as a function of the time-delay between *pump* and *probe*.

Nowadays, the diversity of Pump-Probe (PP) techniques is astonishing, covering most of the electromagnetic spectrum, from optical pump-probe microscopy [79] to time-resolved angle-resolved photoemission [80]. Here, we will focus our attention on the utilizing pump-probe methods in the THz range.

2.2.1 OPTICAL PUMP – BROADBAND THZ PROBE SPECTROSCOPY

We start the discussion of the PP techniques in the THz range with a simple – in terms of staying within the table-top framework - optical pump – THz probe (OPTP) spectroscopy, where the THz response of the investigated system is studied upon photoexcitation with femtosecond NIR laser pulses. In terms of an optical layout the complexity of the experiment is marginally increased compared to the "linear" THzTDS – part of the parental laser beam (we will call it "pump") is guided through the delay stage and the forming optics directly to the sample (as shown in the layout in Fig. 2.6). The delay stage controls the time delay t_d between the pump

laser pulse and the THz broadband pulse (*probe*). The pump radiation is mechanically modulated by the chopper and the lock-in detection is utilized.

The data acquisition and the data analysis in the optical pump – broadband THz probe experiment is more complicated due to the additional degree of freedom. There are at least four parameters to be tuned: frequency (as a Fourier transform of the time axis), temperature of the sample, time delay between the pump and the probe, and the pump energy density. Given that the time required for performing a comprehensive set of measurements and further analysis of the obtained data exponentially scales with the number of parameters, the following methods of the data acquisition in the OPTP experiment may be utilized in order to optimize the duration of the experiment:

a) Fixing the time delay of the probing THz electric field to some characteristic point in $E(t)$. The spectrally-integrated response can be measured (as a voltage on the BPD) and changes in the electric field of the probe, transmitted through the sample, $\Delta E_{\text{probe}}(t_d)$ are recorded as a function of pump-probe time delay, t_d. The choice of the characteristic point on the time-axis of the THz pulse might depend on the experimental condition and investigated sample. To study the dynamics of superconductivity we used the point where the THz E-field crosses the time-axis between maximum and minimum. (becoming equal to zero) since the superconducting response is mainly manifested as an inductive change of the phase of the probe signal;

b) The entire THz electric field $\widetilde{E}(t_{THz})$ is recorded at certain values of t_d with coarse time steps (compared to case **a**), providing access to frequency-dependent optical properties (complex conductivity, refractive index, or permittivity) of the medium at every set of parameters. The data acquisition can be performed utilizing the double lock-in detection, where the pump signal is mechanically modulated with the chopper, an the THz probe is modulated by modulating the bias voltage on the PCA emitter at the frequency, equal to half of the repetition rate of the femtosecond laser system ($\approx$ 125 kHz). We call these type of data acquisition *spectrally-resolved scans*.

2.2.2 NARROW-BAND THZ PUMP – BROADBAND THZ PROBE SPECTROSCOPY

In Section 2.2.1 describing optical pump–THz probe experiment the photon energy range of pump and the probe differs by more than two orders of magnitude, $h\nu_{pump} = 1.5\ eV$ while $h\nu_{probe} \approx 4\ meV$. The optical excitation on the timescale of the temporal resolution of the experiment can be often considered as quasi-thermal, given the fast electron-electron and electron-phonon scattering processes one can approximate that photoexcitation results in heating of electronic subsystem.

For many applications, perturbing the system resonantly provides additional insights on

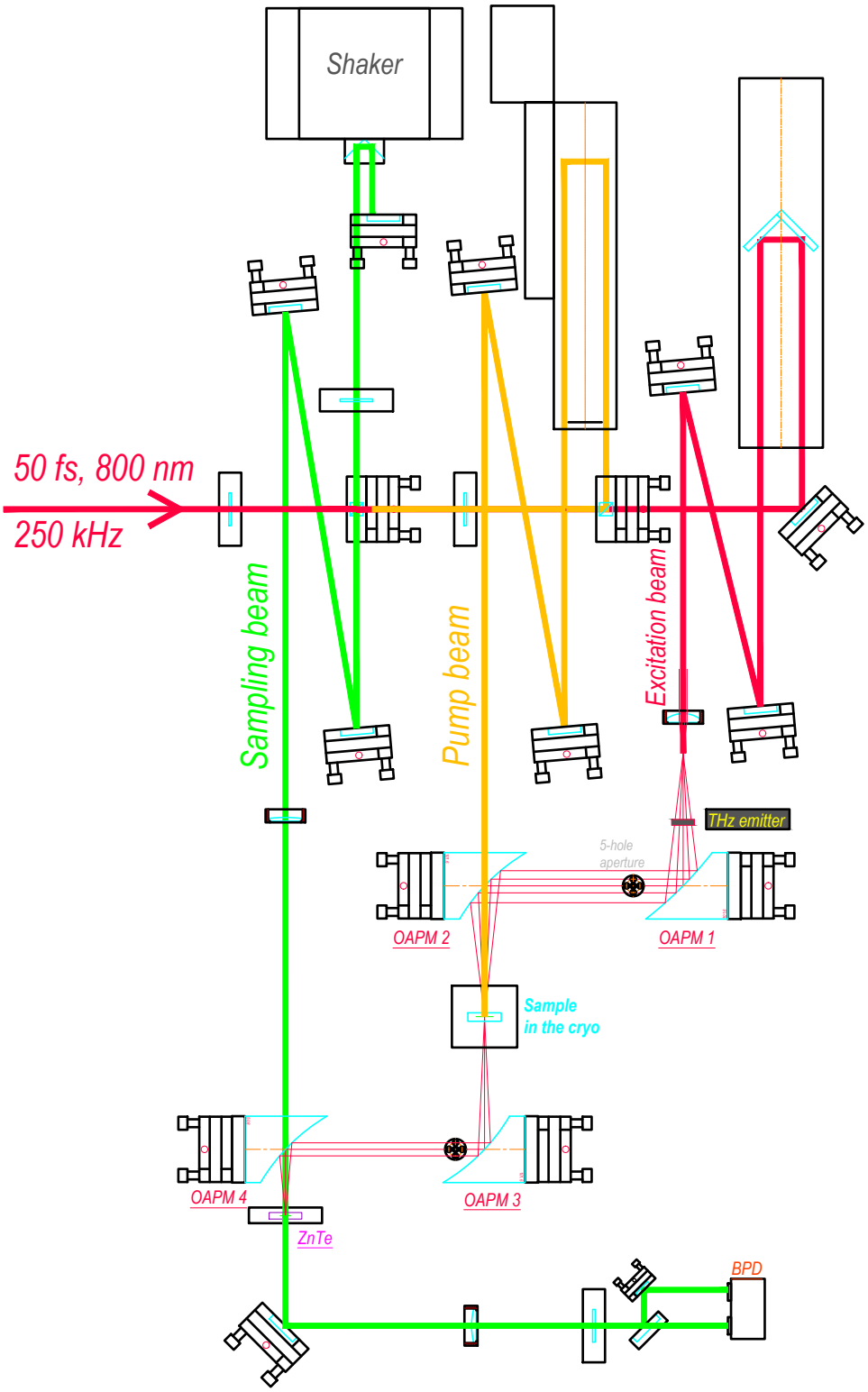

Figure 2.6: Optical layout of the Optical pump – THz probe spectroscopy setup. Part of the incoming laser beam is reflected to the pump beam path. The pump beam passes the delay stage that controls the pump-probe time delay t_d.

the internal process on the ultrafast timescale. This is especially true for the case of the non-equilibrium spectroscopy of superconductors in the THz range. For example, the system may behave differently if the photon energy excitation is below or above the superconducting gap 2Δ [42, 59]. Here, for $\hbar\omega_{pump} < 2\Delta$ the direct Cooper pair breaking is not possible while for $\hbar\omega_{pump} > 2\Delta$ the pump photon is absorbed with creation of two QPs.

However, driving the non-equilibrium processes with THz pulses is challenging because the powerful source of THz radiation is required. Additionally, for resonant excitation the radiation should be narrow-band. Nowadays, table-top sources driven by mJ-level pulses at several kHz repetition rate can reach relatively high electric field values of the THz broadband pulses, however, achieving narrow bandwidth (by means of frequency filtering) reduces the energy of the THz pulses.

Another approach is to use the FEL-based sources at large-scale facilities. Our narrow-band *THz-pump* experiments were performed at the FELBE facility (HZDR), where the free-electron laser (FEL) provides pulsed THz radiation (THz_{FEL}) with central frequency tunable from 1.3 THz to ~10 THz with the output power up to 30 W (depending on the settings) at a 13 MHz repetition rate. The radiation is narrow-band with the bandwidth of ~ 2%, which is perfect for resonant pumping experiments.

The part of the THz pump-probe setup is represented in Fig. 2.7 [81]. The probing broad-band pulses (THz_{probe}) must be synchronized with THz_{FEL} pulses (in the OPTP experiment this is satisfied automatically) and delivered to the THzTDS layout. Alignment of the layout is non-trivial, because of the above mentioned difficulty of visualization of the THz beam. Moreover, to avoid perturbation of the studied system by the probe pulse itself, the broadband THz probe pulse at 250 kHz repetition rate has low intensity, which makes its imaging impossible. As a result, this may lead to some uncertainty in the spatial overlap between the pump and the probe and hence, reduces the precision in calculating the pump absorbed energy density (AED).

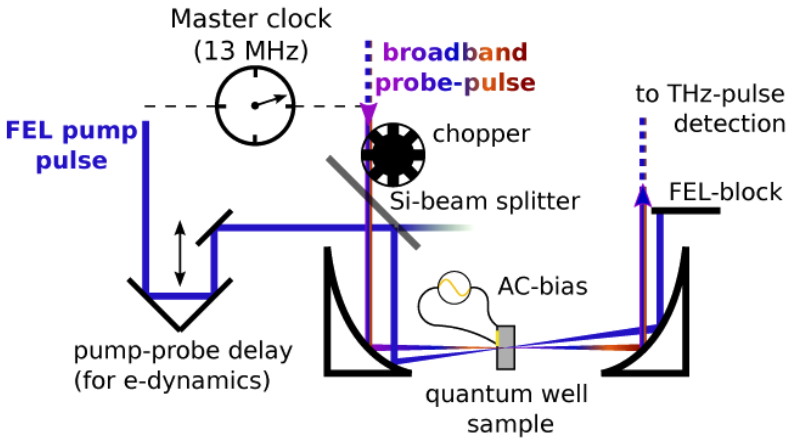

Figure 2.7: Schematic layout of the narrow-band THz pump – broadband THz probe experimental setup. The Si wafer acts as a coupler, the probe beam is transmitted through, and the pump is reflected off the wafer. Reproduced from the Ref. [81] under OSA Open Access License agreement.

With above mentioned difficulties, after establishing the synchronization between FEL and the femtosecond laser system and finding temporal and spatial overlap the measurement procedure the THz pump – THz probe (TPTP) experiment is similar to the OPTP. Again, for the sake of optimizing acquisition time (limited by the allocated *beam-time*) of the experiment, the data acquisition is split into *spectrally-resolved* scans and *1D-scans*, with further data analysis following the approach of the OPTP spectroscopy (Section 2.2.1). Such a similarity in performing the experiment and data analysis provides robust basics for comparing the dynamics in the case of excitation with either NIR or THz pulses.

2.2.3 NARROW-BAND THZ PUMP – NARROW-BAND THZ PROBE EXPERIMENTAL TECHNIQUE

In Chapter 2, we started the discussion of the time-resolved techniques in the THz range with the Optical Pump – Broadband THz probe spectroscopy configuration, where the pump and the probe differ in photon energy by a factor of ~400, temporal and spectral characteristics, etc. Afterwards, we discussed the Narrow-band THz Pump – Broadband THz Probe spectroscopy experimental technique, where the *pump* and the *probe* are both the THz pulses, possessing different temporal and spectral properties. Keeping this line of thought, in this Section we will discuss narrow-band THz pump – narrow-band THz probe (NbTHzPP) technique, where the pump and the probe pulses are the result of splitting the narrow-band FEL pulse with the dif-

ference only in polarization and intensity.

Time-resolved THz pump-THz probe studies were performed at the free electron laser facility (FELBE) at the HZDR, providing intense narrow-band (spectral width of ≈ 25 GHz, pulse width (intensity) $\tau_{\mathrm{FEL}} \approx 16$ ps) THz pulses at a repetition rate of 13 MHz. The layout of NbTHzPP experiment is presented in Fig. 2.8. Experiments were performed in a standard single color pump-probe configuration.

The setup is coupled to the FEL via free-space waveguides. After entering the setup, the small part of the THz_{FEL} beam is reflected by the first beamsplitter to the power monitor. This detector constantly measures the power of the incoming THz radiation during the experiment to account for power fluctuations in the further data analysis. The second beamsplitter splits the beam into the pump and the probe arms with the ratio of ≈ 90 : 10.

The probe pulse passes through the delay stage (which is computer controlled), providing the temporal resolution of the experiment, and comes at the center of the 90° OAPM1. At the focal plane of the OAPM1 the cryostat (with the mounted sample) is placed and the probe beam, reflected and focused by the OAPM1, is incident at the sample surface. The sample is mounted in a liquid helium cryostat with 1" CVD diamond windows. The temperature is controlled by a Lakeshore temperature controller. After passing the sample the probe beam is collimated with a OAPM2 and focused with a OAPM3 onto the detector. The detector is a bolometer cooled with the liquid helium (Infrared Laboratories LN6/C).

One of the disadvantages of the simple NbTHzPP technique is that besides the probe signal the detector is also sensitive to parasitic (for the detector) pump radiation which reduces S/NR. The iris diaphragm and the polarizer after the OAPM2 are meant for filtering out the residual pump radiation.

The pump beam (after the beamsplitter) passes through the mirror-based 90°polarization rotator, providing orthogonal polarization with respect to the probe beam, and a five-position variable wire-grid attenuator (LASNIX), allowing for changing the pump intensity. Then, the pump beam hits the OAPM1 off-center in order to:

a) obtain oblique angle of incidence at the sample to be efficiently blocked by the iris diaphragm;

b) increase the pump beam size at the sample position (due to off-axis aberrations) to enhance uniformity of excitation.

Both pump and monitor beams were mechanically chopped at 233 Hz to provide detection using the lock-in amplifier (Stanford Research Systems SR830).

Preliminary alignment of the layout is done with the alignment laser beam, the precise overlapping of pump and probe beams is achieved by a pyroelectric camera, sensitive in the THz

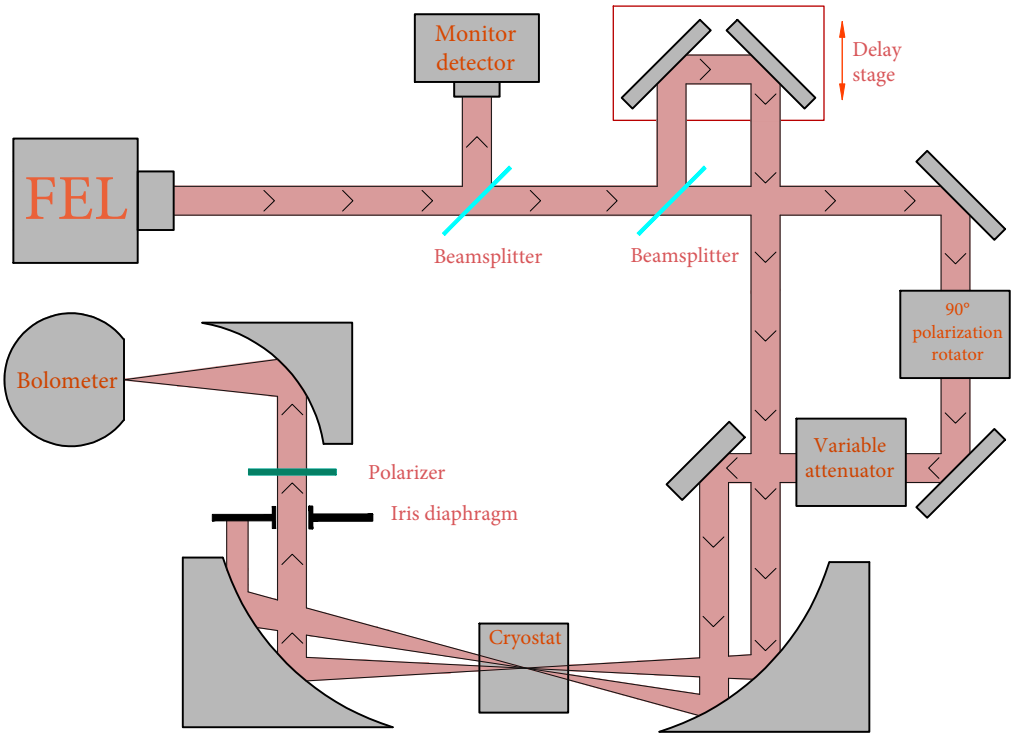

Figure 2.8: Optical layout of the narrow-band THz pump–probe setup. The pump beam is incident on the sample (in the cryostat) at an oblique angle with respect to the optical axis, and the residual pump is filtered by the iris diaphragm and the polarizer.

range. At the same time the beam size is evaluated from the images, obtained by the camera. Fine alignment is done by optimizing the magnitude of the pump-probe signal, and the best filtering of the residual pump beam (affecting the detection) is achieved by monitoring and reducing the noise of the signal.

CHARACTERIZATION OF FEL THZ PULSES

Changing the FEL frequency of the THz radiation affects the parameters of THz pulses that are important for determining the absorbed energy density and the time resolution (given by the cross-correlation of the THz pulses). Namely, with increasing the frequency the spectral width is increasing and the pump beam diameter at the focus is decreasing (Table 2.2.3). Spectral width was determined with the FTIR spectrometer after tuning the FEL to desired frequency, and the pulse widths were calculated from the spectral width and frequency, assuming transform-limited pulses [82]. Pump beam diameters at the sample position (at the focus of OAPM1) were measured directly in the experiment with the Pyrocam. Fig. 2.9 shows an example of the pump

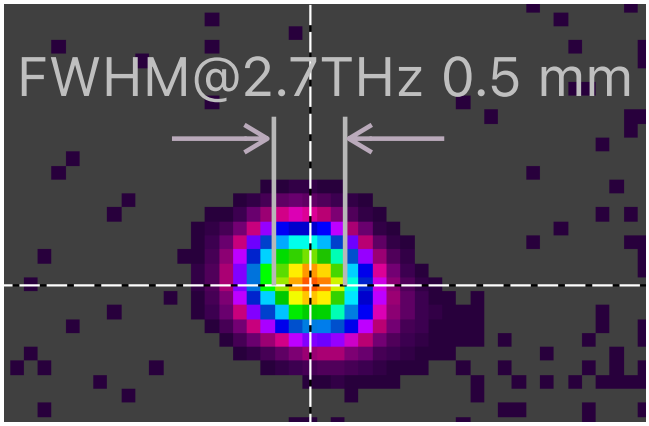

Figure 2.9: The pump beam profile at ν_{FEL} = 2.7 THz, with the FWHM beam diameter at the focus of 0.5 mm measured by the Pyrocam. An uncertainty in the pump beam diameter, caused by the low available resolution of the camera, leads to an uncertainty in calculating the absorbed energy density.

beam profile at ν_{FEL} = 2.7 THz.

$\nu\ (THz)$	$\Delta\nu\ (GHz)$	$\tau_{FEL}\ (ps)$	$\varnothing\ (mm)$
1.49	24.0	18.4	1.05
2.09	27.2	16.2	0.75
2.73	29.4	15	0.5

Table 2.1: Parameters of the THz pulses: carrier frequency, spectral width, pulse width, beam diameter at focus (FWHM).

2.3 SUMMARY

In this chapter, we describe experimental techniques in the field of THz spectroscopy used in this work to study the superconducting state and its dynamics. We start with the linear THzTDS that enables access to the main characteristic of the material in the THz range, for example, directly observe the opening of the superconducting gap below the phase transition. By expanding this method with ultrafast perturbation we can shed light on the behavior of the material

in non-equilibrium. Different types of excitation and detection are discussed - pumping with femtosecond NIR laser pulses and narrow-band THz pulses, and probing with either broadband (OPTP and TPTP) or narrow-band (NbTHzPP) THz pulses.

Each of these methods and their combination was utilized for investigation of the behavior of a superconductor in the non-equilibrium regime. Comparison of resonant and off-resonant excitation provides an access to the microscopic properties and phenomena in superconductors exposed to pulsed excitation. The technique is important for development of the theory and our understanding of strongly correlated systems.

CHAPTER 3

TIME-RESOLVED STUDIES OF THE ENERGY GAP DYNAMICS IN MgB_2

> The measuring process has in quantum mechanics a very important property: it always affects the electron subjected to it, and it is in principle impossible to make its effect arbitrarily small, for a given accuracy of measurement. The more exact the measurement, the stronger the effect exerted by it, and only in measurements of very low accuracy can the effect on the measured object be small. This property of measurements is logically related to the fact that the dynamical characteristics of the electron appear only as a result of the measurement itself. It is clear that, if the effect of the measuring process on the object of it could be made arbitrarily small, this would mean that the measured quantity has in itself a definite value independent of the measurement.
>
> L. Landau, E. Lifshitz: Quantum Mechanics [61]

In the Chapter 2 we presented the arsenal of the experimental techniques to study the superconductivity in the out-of-equilibrium. In this Chapter, we present systematic studies of the

photoinduced dynamics in a two-band superconductor MgB_2 using THz pump – THz probe and optical pump – THz probe techniques. We have studied the temperature and absorbed energy density dependencies of the gap dynamics of the MgB_2 thin film on a picosecond timescale following excitation with intense narrow-band THz and femtosecond NIR pulses. As opposed to excitation with NIR pulses at 1.55 eV, THz pumping enables direct excitation of low-energy QP and gives rise to their non-thermal distribution.

The two-band superconductor MgB_2 is an outstanding material, we discussed its remarkable properties in Section 1.5. The presence of the two gaps and the coupling between them, on the one hand, gives rise to intriguing phenomena like the Leggett mode, a collective excitation caused by fluctuations of the relative phase of the two order parameters, while on the other hand, makes understanding of the ground state electrodynamics complicated.

Section 3.1 presents the results of experimental studies of the energy gap dynamics in MgB_2 utilizing resonant THz pump–probe technique. As our main result, we demonstrate that the non-monotonous temperature dependence of the photoinduced gap suppression suggests the existence of the process, competing with photoinduced quenching of the superconducting order.

In Section 3.2 we show the direct comparison between the gap dynamics for the cases of resonant THz excitation and off-resonant optical excitation, confirming that the observed minimum in the suppression of the superconducting order at $0.6 \cdot T_c$ is limited to the case of narrow-band THz excitation.

3.1 Energy gap dynamics of MgB_2 driven by resonant THz pulses

High-quality single-crystalline MgB_2 thin film, having a film thickness of 30 nm, with the c-axis epitaxy, was grown on MgO (111) 5×5 mm^2 substrate, using a hybrid physical-chemical vapor deposition method [83], and characterized by X-ray diffraction and charge transport measurements [78].

Time-resolved studies of the dynamics following THz pumping were performed at the HZDR at the FEL facility, which provided intense narrow-band THz pulses ($\Delta\nu_{FEL} \approx 25$ GHz, $\tau_{FEL} = 14-18$ ps) at a repetition rate of 13 MHz. Experiments were carried out in a single-color pump-probe configuration using three different frequencies ν_{FEL} of the THz beam: 1.5 THz, 2.1 THz and 2.7 THz. All used frequencies are above the lower gap value $2\Delta_\pi$, with 2.7 THz exceeding $4\Delta_\pi$. For reference, we performed complementary studies of the dynamics driven by femtosecond near-infrared pulses.

Upon absorbing pump pulse radiation with photon energy higher than the energy of the gap 2Δ, direct breaking of CPs occurs, leading to the reduction of the superconducting condensate density and increasing of the quasi-particles (QP) density. Experimental studies, performed earlier on MgB_2 in OPTP configuration [37] and in the single-color THz pump-probe experiment on NbN [59], showed that the maximum gap suppression is achieved on the tens-of-picoseconds timescale; these observations are consistent with our results.

We base our analysis of the experimental data on the T^* model, suggested by Parker [51] (see Section 1.6.3). The model considers optical excitation, where the QPs and the condensate share the same chemical potential, yet the QP temperature T^*, which is equals to the temperature of high frequency ($\hbar\omega > 2\Delta$) bosonic excitations, i.e., phonons, is higher than the temperature of low energy ($\hbar\omega < 2\Delta$) phonons (base temperature). This assumption is supported by the long timescales of the dynamic processes, suggesting that at each time delay the condensate(s) are in a quasi-equilibrium with QPs and high frequency phonons (HFP) [47], and by the fact that the absorbed energy density required to suppress the SC roughly matched the total condensation energy of MgB_2. The latter observation, as discussed in detail below, also implies that on the timescale beyond the $\approx$ 15 ps resolution-limit the two gaps Δ_π, Δ_σ exhibit the same dynamics, likely with the constant $\frac{\Delta_\sigma}{\Delta_\pi}$ ratio.

3.1.1 EXTRACTING THE DYNAMICS OF THE EFFECTIVE GAP FROM THE MEASURED PUMP-INDUCED CHANGES IN TRANSMISSION

Prior to the pump-probe experiment, we measured the temperature dependence of the transmission of the probe pulses through the MgB_2 thin film at each photon energy (Fig. 3.1a). As we can see, the temperature dependence of the differential normalized transmission, $\delta Tr(T) \equiv (Tr_{SC}(T) - Tr(T_c))/Tr(T_c)$, resembles that of the BCS superconducting gap (yet being different for different photon energies), reaching zero at $T = T_c$ in the fashion of the second-order phase transition. Thus, we approximated this dependence with the following formula:

$$\delta Tr(T) = A\left[tanh\left(C\sqrt{\frac{T_c}{T}-1}\right)\right]^p \tag{3.1}$$

Here, the coefficients A, C and p are the fit parameters, and T_c is the critical temperature, equal to 36 K for the thin-film MgB_2 sample.

Fig. 3.1b shows the temperature dependence of Δ_π. Circles are the values, obtained by fitting the equilibrium optical conductivity with Mattis-Bardeen formulas assuming a single gap [78], and the dash line is the fit with the BCS temperature dependence. It should be noted, that $\Delta_{\text{eff}}(T = 0)$ is some effective value of the gap (considering the two-gap nature of MgB_2). As it

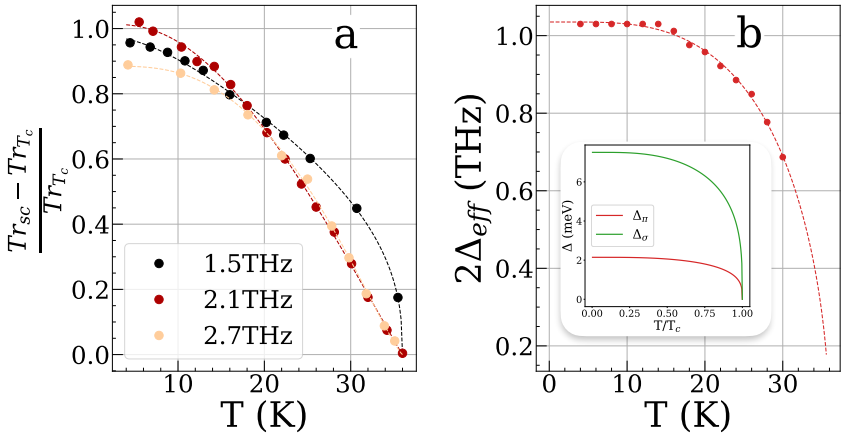

Figure 3.1: **a** Differential transmission of the probe pulse as a function of T. Solid circles represent data points and the dashed lines represent the fit with the eq. 3.1. **b** Temperature dependence of the superconducting gap extracted from fitting the optical conductivity obtained by THzTDS [78]. Solid circles represent data points and the dashed lines represent the fit with the BCS temperature dependence. The value $2\Delta_{\text{eff}(0)}$ matches that of $2\Delta_\pi$. The inset (Fig. 1.8) show the temperature dependence of Δ_π (red) and Δ_σ (green).

was shown in Section 1.5, the temperature dependencies of Δ_π and Δ_σ differ only by a scaling factor, i.e., $\frac{\Delta_\pi(T)}{\Delta_\pi(0)} = \frac{\Delta_\sigma(T)}{\Delta_\sigma(0)} = \frac{\Delta_{\text{eff}}(T)}{\Delta_{\text{eff}}(0)}$, so the $\Delta_{\text{eff}}(T)$ describes the temperature dependence of the coupled order parameter. Thus, here and further, when discussing the gap dynamics, the gap Δ is implied as the effective gap Δ_{eff}, and the values of the photoinduced changes in the gap are normalized to the value of the gap at given temperature $\Delta(T)$.

In the pump-probe experiment, we recorded changes in the differential transmission of the probe pulse $\delta Tr(t_d)$, which are then converted into the changes in the (effective) gap, $\delta\Delta/\Delta$ (the procedure is elaborated below). Given that $h\nu_{\text{FEL}}$ is always larger than $2\Delta_\pi$, the photoexcitation leads to the Cooper-pair breaking and the $\delta\Delta/\Delta$ <0. The dependence of the maximum photoinduced gap suppression $|\delta\Delta/\Delta|_{max}$ on the absorbed energy density A is presented in Fig. 3.2. We can conclude that the characteristic energy density, required to fully suppress superconductivity, i.e., to achieve $\delta\Delta/\Delta$ = 100%, can be estimated by linear extrapolation of this dependence at the low absorbed energy densities. From this preliminary analysis, absorbed energy density required to suppress superconductivity ≈80 mJ/cm^3, which is on the order of the condensation energy. This implies that the excitation is distributed between the two superconducting condensates and the two gaps, Δ_π and Δ_σ, since we cannot break Cooper pairs in the σ-band

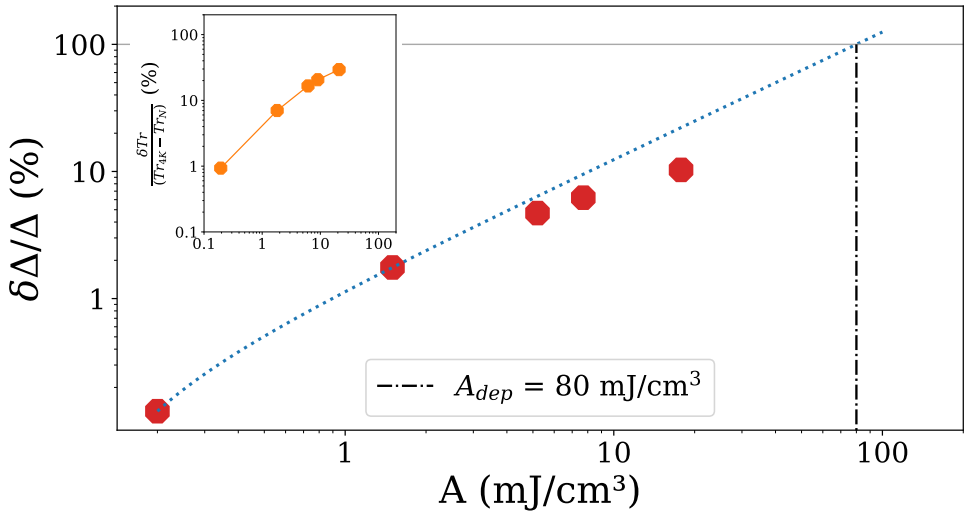

Figure 3.2: Photoinduced gap suppression $\delta\Delta/\Delta$ at 4.2 K as a function of absorbed energy density (red symbols). The energy, required to fully suppress superconductivity, i.e., to achieve $\delta\Delta/\Delta = 100\%$, can be determined by extrapolation of this dependence at low absorbed energy densities (dotted line). The value, obtained with such method, is on the order of magnitude of the superconducting condensation energy (vertical dash-dot line). Inset: maximum of the photoinduced changes in the $\delta Tr(t_d)$ as a function of absorbed energy density.

directly with $\Delta_\pi < h\nu_{\mathrm{FEL}} < 2\Delta_\sigma$ and the superconducting condensate in the σ-band creates 90% of the condensation energy, $E_c = \frac{1}{2}N_\sigma\Delta_\sigma^2 + \frac{1}{2}N_\pi\Delta_\pi^2$.

Assuming the T^* model, we attribute the $\delta Tr(t_d)$ to the photoinduced changes in the effective superconducting gap $\delta\Delta_{\mathrm{eff}}(t_d)$ by applying the following procedure:

i) with the temperature dependence of transmission known (Fig. 3.1a), we can assign effective temperature T_{eff} to each value of photoinduced changes in transmission $\delta Tr(t_d)$ (Fig. 3.3a), thus, obtaining $T_{\mathrm{eff}}(t_d)$ (Fig. 3.3b);

ii) using the temperature dependence of the effective gap (Fig. 3.1b), and assuming that $\Delta(t_d) = \Delta(T_{\mathrm{eff}}(t_d))$, we obtain the photoinduced changes of the (effective) gap $\delta\Delta(t_d, T_{base})$ (Fig. 3.3c).

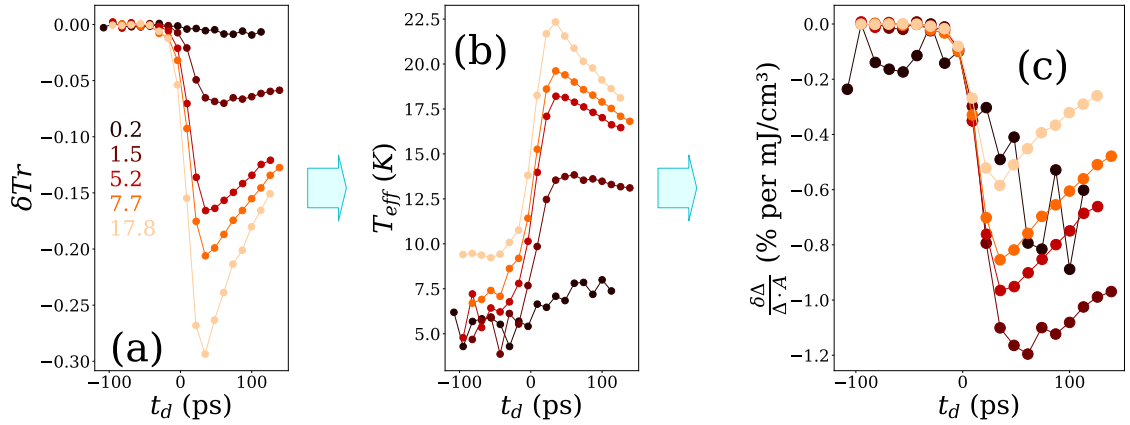

Figure 3.3: Example of conversion from $\delta Tr(t_d)$ to $\delta\Delta(t_d)$ at base temperature 4.2 K for ν_{FEL} = 2.7 THz. **a** Time-resolved changes in transmission of the probe pulse; **b** extracted time evolution of the T_{eff} (here the continuous heating effect leads to an increase in T_{eff} at negative time delays.) **c)** calculated relative changes in the gap normalized to absorbed energy density. Different colors of the curves represent different excitation densities (in mJ/cm^3 in the panel **a**).

Excitation with $h\nu_{\mathrm{FEL}} > 2\Delta_\pi$, as in our case, results in Cooper pair breaking, with the photoinduced gap suppression expected to be proportional to the absorbed energy density. Thus, dividing the relative gap suppression by the absorbed energy density (A), i.e., $\frac{\delta\Delta(t_{\mathrm{d}})}{\Delta(T)A}$ (in % per $\frac{mJ}{cm^3}$), allows us to emphasize the non-linear behavior of the THz driven gap dynamics.

Figure 3.4 presents selected traces of the induced SC state suppression and recovery dynamics, recorded at the base temperature $T = 4.2\ K$ for different A and for $\nu_{\mathrm{FEL}} = 1.5$ THz (panel **a**), 2.1 THz (panel **b**) and 2.7 THz (panel **c**). The presented traces demonstrate the evolution of the *effective* superconducting gap, Δ, as a function of time delay t_{d}, or more precisely $\frac{\delta\Delta(t_{\mathrm{d}})}{A\cdot\Delta(T)}$, where $\delta\Delta(t_{\mathrm{d}}) \equiv \Delta(t_{\mathrm{d}}) - \Delta(T)$, and $\Delta(T)$ is the equilibrium value of the effective gap at the sample temperature T. Here, $\delta\Delta(t_{\mathrm{d}})$ is obtained from the recorded pump-induced changes in the transmission of the probe pulse, $\delta Tr(t_{\mathrm{d}})$, combined with equilibrium $Tr(T)$ and assuming the T^*-model, as elaborated above.

The induced suppression of the superconducting gap in Fig. 3.4 is followed by the recovery of superconducting order on the timescale between ≈ 50 ps and several hundreds ps, depending on T and A. We fit the traces using a model considering the pair-breaking and recovery are exponential processes [84]

$$\frac{\delta\Delta(t_{\mathrm{d}})}{\Delta(T)\cdot A} = H(t_{\mathrm{d}}, \tau_{\mathrm{rec}}, \sigma) \times (C \cdot e^{-\frac{t_d}{\tau_{\mathrm{rec}}}} + B). \tag{3.2}$$

Here, τ_{rec} is the superconducting state recovery time, C is the amplitude of the normalized

gap suppression, and B corresponds to the residual gap suppression at large time delays as a result of the bolometric response. The rise-time of the recorded transient is accounted for by $H(t_d, \tau_{rec}, \sigma)$, a Heaviside function convoluted with the Gaussian pulse with pulse width of σ [84]. Note that σ can be larger than the resolution limit of $\sqrt{2}\tau_{FEL}$, where τ_{FEL} is the duration of the THz pulse. In this case, one can use $\sigma^2 = \tau_{PB}^2 + 2 \cdot \tau_{FEL}^2$ to estimate the intrinsic pair-breaking time τ_{PB}.

Several important observations can be made by visual comparison of datasets in the Figure 3.4 a-c:

i) τ_{rec} is similar for different ν_{FEL} and shows excitation and temperature dependence;

ii) rise time of the photoinduced gap suppression, σ, depends on ν_{FEL}, being approximately resolution limited at $\nu_{FEL} = 1.5$ THz while being longer for $\nu_{FEL} \geq 2.1$ THz;

iii) over a large range of excitation densities (≈ 2 orders of magnitude) the gap suppression amplitude (i.e., maximum suppression of the gap, corresponding to the negative of the pump-probe signal) displays a non-linear dependence on A.

iv) the gap suppression amplitude shows an increasing trend with increasing the ν_{FEL}. However, given the large uncertainty in the absolute value of absorbed energy density due to the high reflectivity of MgB_2 and the FEL mode quality, such observation should be considered carefully.

To quantify the dynamics as a function of temperature and excitation density, we performed systematic T- and A- dependent studies by recording transients (most were obtained by averaging several traces) at different base temperatures and absorbed energy densities for each ν_{FEL} and analyzed them using the fitting procedure described above. The high repetition rate of the FEL results in a continuous heating of the sample, which is taken into account (all the quoted temperatures below include the temperature rise due to the continuous heating, see Appendix B for details). As critical temperatures of samples investigated in different beamtimes varied between ≈ 31 K and ≈ 36 K, we present the T-dependent data as a function of reduced temperature T/T_c. The highest dynamic range and signal-to-noise ratio was obtained at $\nu_{FEL} = 2.7$ THz have, thus we focus on studies in this configuration.

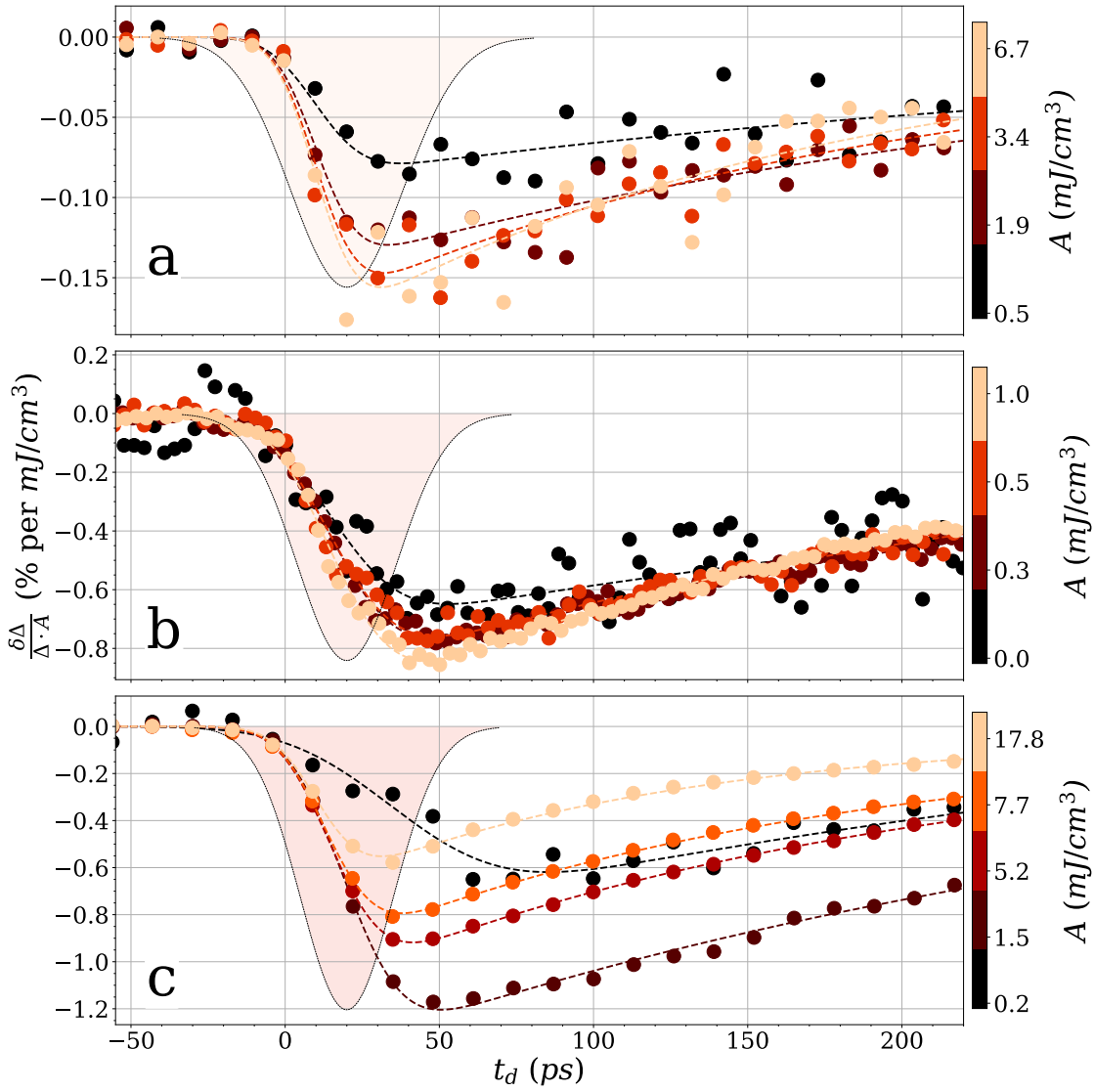

Figure 3.4: Traces presenting THz driven gap dynamics $\frac{\delta\Delta(t_d)}{\Delta(T)\cdot A}$ recorded at the cryostat temperature T = 4.2 K for different ν_{FEL}: **a** 1.5 THz, **b** 2.1 THz and **c** 2.7 THz pulses. The experimental datapoints are represented by solid symbols while dashed lines represent the fits to the data using Eq. 3.2. The shaded regions represent the cross-correlations of the THz pulses. Colorbars to the right depict the corresponding absorbed energy density for each of the traces. The relative amplitude of the gap suppression normalized to the absorbed energy density shows an increasing trend with increasing ν_{FEL}. While the relative errors in calculated absorbed energy density are negligible within datasets recorded at each ν_{FEL}, the absolute values of absorbed energy density are correct within a factor of 2 due to the large reflectivity of MgB_2 and the FEL mode quality.

In the following sections we discuss the T and A dependencies of several observables that we extract from fitting the gap dynamics with the Eq. 3.2. We start with the recovery time dynamics, which shows the behavior similar to early reports on NbN. Then, we demonstrate the rise-time dynamics of the pair-breaking process, where an unexpectedly slow response is observed at the lowest T and A. In Section 3.1.4 we present the dependence of the photoinduced gap suppression in the case of THz excitation and compare the results with those of optical pump–THz probe experiment.

3.1.2 RECOVERY DYNAMICS OF THE SUPERCONDUCTING STATE FOLLOWING PHOTOINDUCED EXCITATION

After initial build-up of pump-induced gap suppression, the superconducting state exhibits exponential recovery with the timescale depending on base temperature and absorbed energy density. Figure 3.5 shows dependence of τ_{rec} on temperature and absorbed energy density A. As shown in Fig. 3.5, at the lowest temperatures τ_{rec} decreases with A, mimicking the intrinsic bi-molecular kinetics of the QP recombination. Below $\approx$ 15 K the recovery dynamics is both temperature and excitation density dependent while above 20 K τ_{rec} reaches constant value of $\approx$ 60 ps. Given the fact that the early stage of the gap dynamics in MgB_2 reveals a delayed pair-breaking with build-up of quasi-equilibrium between QPs and HFP as discussed below, it is clear that the recovery dynamics is determined by the decay of the HFP population. The results are consistent with earlier optical pump–THz probe studies on NbN [5, 47] and MgB_2 [37] and can be described within the Rothwarf-Taylor phonon bottleneck scenario [5, 48, 57], where the recovery is governed by the decay of the HFP population.

We note here, that, given the fact that similar experimental observations were made on NbN [47], and the dynamics was accounted for in terms of the RT bottleneck model, we will not elaborate on the arguments further. An interested reader can consult Refs. [5, 47].

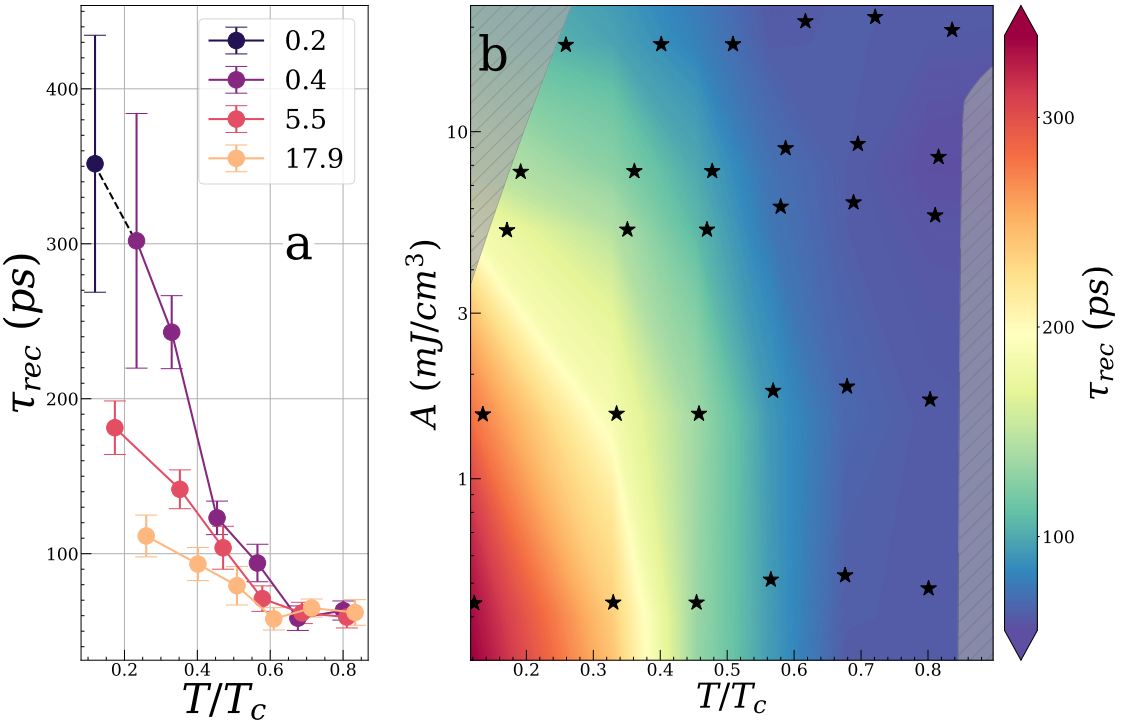

Figure 3.5: τ_{rec} for different A obtained at ν_{FEL} = 2.7 THz. **a** as a function of temperature at several A (in mJ/cm^3); **b** all collected data presented in the contour plot versus absorbed energy density and temperature. Star-like marks in the color plot represent the data points. Areas that could not be accessed in the experiment are masked with grey.

3.1.3 Initial pair-breaking dynamics following THz excitation

Let us now focus on the rise-time dynamics reflecting the THz-driven pair-breaking processes shown in Figure 3.6. Panel **a** represents the comparison of the rise time, σ (see Section 3.1.1), versus absorbed energy density for different ν_{FEL}. Panel **b** shows temperature dependence of the rise time of the photoinduced gap reduction σ at 2.7 THz at several absorbed energy densities A. It should be noted that the time resolution of our experiment is $\approx \sqrt{2} \cdot \tau_{\mathrm{FEL}} \approx 20$ – 25 ps depending on frequency (assuming the transform-limited pulses, see Section 2.2.3) so we consider the rise time approaching this value to be resolution limited (shown as a grey area in Fig. 3.6).

The rise time seems to exhibit photon energy dependence at comparable absorbed energy densities (Fig. 3.6**a**), increasing with photon energy. One can see that the rise time for ν_{FEL} = 1.5 THz is resolution-limited while for ν_{FEL} = 2.1 THz the rise time is close to 40 ps at low A and low T, being clearly above the resolution limit.

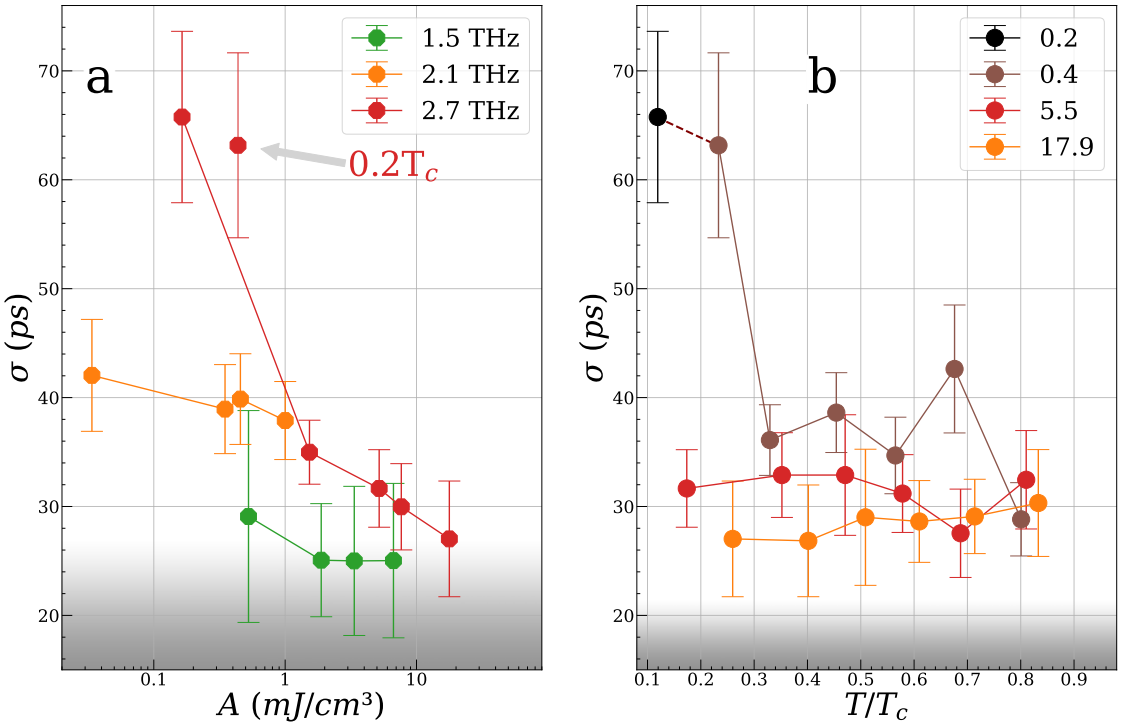

Figure 3.6: Rise time of the photoinduced changes, σ as a function of: **a** absorbed energy density at the 4.2 K cryostat temperature for different ν_{FEL}, **b** temperature and A at ν_{FEL} = 2.7 THz. Grey areas shade the temporal resolution limit, which is $\sqrt{2}\cdot\tau_{1.5\mathrm{THz}} \approx 26$ ps in panel **a**, and $\sqrt{2}\cdot\tau_{2.7\mathrm{THz}} \approx 21$ ps in panel **b**.

Moreover, the slowing down of the rise-time dynamics to ≈ 70 ps below 0.2·T$_c$ at the lowest excitation density at 2.7 THz is clearly resolvable (Fig. 3.6b). Above 12 K and at high absorbed energy density values the rise time remains constant on the order of ≈ 25 ps within the error bars. The delayed pair breaking at low T and A for excitation with ν_{FEL} = 2.7 THz is consistent with the fact that the photon energy in the case of 2.7 THz is higher than 4Δ. Thus, the quasiparticles formed by absorbing of the photon by the Cooper pair have an excess of energy higher than 2Δ. This extra energy can be released via emission of 2Δ phonon, and the superconducting gap can be further reduced via absorption of this phonon by the CP at the initial stage after photoexcitation.

In time-resolved studies with optical excitation on MgB_2 [37], $Pr_{1.85}Ce_{0.15}CuO_{4-\delta}$ [85, 86] and NbN [47] such observation was attributed to delayed pair-breaking by HFPs, emitted during the avalanche scattering process of hot electron relaxation. On the other hand, in the experiments with THz pumping no such delayed response has been observed.

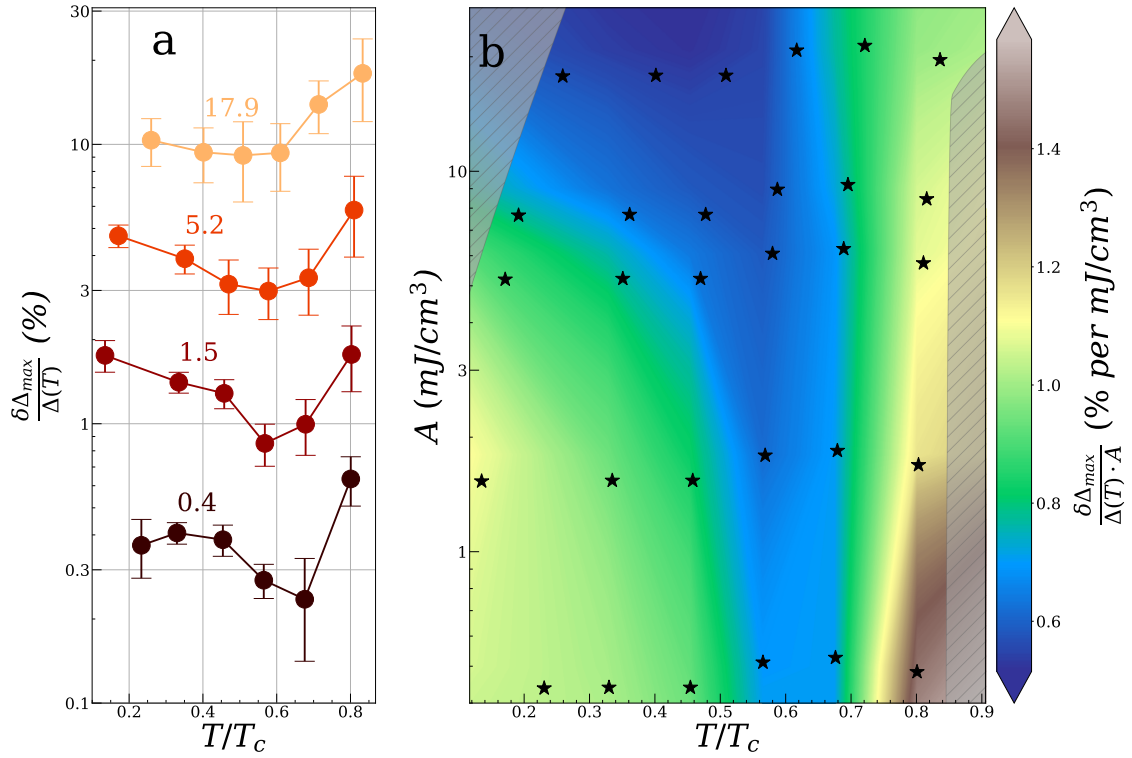

Figure 3.7: The amplitude of photoinduced gap suppression for ν_{FEL} = 2.7 THz. **a** as a function of temperature at several A (in mJ/cm^3); **b** all collected data presented in the contour plot versus absorbed energy density and temperature. Star-like marks in the color plot represent the data points. Areas that could not be accessed in the experiment are masked with grey.

3.1.4 PHOTOINDUCED SUPPRESSION OF THE SUPERCONDUCTING GAP

Figure 3.7 represents temperature and absorbed energy density dependence of the gap suppression amplitude $\frac{\delta\Delta_{max}}{\Delta(T)\cdot A}$ when pumping with 2.7 THz. The first remarkable feature is sub-linear dependence of gap suppression amplitude on absorbed energy density in the entire range of measured temperatures.

Another, and even more surprising observation is that the temperature dependence of gap suppression amplitude (for all absorbed energy densities except for the highest) has a minimum around 0.6·T_c instead of expected monotonic increase with temperature. The minimum in the T-dependence of $\frac{\delta\Delta_{max}}{\Delta(T)}$ suggests that an additional process competing with photoinduced suppression of superconductivity emerges at finite temperatures.

To find out if such unexpected behavior is a consequence of resonant excitation with THz pulses we performed optical pump – THz probe (OPTP) experiment where the superconductor was excited by femtosecond laser pulses at a wavelength of 800 nm (corresponding photon en-

ergy 1.55 eV). As opposed to THz excitation, NIR photons excite QPs from far below to far above the superconducting gap (ratio of the NIR photon energy and the gap energy is about 400). Hence, the superconductivity is suppressed via avalanche generation of HFPs and the resulting pair breaking is caused by releasing the excess energy by high-energy QPs. This scattering process occurs on the picosecond timescale and results in establishing quasi-thermal distribution of photoexcited QPs. Given the fact, that such an avalanche process involves multiple scattering events, one expects the QP distribution to be much closer to thermal one than in the case of THz pumping.

The temperature dependence of the gap suppression in the case optical excitation as well as the T and A dependencies of the rise time and recovery time will be shown in the next Section 3.2.

3.2 Comparison of spectrally-integrated THz response for Optical (NIR) and THz excitation

We performed additional measurement using THzTDS complemented with NIR-pump (λ_{pump} = 800 nm). In this section, we will present the spectrally-integrated time-resolved data, where the pump-induced changes in the broadband THz-probe electric field, $\Delta E_{\text{THz}}(t^0_{THz}, t_d)$, are measured at the fixed characteristic point in the time delay of the probe THz electric field, t^0_{THz}, as a function of pump-probe time delay t_d with respect to the THz pulse. As we discussed in Section 2.2.1, for measuring the pump-probe changes in the superconducting response, the zero-crossing of the probe electric field field between maximum and minimum of the THz pulse provides the best sensitivity as the characteristic point (Fig. 3.8). Prior to the pump-probe experiment we recorded the value of the electric field $\Delta E(t^0_{THz})$ as a function of temperature.

To obtain the relative pump-induced changes in the superconducting gap, $\frac{\delta\Delta(t_d)}{\Delta}$, from the $\Delta E_{\text{THz}}(t_d)$ transients in the spectrally-integrated pump-probe experiment, we apply the conversion procedure, similar to the one described in Section 3.1.1. The differential transmission is substituted with the differential electric field at zero-crossing,
$\Delta E(t^0_{THz}, T) \equiv -\big(E(t^0_{THz}, T) - E(t^0_{THz}, T_{\text{c}})\big)$, that has similar BCS temperature dependence shown in Fig. 3.8**b**. Assuming the T*-model, we assign effective temperature T_{eff} to each value of photoinduced changes in transmission $\Delta E_{\text{THz}}(t_d)$, obtaining $T_{\text{eff}}(t_d)$ and further converting to $\Delta(t_d) = \Delta(T_{\text{eff}}(t_d))$.

Figure 3.9 presents the amplitude of the gap suppression following NIR excitation in the same coordinates as in the Fig. 3.7 to provide clear comparison between the optical and THz excitation. We can see that at low absorbed energy densities the temperature dependence of the

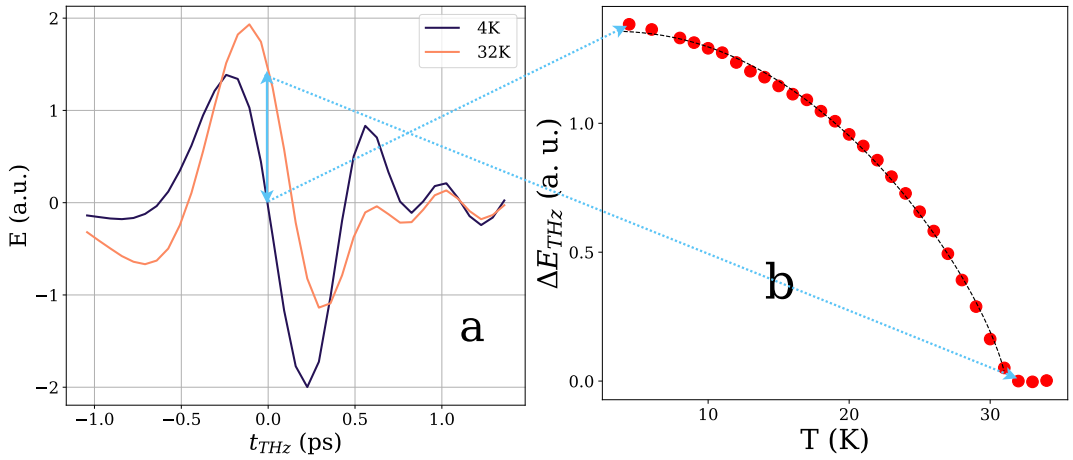

Figure 3.8: **a** Inductive response of a superconductor, manifested in the phase shift in the THz pulses, transmitted through the sample in the superconducting and normal state. Zero-crossing at 4 K between maximum and minimum of $E(t_{THz})$ is used to obtain the $\Delta E_(t_d)$. **b** Temperature dependence of the differential value of the electric field, $\Delta E(t^0_{THz}, T) \equiv -\left(E(t^0_{THz}, T) - E(t^0_{THz}, T_c)\right)$. Red circles are the experimental data, black dashed line is the fit with Eq. 3.1. The T_c of this MgB_2 thin-film sample ≈31 K.

gap suppression follows the expected trend – a monotonous increase as the superconducting condensate density is being thermally suppressed. A small dip in the T-dependence of the gap suppression around 0.6·T_c for the case of optical pumping is present at $A \geq 36$ mJ/cm^3, yet the effect is much weaker, i.e., by a factor of ~4 smaller than in the case of THz pumping (see Fig. 3.7).

The results suggest that there is a major difference in the dynamics of the (effective) superconducting gap following either of the two types of excitation – resonant THz and off-resonant optical. Given that we deliberately kept the experimental conditions, such as the range of temperatures and excitation energy densities, to be similar between the measurements, the observed difference should be caused by the distinction in the processes, occurring after the excitation. We argue that the above-gap THz pumping at finite temperatures together with pair-breaking process excites also the thermally-created QPs thus giving rise to their non-thermal distribution, which can persist on the tens-of-picosecond timescale. Following the Eliashberg scenario, the non-thermal QP distribution can lead to an enhancement of superconductivity that in our case competes with the photoinduced pair-breaking.

To provide further comparison of the gap dynamics between THz and optical pumping, we

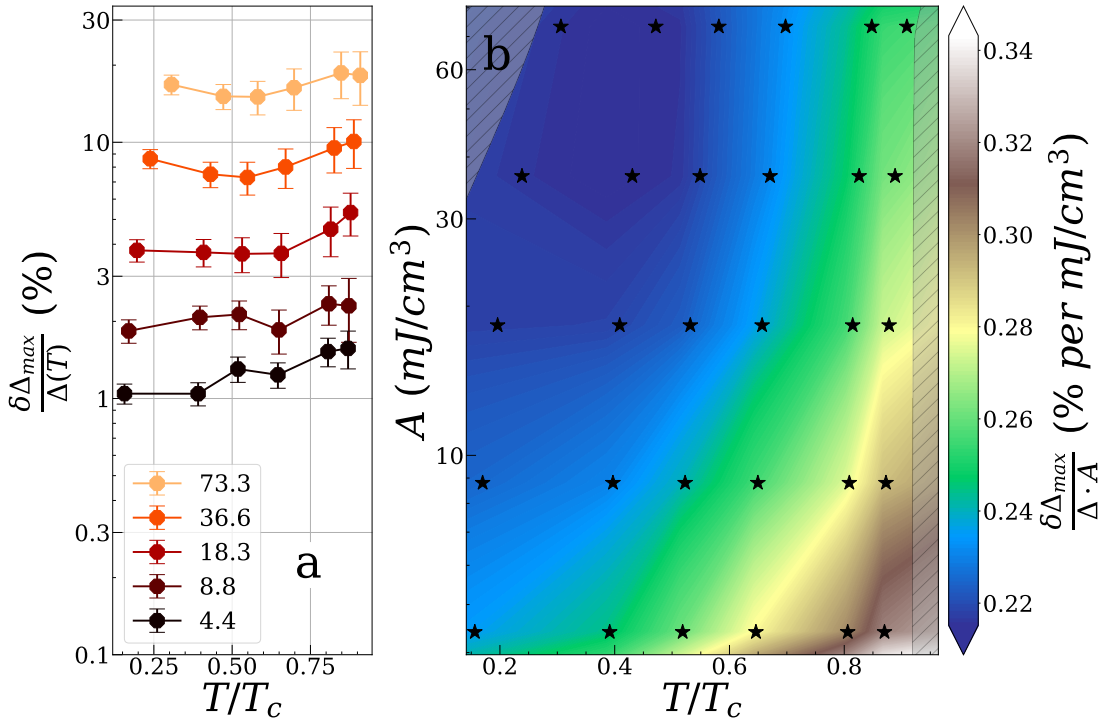

Figure 3.9: The amplitude of photoinduced gap suppression in the case of excitation with NIR femtosecond laser pulses. **a** As a function of temperature at different A (in mJ/cm^3). **b** All collected data are presented in the contour plot versus absorbed energy density and temperature. Star-like marks in the color plot represent the data points. Areas that could not be accessed in the experiment are masked with grey.

analyze the experimental results of T- and A-dependence of the recovery time of the superconductivity and the pair-breaking rise time for the case of optical excitation. The dynamics of the effective gap of MgB_2 at low temperatures, following the optical excitation, is presented in Fig. 3.10 for different absorbed energy densities. We can see that the dynamics resembles the one in the NbTHzPP, with the rise-time and recovery-time speeding up with increasing absorbed energy density (similar to the case of THz excitation).

The $T - A$ dependence of the recovery time for the case of optical excitation is shown in Figure 3.11. We can see that the recovery dynamics in the OPTP experiment shows a similar trend as in the case of THz excitation slowing down at low A and T and reaching approximately constant value of ~ 50 ps at high temperatures and high absorbed energy densities. This is again consistent with the RT scenario and manifests realization of the phonon-bottleneck regime.

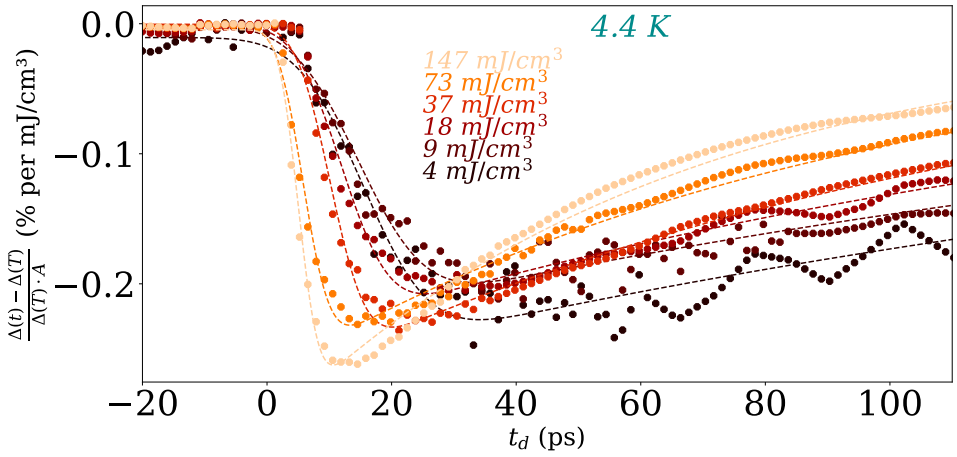

Figure 3.10: Traces, presenting optical pump-induced gap dynamics $\frac{\Delta(t_d)-\Delta(T)}{\Delta(T)\cdot A}$ recorded at the cryostat temperature T = 4.4 K. The experimental datapoints are represented by solid symbols while dashed lines represent the fits to the data using Eq.(1). The relative amplitude of the gap suppression normalized to the absorbed energy density is of the same order of magnitude as in the case of THz pumping.

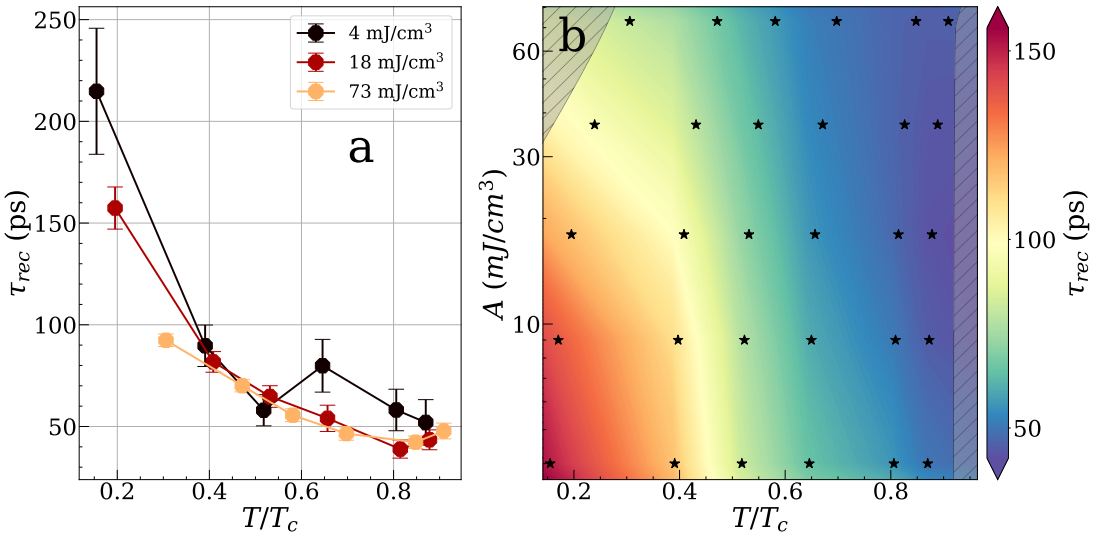

Figure 3.11: The dynamics of the superconducting state recovery in MgB_2 driven by the NIR excitation. **a** τ_{rec} as a function of temperature at several A (in mJ/cm^3); **b** all collected data presented in the contour plot versus absorbed energy density and temperature. Star-like marks in the color plot represent the data points. Areas that could not be accessed in the experiment are masked with grey.

The dynamics of the CP breaking presented in Fig. 3.12 resembles the case of the resonant excitation with THz pulses. However, the timescale of the rise-time of the gap suppression for optical pump is substantially lower. Our results on the rise-time dynamics are also consistent with earlier studies [37], where the T- and A-dependence of the pair-breaking rise time was reported for the first time.

In the case of the optical excitation of a superconductor, high-energy QPs can release their energy to phonons with higher frequencies than those, available in the case of relaxation of QPs upon THz excitation. Especially, an optical E_{2g} mode at ~70 meV [87, 88] has been found to be strongly coupled with the superconducting condensate. Thus, faster pair-breaking process in the case of optical pumping could be attributed to the pair-breaking by optical phonons, as opposed to the case with THz excitation, where phonons, that could be generated by relaxation of excited QPs via HFP emission, are the zone-edge acoustic phonons. Thus the different rate of the CP-breaking may be attributed to the different electron-phonon coupling strengths of acoustic and high-frequency optical phonons.

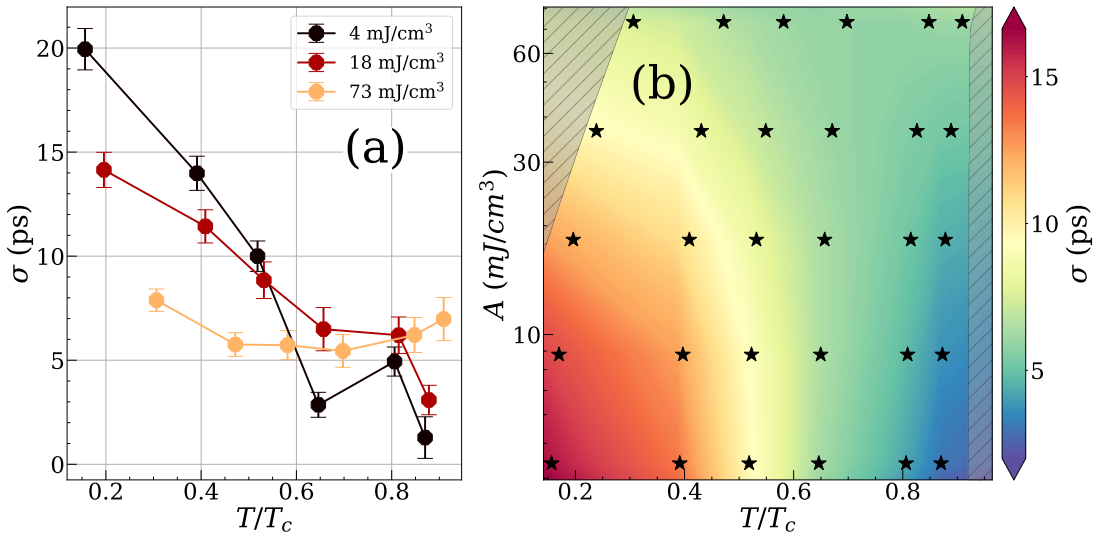

Figure 3.12: The pair-breaking dynamics for NIR excitation. **a** as a function of temperature at several A (in mJ/cm^3); **b** all collected data presented in the contour plot versus absorbed energy density and temperature. Star-like marks in the color plot represent the data points. Areas that could not be accessed in the experiment are masked with grey.

3.2.1 NARROW-BAND THz PUMP – SPECTRALLY-INTEGRATED THz PROBE EXPERIMENT

In this Section, we will compare the gap dynamics obtained in the narrow-band THz pump – spectrally-integrated THz probe with NbTHzPP and OPTP data. We performed similar studies on the same MgB_2 sample in the same setup as in the OPTP experiment but using narrow-band THz_{FEL} pulses at ν_{FEL}= 2.7 THz for excitation. The phase-stable broadband THz radiation, generated by the femtosecond NIR pulses, was used to probe the spectrally-integrated response. The femtosecond laser system with the pulse repetition rate of 250 kHz was synchronized with the FEL, see details in Section 2.2.2. Due to losses in the experimental layout, the maximum absorbed energy density was ≈4 mJ/cm^3, from the other hand, low S/NR limited the minimum excitation density to ≈0.4 mJ/cm^3. Therefore, the full comparison with NbTHzPP and OPTP experiments over a large range of excitation densities is not possible, and we use the results of this experiment to double-check our observation in Fig. 3.7.

The gap dynamics was extracted from the spectrally-integrated pump-probe transients using the routine, described in the beginning of the Section 3.2. Figure 3.13 represents the dynamics of the superconducting gap suppression following excitation with FEL THz pulses for ν_{FEL}= 2.7 THz. Although the S/NR of these data is quite low, the main idea to perform this mea-

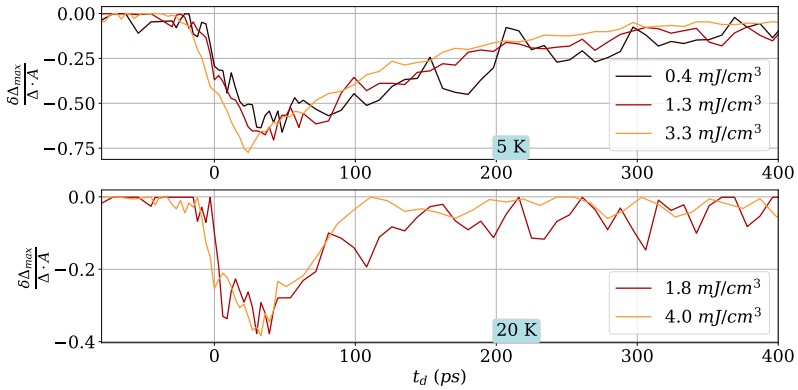

Figure 3.13: THz pump-induced gap dynamics obtained from pump-induced changes in the spectrally-integrated THz probe transmission. The dynamics is similar to the observed in the narrow-band THz pump-probe experiment. One can clearly see, that the rise-time exhibits the delayed processes at low T. The temporal resolution in this experiment is higher because it is limited only with the pulse duration of the pump pulse and not the cross-correlation of the pump and the probe as in the NbTHzPP experiment.

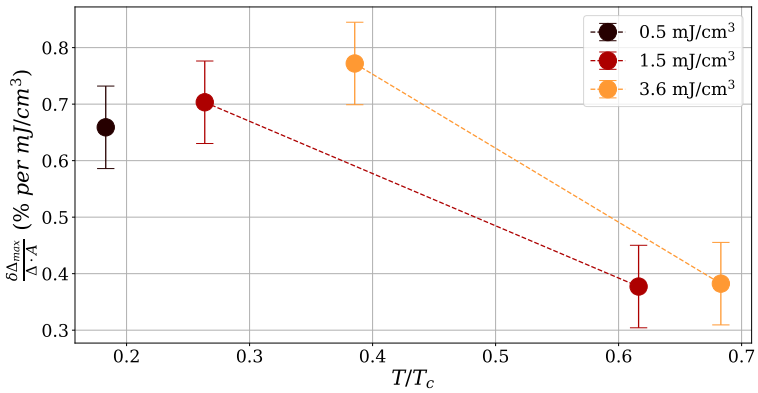

Figure 3.14: Maximum of the photo-induced gap suppression as a function of T at different absorbed energy densities for the THz pumping. A decrease of the gap suppression at $0.6{\cdot}T_c$ is observed, similar to that in the case of narrow-band THz pump-probe (Fig. 3.7). The values of the pump-induced gap suppression are also similar to the case of studies in the narrow-band THz pump-probe configuration.

surement was to confirm, if the non-trivial temperature dependence of the gap suppression, discovered in NbTHzPP experiment, is a feature of the resonant excitation with narrow-band THz pulses. In Fig. 3.14 we can see that the gap suppression amplitude at 20 K is ≈2 times lower than at 5 K.

3.3 SIMULATION OF THE DYNAMICS OF THE SUPERCONDUCTIVITY SUPPRESSION USING THE ROTHWARF-TAYLOR MODEL

To further support the claim that it is the resonant excitation that leads to a non-thermal QP distribution, which is, in turn behind the process of the enhancement of superconductivity, we performed the simulation of the gap dynamics using the Rothwarf-Taylor bottleneck model. The goal of the simulation is to find out whether the observed behavior in the THz pump-probe experiment, in particular, the observed minimum un the pair-breaking efficiency at $0.6{\cdot}T_c$, can perhaps be attributed to a result of redistribution of the absorbed energy between the QPs and HFPs. The full derivation of the time evolution of QP and HFP concentrations, assuming the phonon-bottleneck scenario [48] and neglecting the decay of HFPs, is given elsewhere [5, 89].

In Section 1.6.3 we introduced the coupled equations, describing an energy exchange between the QPs and HFPs. Following the derivations in [57], we introduced dimensionless QP

and HFP concentrations, $q \equiv Rn/\beta$ and $p \equiv RN/\beta$, where n and N are the QP and HFP concentration, β is the probability for pair-breaking by HFP absorption and R is the bare QP recombination rate with the creation of a HFP. Here we present an analytical solution of the coupled equations, considering only early-time dynamics, where the decay of the HFP population can be neglected. The resulting (dimensionless) QP concentration as a function of dimensionless time $\theta \equiv \beta t$ is given by

$$q(\theta) = \left[-\frac{1}{4} - \frac{\xi^{-1}}{2} + \frac{\xi^{-1}}{1 - K\exp(-\theta/\xi)} \right]. \tag{3.3}$$

Here, $\xi^{-1} = \sqrt{1/4 + 4p_0 + 2q_0}$ and $K = \frac{(4q_0+1)-2\xi^{-1}}{4q_0+1)+2\xi^{-1}}$ where (p_0, q_0) are the initial conditions.

For comparison on the qualitative level, we neglect thermally-excited QPs, (i.e., we consider that the concentration of photoexcited QPs is large compared to the thermal ones). In the first approximation, we can also assume that photoinduced gap suppression is proportional to the concentration photoinduced of QPs, i.e., $\delta\Delta \propto n_{QP}^{PE}$. This allows us to compare the experimental results on photoinduced gap suppression with the results of simulation.

The parameters R and β are not known precisely for MgB_2, where earlier OPTP studies suggest that $R = 100 \pm 30$ ps^{-1}u.c.V.$^{-1}$ and $\beta^{-1} = 15 \pm 2$ ps [37]. These values were obtained considering MgB_2 being a single-gap superconductor. Additionally, the experimental parameters such as film thickness were just roughly estimated. Taking the quoted values as a starting point, we performed the simulation of photoinduced concentration of QPs, by varying the value of R over a wide range. The results of the simulation are represented in four panels of the Fig. 3.15. We can immediately see that for different values of R the gap suppression amplitude has a sublinear dependence on A in the entire temperature range. Indeed, similar behavior we observe in both OPTP and THz NbTHzPP experiments. But, in contrast to the temperature dependence of the gap suppression driven by the narrow-band THz pulses, we do not see a minimum in the pair-breaking efficiency at $\approx 0.6 \cdot T_c$. Instead we observe a smooth and monotonous increase in the gap reduction, similar to our results obtained by NIR excitation, with details depending on chosen value of R.

The simulation shows that accounting for the interplay between QPs and HFPs does not result in a non-trivial temperature dependence of the photoinduced gap suppression, and hence, of the gap suppression. We can see that qualitatively the results of simulation are similar to the gap suppression in the case of optical excitation (Fig. 3.9). This fact provides further support to the idea that in the case of THz pumping an additional process competes with THz-driven breaking of Cooper pairs.

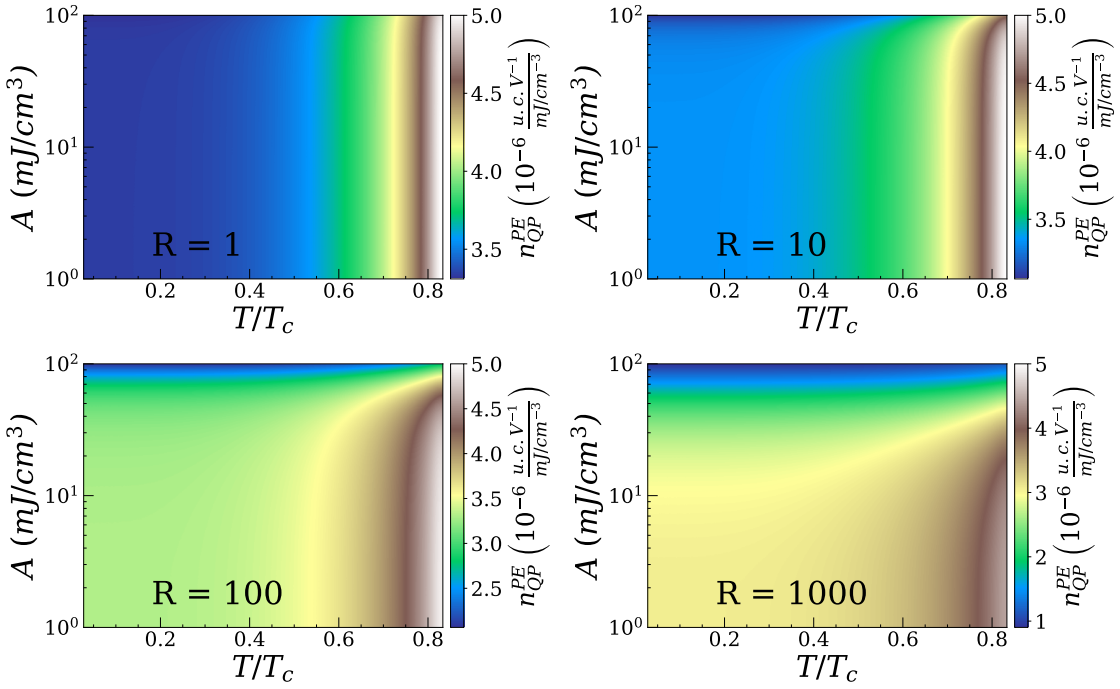

Figure 3.15: Concentration of photoexcited QPs, normalized to absorbed energy density, as a result of simulation within the Rothwarf-Taylor model as a function of temperature and absorbed energy density at four different values of R (in $\frac{u.c.V.}{ps}$)

3.4 SUMMARY

To summarize, we investigated the energy gap dynamics in the two-band BCS superconductor MgB_2 upon excitation with narrow-band THz pulses. The completeness of our study allowed us to reveal novel observations like the dependence of the dynamics of photoexcited pair-breaking process on temperature and absorbed energy density as well as on the photon energy of the excitation. The recovery dynamics of the superconducting state proceeds within the Rothwarf-Taylor phonon-bottleneck scenario, where dynamics is governed by the decay of the HFP population with recovery time decreasing with increasing of both T and A.

The most fascinating result of our investigation is the non-trivial behavior of the photoexcited gap suppression amplitude. At first, the gap suppression indicates sub-linear dependence on absorbed energy density. This observation is consistent with the simulation within the phenomenological Rothwarf-Taylor model. However, in the simulation we cannot reproduce the observation of the minimum in pair-breaking efficiency, observed in the temperature dependence of the gap suppression. We attribute presence of the minimum in the T-dependence of the THz-pump-induced gap suppression to a process competing with breaking of CPs, which

gives rise to a transient enhancement of superconductivity.

We argue that the underlying process is the Eliashberg-type enhancement of superconductivity due to highly non-thermal QP distribution caused by narrow-band THz excitation.

Additionally, we performed OPTP studies, allowing the comparison of the main parameters of the photoinduced gap suppression such as the pair-breaking dynamics, amplitude of the gap suppression and the recovery time of the superconducting state. The $T-$ and $A-$dependencies of the rise time and the recovery time are similar in general to the case of resonant THz excitation. However, the rise-time upon optical excitation proceeds on a substantially faster timescale. We attribute this to the difference in pair-breaking rates by high-frequency optical phonons (generated via relaxation of "hot" electrons in the case of optical excitation) and acoustic phonons (generated via cooling of QPs excited by the THz pulse with $h\nu_{FEL} \geq 4\Delta_\pi$). The temperature dependence of the photoinduced gap suppression amplitude does not show a minimum around $0.6 \cdot T_c$. This fact confirms our suggestion that it is the non-thermal QP distribution as a result of the THz excitation that gives rise to a process competing with pair breaking.

The observed enhancement effects (considering reducing of the pair-breaking efficiency by a factor of ≈ 2) are much more pronounced than in the early studies with continuous microwave irradiation of a superconductor [44]. There, the observed increase in T_c was on the order of a few percents.

Finally, comparing the pair-breaking efficiency for different ν_{FEL}, we can see that the gap suppression decreases with decreasing the pump frequency (Fig. 3.4), i.e., for excitation with lower photon energy more energy is required to suppress superconductivity. However, it should be noted that the absolute uncertainty in absorbed energy density (directly contributing to the uncertainty of the normalized gap suppression, $\frac{\delta\Delta}{\Delta \cdot A}$) is too large to make a definitive statement. To clarify the dependence of pair-breaking efficiency on ν_{FEL}, the systematic studies with higher precision of defining the absorbed energy density are required.

To further investigate these intriguing effects, experiments with narrow-band sub-gap pumping are required, with the pump frequency below 1 THz. This would enable sub-gap pumping for temperatures closer to T_c, where the concentration of thermally excited QPs is large and the effect of the enhancement of superconductivity can be expected to be the largest.

CHAPTER 4

TIME AND SPECTRALLY RESOLVED CONDUCTIVITY DYNAMICS OF MgB_2

It came as a surprise that optical spectroscopy developed as an important experimental tool for the determination of band structure. First, the absorption and reflection bands of crystals are broad and apparently featureless functions of the photon energy when this is greater than the band gap. Second, direct interband absorption of a photon will occur at all points in the Brillouin zone for which energy is conserved. <...>
Three factors unraveled the spectra: The broad bands are not like a spectral line greatly broadened by damping, but the bands convey much intelligence which emerges when derivatives are taken of the reflectance; derivatives with respect to wavelength, electric field, temperature, pressure, or uniaxial stress, for example. The spectroscopy of derivatives is called modulation spectroscopy.

C. Kittel. Introduction to Solid State Physics [90]

4.1 INTRODUCTION

In this Chapter we present the results of the systematic studies of the time- and spectrally-resolved dynamics in MgB_2. The experimental technique was introduced in the Section 2.2.2. In contrast to the spectrally-integrated scans or the scans, performed in the narrow-band THz pump-probe configuration, the probe signal is represented over a two-dimensional time-delay landscape: t_{THz}, the time-delay between the broadband phase-stable THz pulse and the sampling femtosecond NIR pulse, as discussed in the Section 2.1, and t_d, the time-delay between the probe THz pulse and the excitation THz (or NIR) pulse. Thus, the data acquisition and processing becomes time consuming, especially, in the case of the THz FEL experiment because of the lower signal-to-noise ratio, difficulties with the synchronization of the FEL and the femtosecond laser system and the complexity of the experimental setup. To the best of our knowledge, we present the first time- and spectrally-resolved studies of superconductors, resonantly excited with the narrow-band THz radiation and probed with the broadband THz radiation.

The motivation to conduct such studies includes several aspects:

a) the photoinduced dynamics of the superconducting state with spectral resolution allows to verify the usage of the T*-model for the analysis of the gap dynamics, i.e., to answer the question if the (global) impact of the above-gap photoexcitation of a superconductor is an increase of the temperature of coupled QP and HFP subsystems (as demonstrated in the OPTP experiment [37]);

b) the modulation nature of the pump-probe spectroscopy can enable access to the spectral features, which are not distinguishable in the equilibrium spectroscopy, i.e., the multi-gap dynamics;

c) using narrow-band THz and optical excitation in the pump-probe THz spectroscopy on the same sample allows for direct comparison of the excited states of a superconductor driven by the two types of excitation and may reveal, if the non-thermal distribution driven by the resonant excitation has an imprint on the spectrally-resolved dynamics.

Because of the time limitation in the large-scale facility experiment, obtaining the spectrally-resolved dynamics for many points of pump-probe time-delay, t_d, was not possible. Hence, the photoinduced changes in the transmitted electric field of the broadband THz probe signal, $\Delta E(t_{THz})$, were recorded at several fixed values of t_d. In combination with the spectrally-integrated photoinduced response, discussed in the previous sections, a full picture of the dynamics of the superconducting order, following the excitation can be portrayed.

4.2 EQUILIBRIUM OPTICAL CONDUCTIVITY OF MgB_2

The ground state of the conventional single-gap superconductors like NbN [74] is well understood within the BCS theory, and their experimental optical conductivity, representing characteristic features, i.e., $\sigma_1(0 < \nu < 2\Delta/h) = 0$ and $\sigma_2(\nu \to 0) \to \infty$, can be accurately fitted with Mattis-Bardeen formulas (see Section 1.4.3), providing information on $\Delta(T)$ as well as $\Delta(t_d)$ in the pump-probe experiment. However, in the case of multi-band superconductors the situation becomes more complicated, and even the equilibrium optical conductivity is not straightforward to interpret. Here, no fully established theory exists to describe $\sigma(\nu)$ of a two-band superconductor, including the interband coupling.

The MgB_2 sample that we investigated in this experiment was similar to the one described in the Chapter 3, yet the film thickness was 10 nm and the MgO substrate thickness was 0.33 mm. The fact that the T_c of such a thin film is equal to 31 K indicates the high quality of the sample.

Prior to the time-resolved THzTDS we performed fine characterization of the equilibrium optical conductivity of the MgB_2 film as a function of temperature. Figure 4.1, panels **a** and **b**, represent $\sigma_1(\nu)$ and $\sigma_2(\nu)$, respectively, at several selected temperatures, Figure 4.1**c** demonstrates $\sigma_1(4K)$ in the superconducting state normalized to $\sigma_1(32K)$ in the normal state.

As we can see the optical conductivity shows noticeable differences from the conventional single-gap superconductor, namely, the real part of the low-temperature conductivity touches zero at ≈ 0.7 THz and increases upon lowering the frequencies. In the Mattis-Bardeen model, in the limit $T \to 0$, $\sigma_1 = 0$ in the frequency range $0 < \nu < 2\Delta/h$ (apart from $\sigma_1(\nu \to 0) \to \infty$), displaying a clear gap, and then gradually increases towards normal-state σ_1 at frequencies $\gg 2\Delta/h$. The imaginary part of the low-temperature optical conductivity of MgB_2 diverges towards low frequency as expected. However, it shows an inflection at ≈ 0.3 THz unlike in the Mattis-Bardeen model. These spectral features were observed in early studies on MgB_2 [78, 91] and the discussion regarding the origins of these features continues nowadays [92]. Furthermore, no clear evidence of Δ_σ is observed in equilibrium $\sigma(\nu)$ which was attributed to the fact that the scattering rate in the σ-band is smaller than $2\Delta_\sigma$ (i.e., the clean limit).

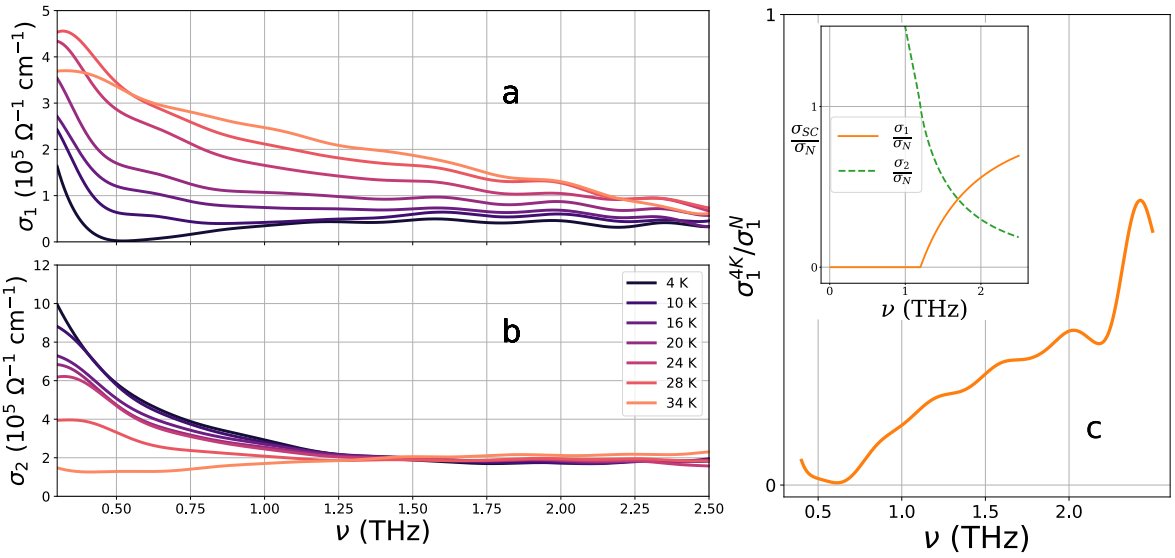

Figure 4.1: Left panels represent the optical conductivity of MgB_2 film at several temperatures. T_c of this sample ≈ 31 K. Panel **a** represents $\sigma_1(\nu)$, panel **b** represents $\sigma_2(\nu)$. Panel **c** represents $\sigma_1(\nu)$ in the superconducting state normalized to $\sigma_1(\nu)$ in the normal state. An inset in the panel **c** displays the optical conductivity, calculated by Mattis-Bardeen formulas for T → 0 (Section 1.4.3). An upturn in experimental $\sigma_1(\nu)$ at low frequencies (reported in MgB_2 earlier [78, 91]) is a deviation from the calculation in the context of the Mattis-Bardeen model.

In other words, the ground-state optical properties of MgB_2 is not fully understood, and no established model exists that would describe optical conductivity as a function of frequency with the two gaps and the interband coupling taken into account. Thus, it is unclear how to properly fit the experimental quilibrium optical conductivity and extract the, for example, the temperature dependence of the gap(s) (as it was done in the Ref. [47] for NbN).

The analysis of the spectral properties of a superconductor can also be done based on investigating the sample transmission in the superconducting state, $\mathcal{T}(\nu)$. This approach was used in the first optical studies of superconductors, providing information about the superconducting gap [2], as well as in [47] for NbN.

To exclude the metallic spectral response of the normal state from the consideration, we normalize the transmission in the superconducting state, $\mathcal{T}_{SC}(\nu)$, to that in the normal state, $\mathcal{T}_N(\nu)$, and operate with this transmission ratio, $\boldsymbol{TR} \equiv \mathcal{T}_{SC}(\nu)/\mathcal{T}_N(\nu)$. Fig. 4.2 presents the

temperature dependence of the equilibrium transmission ratio of MgB_2 film, $\boldsymbol{TR}_{eq}$, represented in different normalizations. Panel **a** shows the temperature dependence of $\boldsymbol{TR}_{eq} - 1$. A characteristic feature around 1 THz, where $\boldsymbol{TR}_{eq}(\nu) = 1$, shifts with increasing temperature to lower frequency. This feature is more pronounced in the plot, shown in the panel **b**, where the $\boldsymbol{TR}^{n}_{eq}(\nu, T) \equiv \boldsymbol{TR}_{eq}(\nu, T) / \boldsymbol{TR}^{max}_{eq}(\nu, T)$, i.e, the transmission ratio at each temperature is normalized to its maximum value at this temperature. The maximum in the transmission ratio is located around 1.8 THz at low temperatures. The temperature dependence of the characteristic feature in $\boldsymbol{TR}^{n}$, depicted by white color in the contour plot, reflect that of the superconducting gap. The cross-like marks in panel **b** depict the temperature dependence of the gap $2\Delta_{\pi}$, discussed in the Section 3.1, with the temperature axis scaled to have the T_c equal to 31 K. We can see a good agreement between the line, depicted by the cross-like symbols and the white-color feature in the normalized transmission on the plot. Therefore, the transmission ratio of the photoexcited superconductor, $\boldsymbol{TR}_{PE}$, can be directly compared with $\boldsymbol{TR}_{eq}$.

In the case of the THz excitation the excitation energy densities were small, and the transmission ratio of the photoexcited state is close to that in equilibrium, i.e., $\boldsymbol{TR}_{PE}(T, t_d, A) \approx \boldsymbol{TR}_{eq}(T)$. Therefore, the photoinduced change in the transmission ratio, i.e., $\Delta\boldsymbol{TR}_{PE} = \boldsymbol{TR}_{PE}(T, t_d, A) - \boldsymbol{TR}_{eq}(T)$, is a more representative quantity to study the photoinduced dynamics. In order to provide a basis for comparing the photoinduced changes, we show in the Fig. 4.2 **c** the difference between the equilibrium transmission ratio of the sample at specified temperatures and transmission at T = 4 K. $\Delta\boldsymbol{TR}_{eq} \equiv \boldsymbol{TR}(T) - \boldsymbol{TR}(4K)$ has a characteristic zero-crossing point at $\nu \approx$1.2 THz at low temperature, shifting towards low frequencies with increasing the temperature. Above this frequency a broad negative peak is observed, below 1 THz $\Delta\boldsymbol{TR}_{eq}$ has a broad positive maximum. The ratio $\Delta\boldsymbol{TR}_{eq}(1.8\text{ THz})/\Delta\boldsymbol{TR}_{eq}(0.4\text{ THz}) \approx 5$. Therefore, the maximum photoinduced changes in the transmission ratio are expected to appear at low frequency of $\approx$ 0.4 THz, where $\Delta\boldsymbol{TR}$ should be positive, and at higher frequency of $\approx$ 1.8 THz, where $\Delta\boldsymbol{TR}$ should be negative.

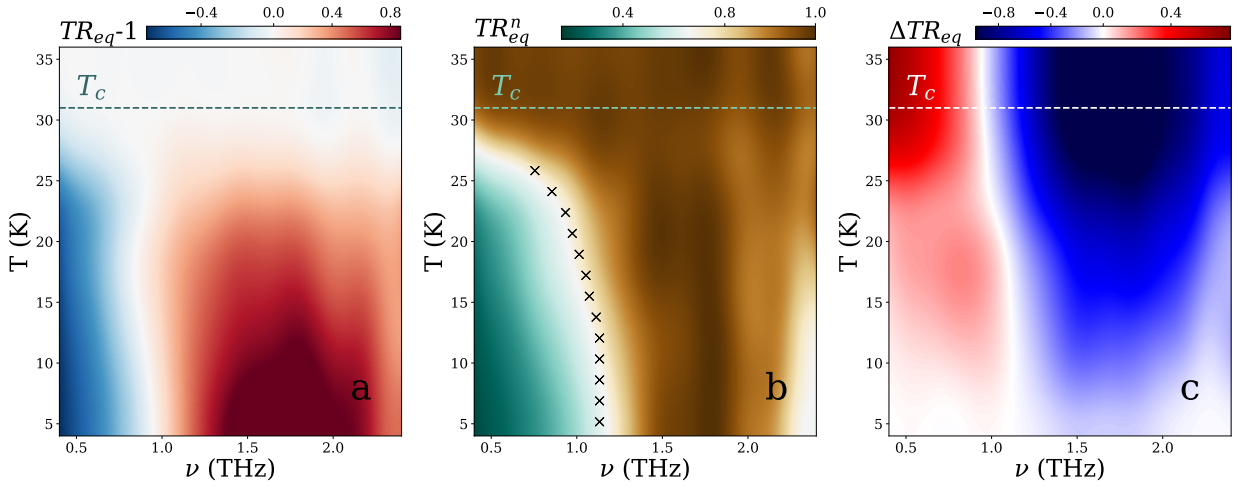

Figure 4.2: Equilibrium transmission ratio of MgB_2 as a function of T in various normalizations. **a** $\boldsymbol{TR}_{eq} - 1$; **b** $\boldsymbol{TR}^n_{eq}$. Here, a spectral feature, that has a temperature dependence of the gap, can be distinguished. Cross-like marks depict the temperature dependence of the gap $2\Delta_\pi$, scaled for T_c of 31 K. **c** $\Delta\boldsymbol{TR}_{eq} \equiv TR_{eq}(T) - TR_{eq}(4K)$, providing a basis for comparison of the small photoinduced changes $\Delta\boldsymbol{TR}_{PE}$.

4.3 PHOTOINDUCED DYNAMICS OF THE TRANSMISSION AND THE OPTICAL CONDUCTIVITY OF MGB_2

In the narrow-band THz_{FEL} pump – broadband THz probe spectrally-resolved experiment the data were recorded at 5 different temperatures from 5 K to 24 K, at 2–3 pump absorbed energy densities and at 2–3 PP time delays t_d. Each transient was repeated 2–6 times (depending on S/NR) and averaged. In the experiment we used ν_{FEL}= 2.7 THz for excitation. In the other experimental runs we also tried with different ν_{FEL}, however, the data quality turned out to be substantially lower, likely due to the low FEL stability.

As already mentioned, the THz_{FEL} pump – broadband THz probe experiment is time-consuming, while the *beamtime* is strictly limited at the large-scale facility experiments. Due to this fact, we recorded spectrally-resolved changes in transmission for several values of t_d, while the pump-induced gap dynamics with high enough temporal resolution was obtained in the spectrally-integrated measurements (cyan line in Fig. 4.3a). The values of the t_d, for which the spectrally-resolved data were recorded, are depicted with red stars in Fig. 4.3a: at the rising edge of the photoinduced gap suppression (t_d = 2 ps), at the peak of the photoinduced gap suppression (t_d = 35 ps) and in the region where the superconducting state partially recovers (t_d = 135 ps).

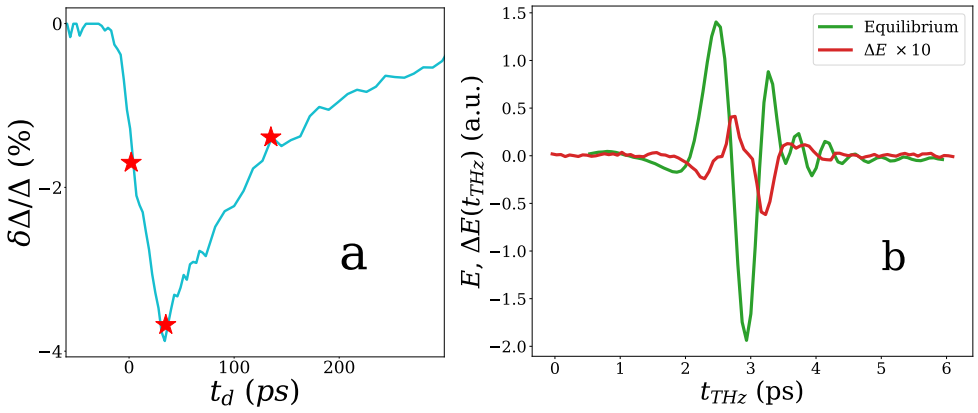

Figure 4.3: Obtaining the time- and spectrally-resolved changes in $\boldsymbol{TR}_{PE}$. **a** Cyan curve shows $\delta\Delta/\Delta$ as a function of t_d, obtained in the spectrally-integrated pump-probe experiment. Red stars indicate the t_d values, at which the spectrally-resolved transients were recorded for $T = 5$ K and $A = 3.4$ mJ/cm^3. **b** An example of the THz pump-induced changes (red) in the transmitted electric field of the THz probe, $\Delta E(t_{THz})$, compared to the equilibrium $E(t_{THz})$ (green) at T= 5K.

The data acquisition in the spectrally-resolved experiment (both with optical and with THz excitation) was performed utilizing the double lock-in detection, where the pump was mechanically modulated with the chopper, and the THz broadband probe signal was modulated by applying the pulsed bias voltage to the PCA emitter at the frequency, equal to half of the repetition rate of the femtosecond laser system, i.e., at ≈ 125 KHz.

Simultaneously, for each set of experimental parameters (T, A and t_d) the time-domain signals from the two lock-in channels were recorded. The first channel contained the combined signal $S_1 = E_{\text{unpumped}}(t_{THz}) + E_{\text{pumped}}(t_{THz}) \equiv E_0(t_{THz}) + \frac{\Delta E(t_{THz})}{2}$, where $E_0(t_{THz})$ was the unpumped $E(t_{THz})$ and $\Delta E(t_{THz})$ were the pumped-induced changes. This approximation is valid for small perturbation limit, satisfied in our case. The second channel contained solely pumped-induced changes $S_2 = \Delta E(t_{THz})$.

To obtain the photoinduced changes in transmission we start from the photoinduced changes in the transmitted THz electric field (Fig. 4.3b), $\Delta E(t_{THz}, t_d, T, A)$. The change in the transmission, normalized to the transmission of the normal state (T≥T_c), is extracted as $\Delta\boldsymbol{TR}_{PE}(\nu) \equiv \Delta\mathcal{T}(\nu)/\mathcal{T}_N(\nu) = \Delta\widetilde{E}^2(\nu)/\widetilde{E}^2(\nu, T_c)$, where $\Delta\widetilde{E}(\nu)$ is the fast Fourier transform (FFT) of $\Delta E(t_{THz})$.

Fig. 4.4 demonstrates the photoinduced changes in the transmission, normalized to the transmission in the normal state, $\Delta\boldsymbol{TR}_{PE}(\nu)$, for the base temperature T = 5 K at the fixed t_d,

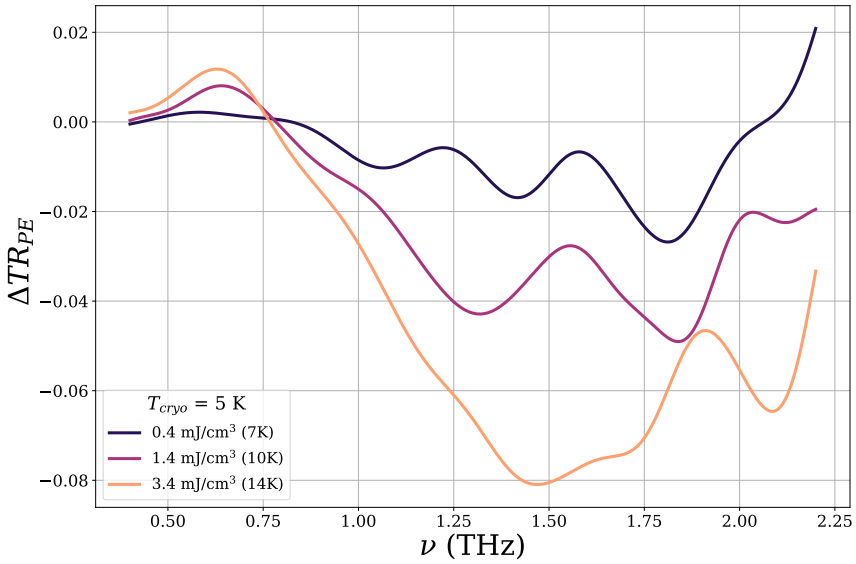

Figure 4.4: Spectrally-resolved photoinduced changes in the transmission ratio, $\Delta \boldsymbol{TR}_{PE}(\nu)$, driven by excitation with narrow-band THz pulses at different A. The temperature of the cryostat cold finger was set to 5 K, and the actual temperature of the sample (with the continuous heating taken into account) is denoted next to every value of A in the brackets. The spectral oscillations at high frequencies are caused by the low S/NR of the experiment.

corresponding to the peak of pump-probe signal, i.e., maximum gap suppression, for different absorbed energy densities of excitation. One can see, that the spectrally-resolved behavior is similar to the thermally-induced changes, $\Delta \boldsymbol{TR}_{eq}$, represented in Fig. 4.2**c**. The oscillations observed in all three curves in the frequency range from 1.2 THz to 2.2 THz should not be considered as spectral features and represent low S/NR.

For comparison, we present in Fig. 4.5 the transmission ratio of the photoexcited state, $\boldsymbol{TR}_{PE}$, driven by the optical excitation at the base temperature T = 4.6 K. The dynamic range of the OPTP is substantially better compared to THz pump-probe experiment (optical pump and THz probe pulses are perfectly synchronized), which allowed us to record the experimental data in the range of absorbed energy densities varied by a factor of ≈ 20. The dataset of optically-induced $\boldsymbol{TR}^{n}_{PE}$, shown in Fig. 4.5, is based on 5 values of the absorbed energy densities, with t_d fixed at 35 ps, corresponding to the peak of the pump-probe signal.

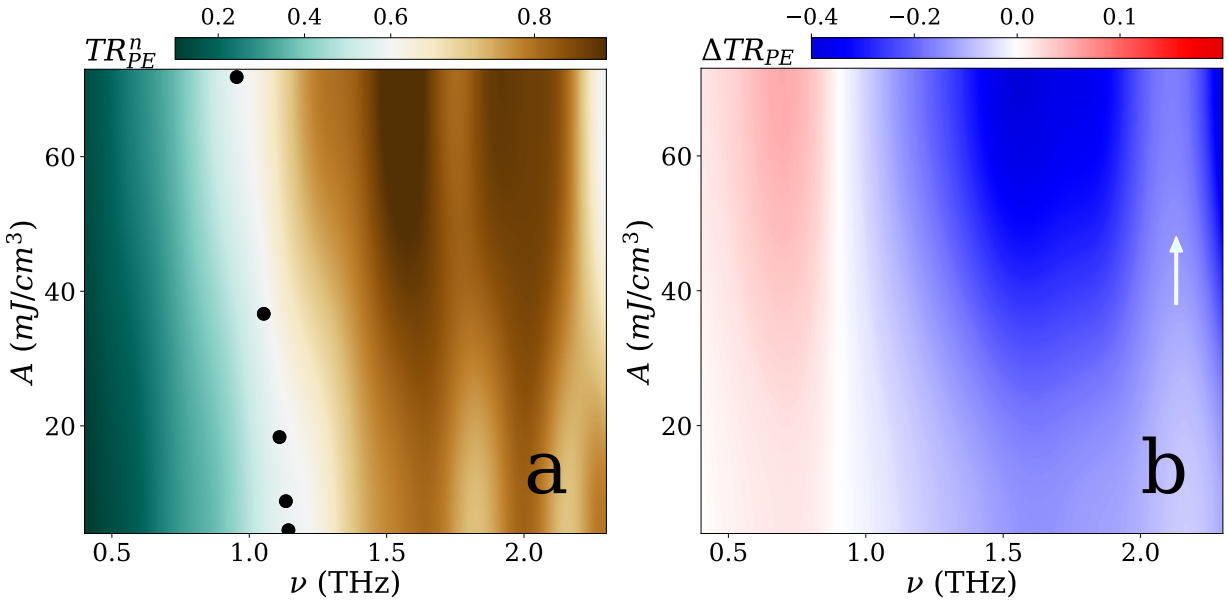

Figure 4.5: Optically-driven spectrally-resolved dynamics of the $\boldsymbol{TR}_{PE}$ in different normalizations as a function of A at the peak of PP signal. The base temperature equals 4.6 K. **a** $\boldsymbol{TR}^n_{PE}(\nu)$. Black circles depict the value of the gap, extracted in the spectrally-integrated OPTP experiment for similar T and A at the peak of pump-probe signal. **b** $\Delta\boldsymbol{TR}_{PE}(\nu)$. A spectral feature at $\nu \approx$ 2.1 THz could be attributed to the Δ_σ, that is not observed in the linear spectroscopy.

Panel **a** shows the transmission ratio of the photoexcited state, $\boldsymbol{TR}_{PE}$, normalized to the peak value at each A, i.e., $\boldsymbol{TR}^n_{PE}(\nu)$. One can see, that the spectrally-resolved behavior is similar to the equilibrium $\boldsymbol{TR}^n_{eq}$, implying that the T*-model used in our analysis is a valid approximation to describe the photoinduced gap dynamics. The black circles depict the value of the gap upon photoexcitation, extracted in the spectrally-integrated OPTP experiment for similar T and A at the peak of pump-probe signal. We can see that the spectral feature shown with white color (similar to that in $\boldsymbol{TR}^n_{eq}$, Fig. 4.2**b**) follows the A-dependence of the gap reduction. The oscillation-like spectral features, apparently, arise from the dividing of the transmission in the photoexcited state, $\mathcal{T}_{PE} = \Delta\mathcal{T}_{PE} + \mathcal{T}_{eq}$, by the transmission in the normal state, $\mathcal{T}_N$. It should be noted, that $\Delta\mathcal{T}_{PE}$ and $\mathcal{T}_{eq}$ is obtained in a single measurement, and no correction for the temperature drift between $\Delta\mathcal{T}_{PE}$ and $\mathcal{T}_{eq}$ is required. However, $\mathcal{T}_N$ is recorded prior to the pump-probe experiment, and therefore, may have slightly different spectral shape as if it were acquired along with the pump-probe data.

Fig. 4.5**b** shows $\boldsymbol{TR}_{PE}$ after subtracting the equilibrium $\boldsymbol{TR}_{eq}$ at each A, i.e., $\Delta\boldsymbol{TR}_{PE}(\nu)$. In general, spectrally-resolved $\Delta\boldsymbol{TR}_{PE}(\nu)$ is similar to $\Delta\boldsymbol{TR}_{eq}$, Fig. 4.2**c**. Remarkably, the optically-

induced $\Delta\boldsymbol{TR}_{PE}(\nu)$ shows a spectral feature at $\nu \approx 2.1$ THz, shown with an arrow in the plot. Here $\Delta\boldsymbol{TR}_{PE}(\nu)$ decreases (in the absolute value) to almost zero, consistently for all values of absorbed energy density.

It should be noted that at high frequencies the magnitude of the THz probe signal is low, and in the equilibrium spectroscopy the weak features on the edge of the frequency range are usually neglected as non-trustable. However, the pump-probe spectroscopy can emphasize weak spectral features due to the derivative-like modulation nature of the approach. We can see that the spectral oscillations in $\boldsymbol{TR}_{PE}$, seen in Fig. 4.5**a**, are efficiently cancelled out by subtracting the equilibrium $\boldsymbol{TR}_{eq}$. Therefore, the observed feature, present throughout the entire range of absorbed energy densities, displays a real spectral feature. Given the fact, that the frequency range of this spectral feature coincides with the range, where Δ_σ is observed in ARPES and STS measurements [29, 30], we can attribute the feature to the modulation of the superconducting gap in the σ-band, which is not observed in the equilibrium spectroscopy. Indeed, further experimental studies and theoretical analysis, including simulations of the temperature dependence of the optical conductivity for the case of two coupled order parameters, are required to investigate this observation.

In Figure 4.6, we present the A-dependence of the spectrally-resolved changes in the optical conductivity driven by the optical excitation at the peak of PP signal for two base temperatures 4.6 K and 20 K. The graph is based on the dataset, recorded at 5 values of the absorbed energy density in the range from 4 to 70 mJ/cm^3.

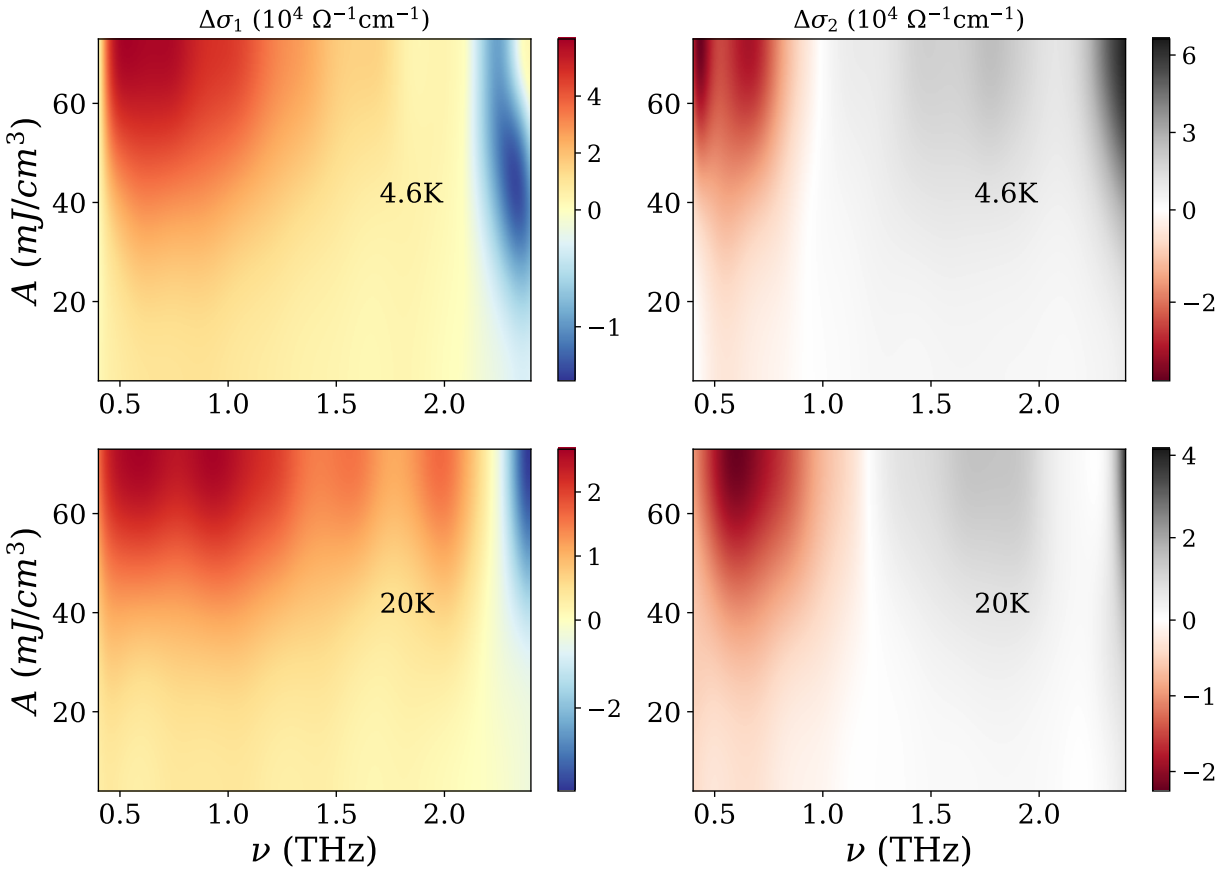

Figure 4.6: Optical pump-induced spectrally-resolved dynamics of the optical conductivity for different absorbed energy densities at the peak of PP signal for two base temperatures. Top panels represent $\Delta\sigma_1$ and $\Delta\sigma_2$ for base temperature 4.6 K, bottom panels – for 20 K. The red areas in both graphs indicate the photoinduced suppression of the gap. Photoinduced changes $\Delta\sigma$ are, in general, similar to an increase in temperature.

The prominent feature in $\Delta\sigma_1$ (represented by red color in the plot) is observed near the frequency of the superconducting gap $2\Delta_\pi$. $\Delta\sigma_2$ reaches maximum at low frequencies, characteristic for the suppression of the superconducting order. The photoinduced spectrally-resolved changes $\Delta\sigma$ are, in general, similar to thermally-induced $\Delta\sigma$, this fact confirms the validity of the T* model as an approximation to account for the pump-induced dynamics of superconducting state in the case of above-gap excitation.

The spectral feature around 2.1 THz, also observed in $\Delta\boldsymbol{TR}_{PE}(\nu)$ (Fig. 4.5 **b**), is visible for all absorbed energy densities around 2.1 THz. Here, the photoinduced change in σ_1 is close to zero for base temperature of 4.6 K in the entire range of absorbed energy densities, and at 20 K

$\Delta\sigma_1$ changes sign (from positive to negative).

As noted above, a modeling of the electrodynamic response of the two-gap superconductor, including the coupling between the two bands, is required to make a direct comparison of the observed changes in $\Delta\sigma(\omega)$ at high frequencies, to the photoinduced changes in Δ_σ.

PHOTOINDUCED SPECTRALLY-RESOLVED DYNAMICS OF MgB_2 DRIVEN BY THE THZ EXCITATION

In Fig. 4.7 we present the transmission ratio of the photoexcited state, $\boldsymbol{TR}_{PE}$, driven by the THz excitation as a function of ν and T for two values of absorbed energy density. Unfortunately, due to huge losses in the FEL beam path, the maximum absorbed energy density was only 3.6 mJ/cm^3, therefore we cannot track the systematic behaviour of $\boldsymbol{TR}_{PE}$ over a large range of excitations. The dataset of the photoinduced $\boldsymbol{TR}^n_{PE}$, shown in Fig. 4.7, is based on 5 values of T, with t_d fixed at 35 ps, corresponding to the peak of the pump-probe signal.

Given that in the low excitation limit $\boldsymbol{TR}_{PE} \approx \boldsymbol{TR}_{eq}$, we present the photoinduced changes in the transmission ratio, $\Delta\boldsymbol{TR}_{PE}$. One can see, that the spectrally-resolved behavior is similar to the equilibrium $\boldsymbol{TR}^n_{eq}$ and to the $\Delta\boldsymbol{TR}_{PE}$ driven by the optical excitation. The oscillation-like spectral features, apparently, arise from the dividing of the transmission in the photoexcited state, $\mathcal{T}_N$, and should not be considered.

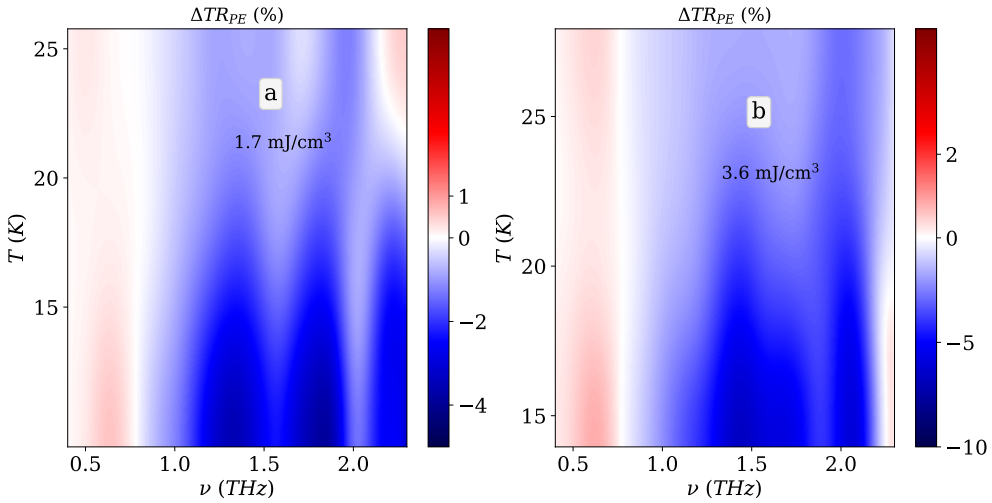

Figure 4.7: Temperature dependent $\Delta\boldsymbol{TR}_{PE}(\nu)$ for the case of THz excitation, at the peak of PP signal. Panels **a** and **b** represent $\Delta\boldsymbol{TR}_{PE}(\nu)$ at 1.7 and 3.6 mJ/cm^3, respectively.

As we discussed, due to absence of the theoretical model to describe the optical conductivity of MgB_2, the proper quantitative analysis of the equilibrium optical conductivity is not possible. Therefore, understanding of the photoinduced changes can be made only on a qualitative level.

Figure 4.8 presents the temperature dependence of the spectrally-resolved photoinduced changes in optical conductivity for the case of FEL excitation. The time delay, t_d, is fixed at the value, corresponding to the peak of PP signal. The pseudo-color plots are based on the datasets recorded at 5 values of the base temperature and shown for two absorbed energy densities. Grey dash-dot lines represent the temperatures at which the photoinduced changes in transmission were recorded, with the continuous heating effect taken into account. The value of absorbed energy density is given on each plot.

We can see that the maximum photoinduced change in σ_1 is observed at the frequency around $2\Delta_\pi$, and the absolute maximum in $\Delta\sigma_2$ occurs in the low-frequency range, fully consistent with suppression of the superconducting order. $\Delta\sigma_2$ changes sign (from negative to positive) at $\nu \approx 1$ THz. Unfortunately, due to huge losses in the FEL beam path, the maximum absorbed energy density was only 3.6 mJ/cm^3, therefore we cannot track the systematic behaviour of $\Delta\sigma(\nu)$ over a large range of excitations. Again, the spectral oscillations seen in the $\Delta\sigma(\nu)$ should not be considered as spectral features, being a consequence of low S/NR of the experiment.

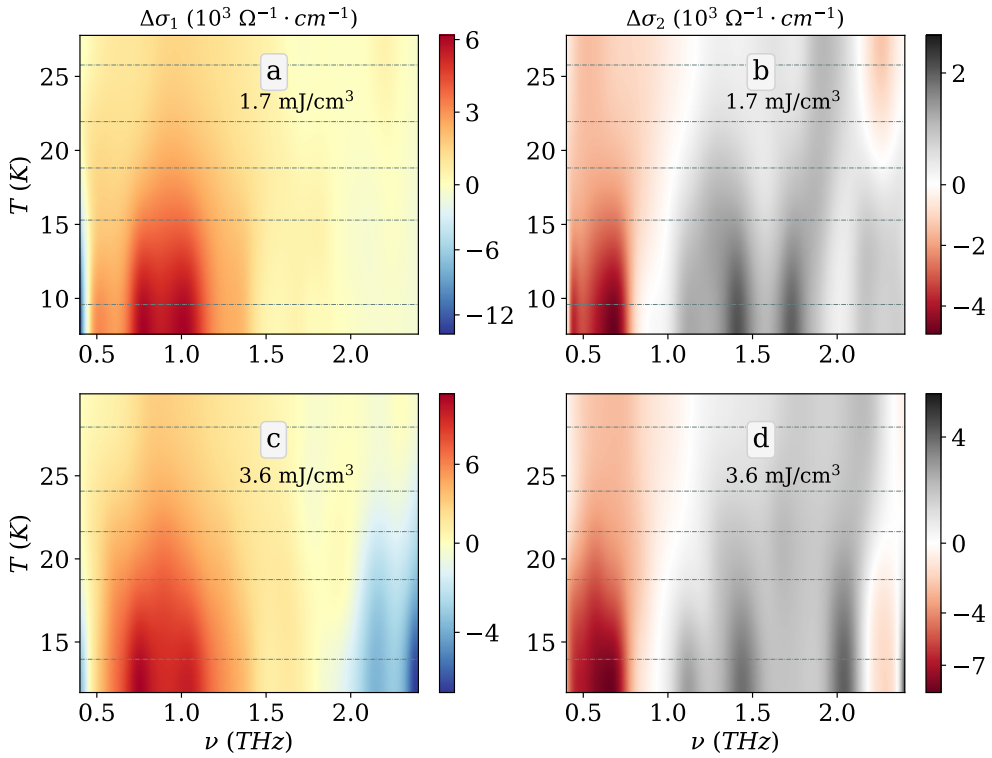

Figure 4.8: Temperature dependent spectrally-resolved changes in the complex conductivity at the peak of PP signal. Panels **a** and **c** represent $\Delta\sigma_1(\nu)$ at 1.7 and 3.6 mJ/cm^3, **b** and **d** represent $\Delta\sigma_2(\nu)$ for these absorbed energy densities. The dashed horizontal lines present the temperatures, where the data were recorded.

4.4 SUMMARY

In this Chapter we present experimental results on spectrally-resolved transmission dynamics of MgB_2 upon resonant THz and off-resonant NIR ultrafast excitation. Based on the spectrally-resolved photoinduced dynamics, we show that the T*-model that we use to evaluate the dynamics of the superconducting gap driven by the photoexcitation, is a valid approximation, and in general, the electronic system of a superconductor upon photoexcitation can be characterized by the effective temperature T*.

We show that the pump-probe THz spectroscopy is more sensitive to detection the spectral features than the linear spectroscopy. In the experiment with optical (NIR) excitation a sharp high-frequency feature is observed, that could be associated with modulation of the superconducting gap in the σ-band.

As one can see, discussion and understanding of the obtained results is still in progress, and

we are in the discussion with the theoretical groups. The interpretation of the non-equilibrium spectrally-resolved dynamics of the superconducting state, on one hand requires better understanding of the ground state of the multi-band superconductor while on the other hand can help to achieve this understanding.

CHAPTER 5

CONCLUSIONS

In this thesis, we present the time-resolved experimental studies of the dynamics in the two-band superconductor MgB_2, driven by photoexcitation, using pump-probe THz spectroscopy.

Our systematic studies of the energy gap dynamics in a two-band superconductor MgB_2 allowed us to obtain temperature- and absorbed energy density-dependencies of the main parameters for perturbed superconducting state following pulsed photoexcitation. From the time-resolved gap dynamics we extracted the pair-breaking dynamics, characterizing the quenching of the superconducting order, the recovery time of the superconducting state and the gap suppression, represented by the peak value of the photoinduced change in optical conductivity.

The recovery dynamics of the superconducting state is well accounted by the phenomenological Rothwarf-Taylor model, assuming the "phonon bottleneck", with recovery time decreasing with increasing of both temperature, T, and the absorbed energy density, A. The A–dependence of the maximum gap suppression shows a sub-linear behavior, which is also consistent with the Rothwarf and Taylor model, where the photoexcited state is characterized by T^* (common temperature of the condensate, quasiparticles and high-frequency phononss).

The most fascinating result of our study is the non-trivial behavior of the photoexcited gap suppression. When exciting with narrow-band THz pulses, we observe a decrease in the pair-breaking efficiency with increasing T, displaying a minimum around $0.6T_c$. This observation is at odds with the expected monotonous increase, following the reduction of the condensation energy with increasing the temperature. We attribute this observation to a process competing with breaking of Cooper pairs which can be treated as a transient enhancement of supercon-

ductivity. The observed enhancement effects that follow from the reducing of the pair-breaking efficiency by a factor of ≈2 are much more pronounced than in the early studies of enhancement of superconductivity by continuous microwave irradiation. There, the observed increase in T_c was on the order of a few percents. Thus, tuning the excitation to below the small gap ($2\Delta_\pi$) one may be able to globally enhance superconductivity by a considerable amount.

For comparison, we show the results on off-resonant excitation with NIR laser pulses where the temperature dependence of the pair-breaking efficiency follows the thermal reduction of the gap. We show that the dynamics of the superconducting state following optical excitation is similar to that, in the case of the THz excitation. However, the rise-time of the optically driven pair-breaking process is substantially faster, which can be attributed to the difference in pair-breaking rates by high-frequency optical phonons (in the case of optical excitation) and low-frequency acoustic phonon modes (in the case of THz excitation).

We further present experimental study of time evolution of the spectrally-resolved electrodynamic properties of MgB_2, such as transmission in the superconducting state and the optical conductivity, upon excitation with off-resonant NIR and resonant THz excitation. For the first time, the time- and spectrally-resolved optical conductivity of MgB_2 is studied using THz spectroscopy with narrow-band THz excitation. We show that the pump-probe THz spectroscopy may be used to detect weak spectral features, that may not be resolved using the linear spectroscopy.

In the experiment with optical (NIR) excitation a sharp high-frequency feature is observed in the optical conductivity, that could be associated with modulation of the superconducting gap in the σ-band. Interpretation of both equilibrium and non-equilibrium experimental data is, however, not straightforward and requires, among other, a better understanding of the ground state of the two-band superconductor MgB_2. Additional systematic experiments with better signal-to-noise ratio could provide more information to build the complete picture of the complicated processes occurring on the ultrafast timescale in the perturbed multi-band superconductor.

To further investigate the phenomenon of enhancement of superconductivity, an experimental systematic study, utilizing narrow-band sub-gap THz excitation and broadband THz spectrally-resolved probing, would enable access to the observation of the redistribution of the thermally-induced quasiparticles which are likely responsible for the observed enhancement effects. The systematic studies with tuning the photon energy of the excitation, temperature and excitation density would provide better understanding of this effect, both on the qualitative and the quantitative level.

We demonstrate, that the time-resolved THz spectroscopy is a powerful experimental technique, being especially suitable for studying the electrodynamics of superconductors, manifested in the superconducting gap and the optical conductivity, and its time evolution following excitation. Investigation of the material properties in out-of-equilibrium provides additional degrees of freedom, such as timescale, excitation energy density, temperature, frequency or the type of excitation. And even though the world will never show us all of its mysteries, the time-resolved THz spectroscopy can shed light on some of the intriguing phenomena.

APPENDIX A

ALIGNMENT OF THE THZ BEAM PATH

Being a powerful and unique tool for investigating low-energy in solids, THz radiation is also challenging in many senses. As shown in Chapter 2, generating and detecting electromagnetic radiation in the THz range requires a lot of effort in contrast to, for example, visible range of light (including IR and UV) where we have bulb lamps or LEDs as sources and photodiodes for detection.

These "fundamental" constraints result also in difficulties with handling the THz radiation, in our case alignment the THz beam in the experimental setup. Additionally, there are a few aspects making the alignment even more tedious:

i) usually, the power of the THz beam used in the setup is quite low, which means often there are no means to compensate losses by simply increasing the power. Thus, any type of beam clipping must be avoided;

ii) the sensitivity of the THzTDS scales with the electric field of the THz beam, which is inversely proportional to the diameter of the THz beam. This implies that the THz beam must be focused to as small as possible spot. However, given the wavelength of the THz radiation is in range of 300 μm, achieving tight focusing requires working with large beam diameters, where

$$\varnothing_f \propto \frac{\lambda F}{D}. \tag{A.1}$$

Here $\varnothing_f$ is the beam diameter at the focus, λ is the wavelength, F is the focal length and D is the diameter of the beam incident on the focusing element. Thus, to achieve small diameter of the beam at the focus, the D/F ratio should be large;

iii) given the previous aspect and considering that aberrations scale as $\left(\frac{D}{F}\right)^2$, the alignment accuracy is crucial.

For guiding and focusing the THz beam the OAPMs are usually used, by default being free of spherical aberration. However, the fully aberration-free operation is possible only in case of perfect alignment of all five degrees of freedom (Fig. A.1): 2 angles in xz and yz planes, displacement along x and y directions and the rotation about the z axis. Additionally, adjustment of the focal point might be required that is performed by moving along z direction.

In the case of THz generation other than by using the laser radiation, a special camera is needed for observing the THz beam alignment, as it was done in the experiment described in the Section 2.2.3. Afterwards, an alignment laser, in the visible range, can be added in the setup to simplify the alignment.

If the THz radiation is born in the process of nonlinear conversion of the femtosecond laser pulses, the excitation laser beam can serve as an alignment laser. The THz emitter can be assumed as a plane-parallel thin plate, therefore, the wavefront of the emitted THz beam should match the one of the excitation laser beam. In the experimental setup described in the Section 2.1 this feature was used, and the four OAPMs were aligned by the laser beam.

For consistent alignment of all five degrees of freedom a set of reference 5-hole apertures was designed (Fig. A.2**a**). The aperture **M** is inserted in the diverging excitation beam to a designed position and creates a specific pattern in the laser beam. The aperture **C** is consequently inserted into the optical path after each of the OAPM and serves for control of the beam size and direction and the aberration pattern. The astigmatism-like and comma-like aberrations can be distinguished, providing a hint of which of the degrees of freedom requires adjusting. In the bottom panels of Fig. A.2 the photos of the beam patterns are represented. Panel **(b)** shows how the beam looks like right after the aperture **M**. Panel **(c)** represents the beam reflected off the misaligned OAPM, where horizontal elongation of the pattern suggests the astigmatism introduced by angular misalignment in the xz plane.

The optical beam path was designed in the planar layout (Fig. 2.1) with the reference pinholes in and aligned according to the design. After finding the "time-zero" – temporal matching of the "excitation" and "sampling" pulses – the THz signal is obtained immediately, and no major spatial alignments was required, speaking in favor of efficiency of the suggested alignment method.

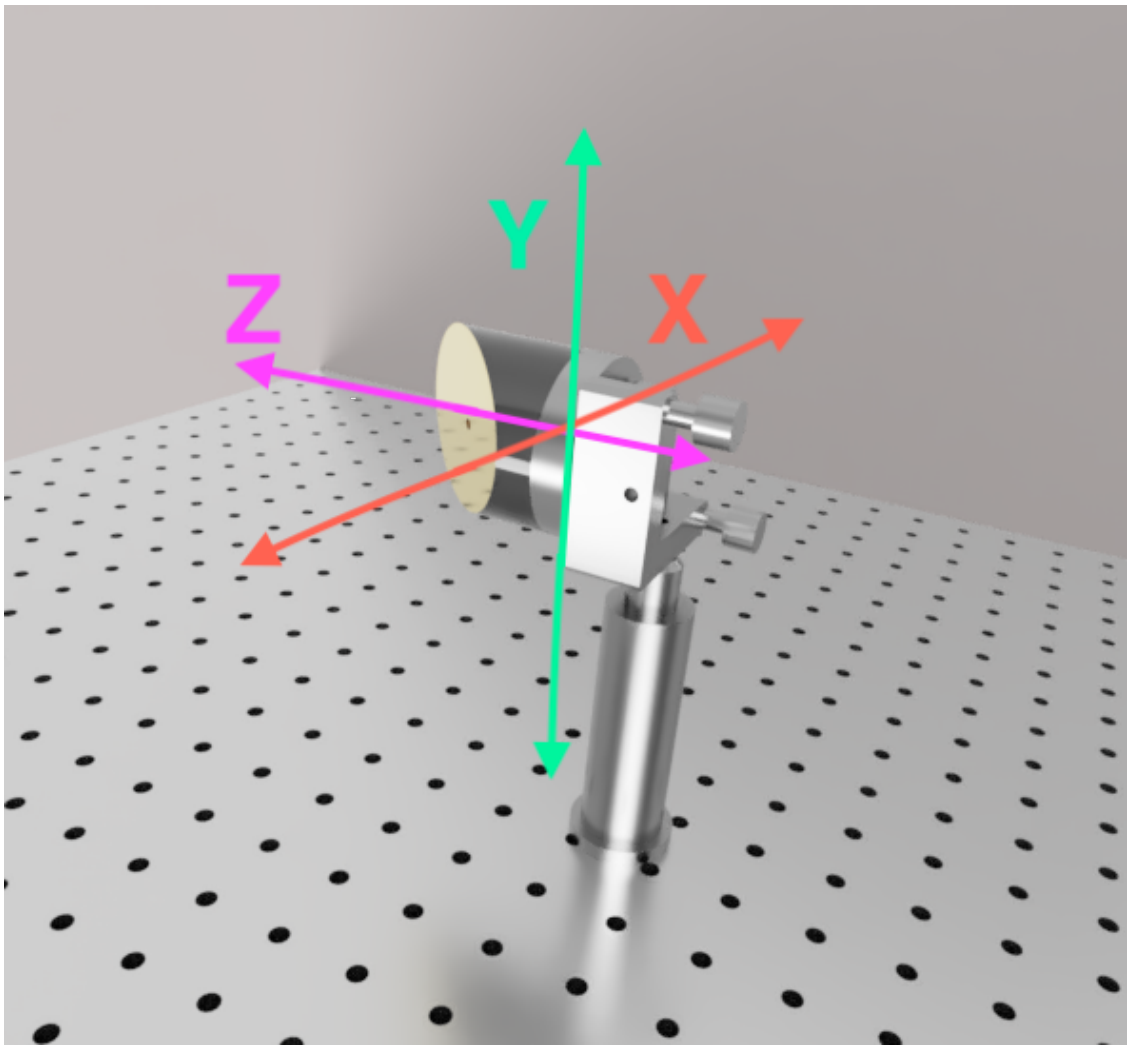

Figure A.1: Axes of alignment of the OAPM

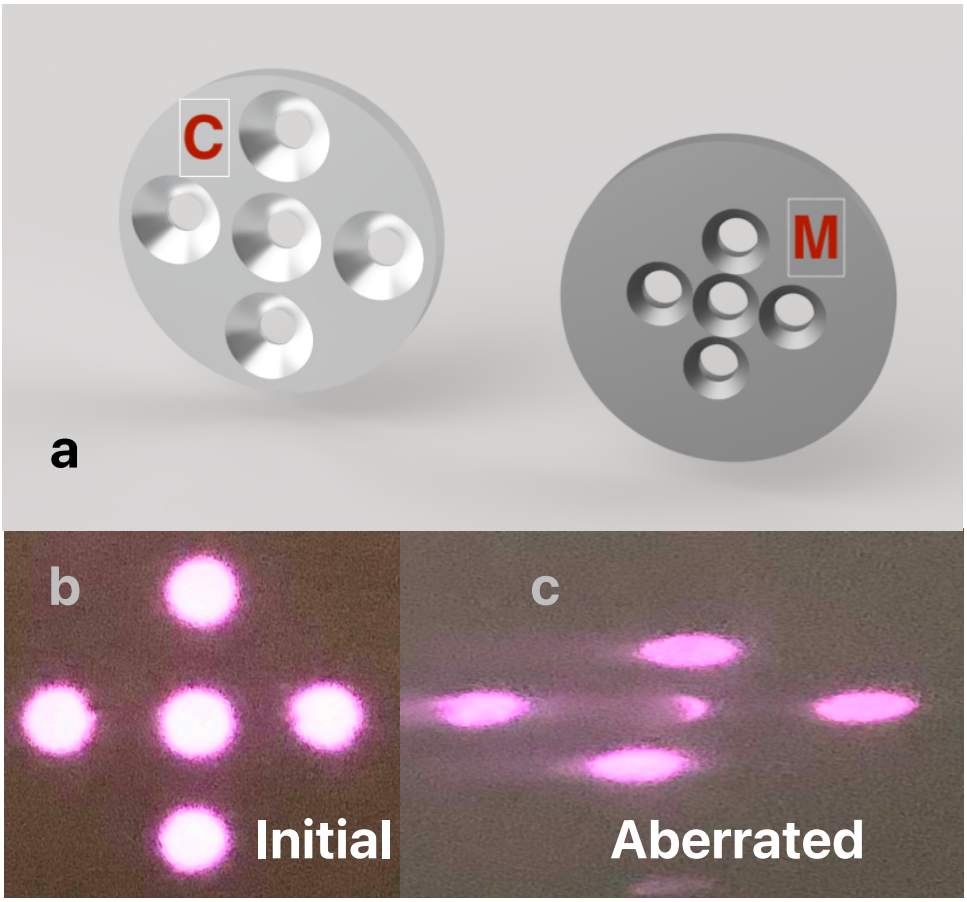

Figure A.2: **a** Designed 5-hole apertures, **b** initial beam pattern, **c** aberrated beam. The alignment of the layout is optimum if the beam pattern, formed by the 5-hole aperture **M** (panel **b**), remains unchanged after passing the OAPMs. The pattern on the panel **c**, as an example of the uncompensated aberrations, indicates an astigmatism in the horizontal direction.

APPENDIX B

CALCULATING THE ABSORBED ENERGY DENSITY IN THE THIN FILM AND ACCOUNTING FOR THE CONTINUOUS HEATING EFFECT

B.1 ABSORBED ENERGY DENSITY EVALUATION

The value of the absorbed energy density A (in mJ/cm^3) within the MgB_2 thin film allows one to compare the amplitude of the excitation induced gap suppression with the superconducting condensation energy or the energy required to heat up the sample to T_c. In the low perturbation limit, the amplitude of the relative photoinduced gap suppression, $\frac{\delta\Delta}{\Delta}$, normalized to the absorbed energy density A, is expected to be equal to reciprocal value of the condensation energy $1/E_{cond}$. The absorbed energy density was calculated using the following equation:

$$A = \frac{P_{inc}}{f_{FEL}} \cdot \frac{Abs \cdot Tr_{window}}{\frac{\pi \cdot \varnothing^2}{4} \cdot d_{MgB_2}}, \tag{B.1}$$

where P_{inc} is the incident power of the THz beam, measured at the sample position, f_{FEL} is the repetition rate of the FEL pulses (13 MHz), Abs is the absorbed fraction of the THz pulse energy calculated from the optical conductivity of the thin film, Tr_{window} is the transmission of the front cryostat window with the Fabry-Perot effect, taken into account, $\varnothing$ is the pump beam diameter at the focus (FWHM) and d_{MgB_2} is the film thickness (30 nm). Absorption Abs of the pump pulse in the MgB_2 film is calculated using the transfer-matrix method (TMM) [93]

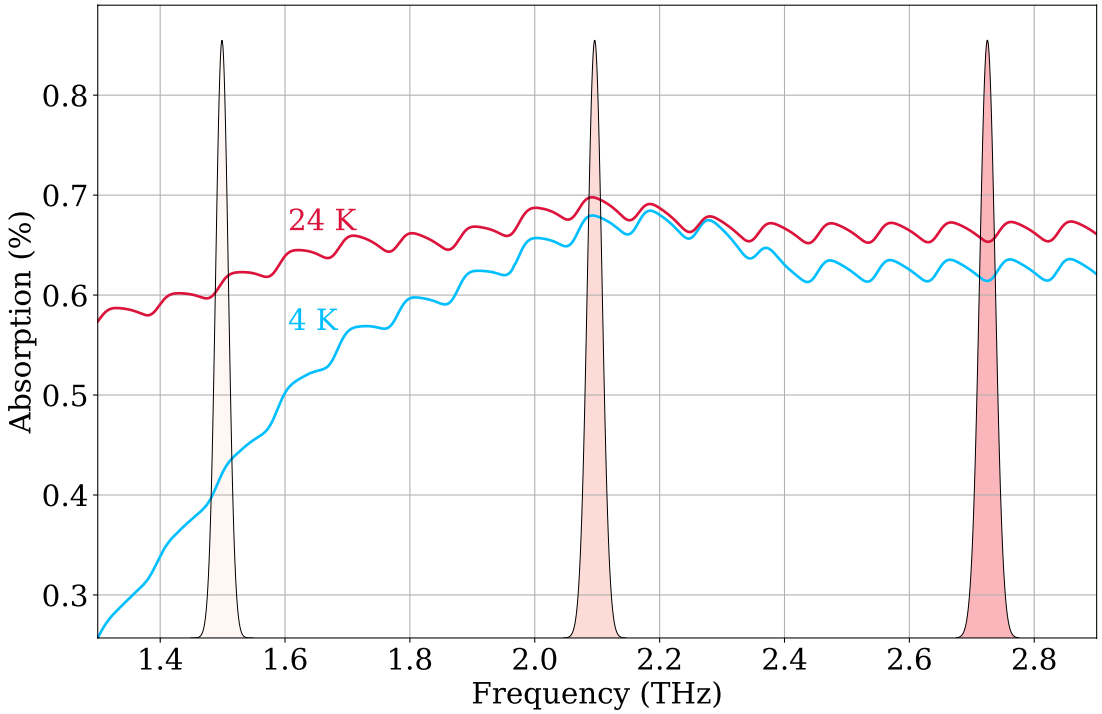

Figure B.1: Frequency dependence of the absorption, integrated over the THz pulse bandwidth, at 4 K and 24 K. Spectra of the THz pulses at different frequencies used in the experiment are represented by three Gaussians

to account for the Fabry-Perot effect in the sample. In general, this effect, caused by multiple reflections inside the substrate, can lead to a strong variation of the absorbed energy density depending on substrate thickness, temperature, frequency and optical conductivity of the thin film (which is also temperature and frequency dependent). However, the finite spectral width of the THz pulses smears this effect. The calculation showed that the frequency dependence of absorption integrated over the THz pulse bandwidth (Fig. B.1) is modulated very weakly ($\approx$ 5%).

Although the relative error in calculating the absorbed energy density within the set of parameters for a given frequency is low, the error in the absolute value of absorbed energy density with all the uncertainties taken into account can be substantial. E.g., to evaluate the THz beam profile and the overlap between the pump and the probe beams, the pyroelectric camera was used, where the pixel size is as large as ~1/10 of the beam diameter.

B.2 CONTINUOUS HEATING EFFECT

Absorption of the THz radiation with high average output power up of to 1 W (focused on a spot of $\approx$1 mm^2) results in temperature difference between the probed thin film area and the cryostat cold finger. In turn, this temperature difference can cause systematic errors in calculating the photoinduced changes of the superconducting gap.

In the preliminary experiments to the measurement session with broadband THz probe, the noticeable continuous heating effect was observed by inspecting the changes in transmission of the probe signal at negative pump-probe time delay (probe before pump). Initially, this observation seemed inconsistent, given that the calculated temperature gradient in the MgO substrate does not exceed 0.1 K.

However, we found out that thermal boundary resistance can play a decisive a role in case of a thin film deposited on a substrate. According to [94, 95] the inverse thermal boundary resistance (TBR) is linearly proportional to the temperature in the low-temperature limit. Thus, the following formula was derived to account for continuous heating effect:

$$T_{act} = \sqrt{T_{base}^2 + \kappa \cdot P_d}, \tag{B.2}$$

where T_{act} is the actual (elevated) temperature of the thin film, T_{base} is the base temperature (cryostat cold finger temperature), P_d is the absorbed continuous pump power density and κ is the parameter related to the TBR – proportional to a temperature derivative of the thermal boundary conductivity.

We performed systematic measurements to quantify the continuous heating and experimentally determined the parameter κ to be equal to 3.8 $\frac{\mathrm{K^2 \cdot cm^2}}{\mathrm{mW}}$. To do that, we used transmission of the probe in the superconducting state as a consistent measure for the actual sample temperature. We note, however, that the TBR can vary from sample to sample.

For the NbTHzPP experiment, described in Chapter 3, we have the upper limit for the heating effect: at T_{base} = 35 K and P_d = 350 mW/cm^2 a distinct pump-probe signal is observed which means that temperature difference does not exceed 1 K (given the $\mathrm{T_c}$ = 36 K). This implies that the parameter κ for the sample, investigated in the NbTHzPP experiment, does not exceed 0.1 $\frac{\mathrm{K^2 \cdot cm^2}}{\mathrm{mW}}$ – a factor of 40 smaller than in the sample, studied in the OPTP and TPTP experiments. Since we have no means for more accurate estimates, the heating effect in the NbTHzPP experiment is considered with the value of κ = 0.1 $\frac{\mathrm{K^2 \cdot cm^2}}{\mathrm{mW}}$. Figure B.2 represents the dependence of the actual temperature of the sample T_{sample} on the absorbed energy density, AED, at 4 K and 20 K base temperature.

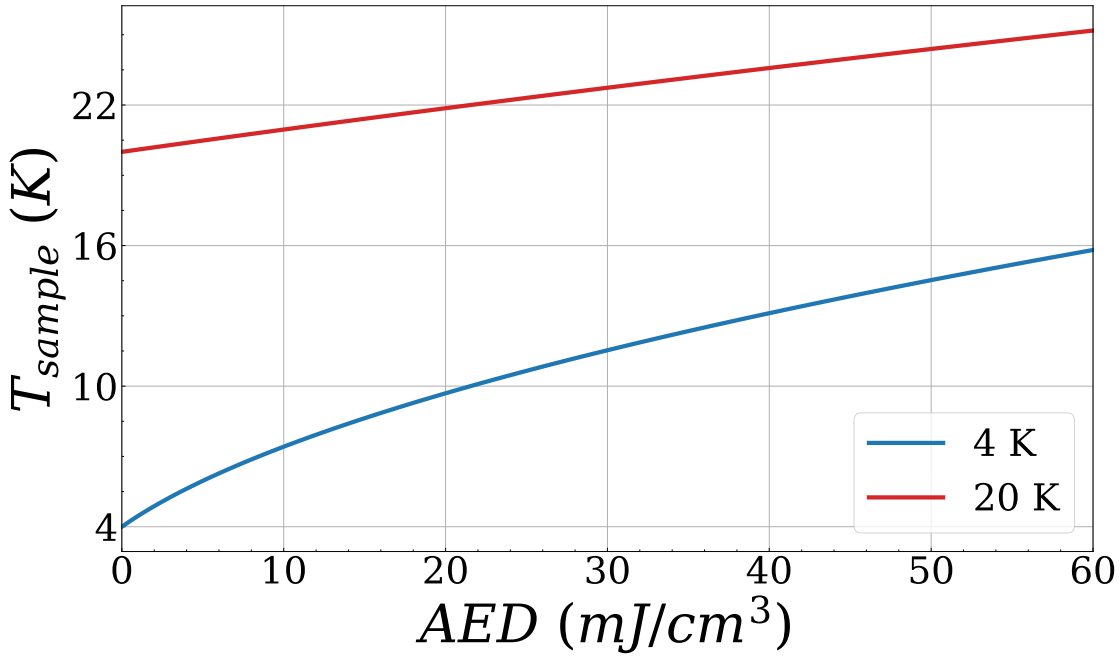

Figure B.2: AED dependence of the actual temperature of the sample at 4 K and 20 K base temperature.

APPENDIX C

AUTHOR CONTRIBUTIONS

Removed in the electronic version of this thesis due to data protection regulations.
In der elektronischen Version entfernt aufgrund datenschutzrechtlicher Bestimmungen.

BIBLIOGRAPHY

[1] R. Jaklevic, J. Lambe, A. Silver, and J. Mercereau, "Quantum interference effects in Josephson tunneling," *Physical Review Letters*, vol. 12, no. 7, p. 159, 1964.

[2] R. Glover III and M. Tinkham, "Transmission of superconducting films at millimeter-microwave and far infrared frequencies," *Physical Review*, vol. 104, no. 3, p. 844, 1956.

[3] J. Bardeen, L. N. Cooper, and J. R. Schrieffer, "Theory of superconductivity," *Physical review*, vol. 108, no. 5, p. 1175, 1957.

[4] M. Tinkham, *Introduction to superconductivity*. Mac-Graw-Hill Inc., 1996.

[5] J. Demsar, "Non-equilibrium phenomena in superconductors probed by femtosecond time-domain spectroscopy," *Journal of Low Temperature Physics*, vol. 201, no. 5, pp. 676–709, 2020.

[6] G. M. ELIASHBERG, "Rf field stimulated superconductivity of thin films [sverhprovodimist plenok, stimulirovannaya vch polem]," *Pisma v ZhETF*, vol. 11, pp. 186–188, 1970.

[7] C. Castaneda, *The Teachings of Don Juan: A Yaqui Way of Knowledge*. University of California Press, 1998.

[8] C. Chu, "Superconductivity above 90 K," 1987.

[9] A. Drozdov, P. Kong, V. Minkov, S. Besedin, M. Kuzovnikov, S. Mozaffari, L. Balicas, F. Balakirev, D. Graf, V. Prakapenka, *et al.*, "Superconductivity at 250 K in lanthanum hydride under high pressures," *Nature*, vol. 569, no. 7757, pp. 528–531, 2019.

[10] E. Snider, N. Dasenbrock-Gammon, R. McBride, M. Debessai, H. Vindana, K. Vencatasamy, K. V. Lawler, A. Salamat, and R. P. Dias, "Retracted article: Room-temperature superconductivity in a carbonaceous sulfur hydride," *Nature*, vol. 586, no. 7829, pp. 373–377, 2020.

[11] L. Wittgenstein, *On Certainty*. Basil Blackwell, 1st ed., 1969.

[12] M. Zelikman, *The fundamentals of the physics of superconductors*

Osnovy fiziki sverhprovodnikov

. Saint-Petersburg Polytechnical University, 2015.

[13] H. K. Onnes, "Investigations into the properties of substances at low temperatures, which have led, amongst other things, to the preparation of liquid helium," *Nobel lecture*, vol. 4, pp. 306–336, 1913.

[14] H. Kamerlingh Onnes, "Further experiments with liquid helium. d. on the change of electrical resistance of pure metals at very low temperatures, etc. v. the disappearance of the resistance of mercury," *Koninklijke Nederlandse Akademie van Wetenschappen Proceedings Series B Physical Sciences*, vol. 14, pp. 113–115, 1911.

[15] L. N. Cooper, "Bound electron pairs in a degenerate fermi gas," *Physical Review*, vol. 104, no. 4, p. 1189, 1956.

[16] F. London and H. London, "The electromagnetic equations of superconductor," vol. A149, March 1935.

[17] L. Landau, "The theory of phase transitions," *Nature*, vol. 138, no. 3498, pp. 840–841, 1936.

[18] M. Dressel and G. Grüner, *Electrodynamics of Solids: Optical Properties of Electrons in Matter*. Cambridge: Cambridge University Press, 2002.

[19] D. C. Mattis and J. Bardeen, "Theory of the anomalous skin effect in normal and superconducting metals," *Physical Review*, vol. 111, no. 2, p. 412, 1958.

[20] W. Zimmermann, E. Brandt, M. Bauer, E. Seider, and L. Genzel, "Optical conductivity of BCS superconductors with arbitrary purity," *Physica C: Superconductivity*, vol. 183, no. 1-3, pp. 99–104, 1991.

[21] M. M. Korshunov, Y. N. Togushova, and O. V. Dolgov, "Impurities in multiband superconductors," *Physics-Uspekhi*, vol. 59, no. 12, p. 1211, 2016.

[22] H.-S. Xu, Y.-J. Yan, R. Yin, W. Xia, S. Fang, Z. Chen, Y. Li, W. Yang, Y. Guo, and D.-L. Feng, "Multiband superconductivity with sign-preserving order parameter in Kagome superconductor CsV_3Sb_5," *Physical Review Letters*, vol. 127, no. 18, p. 187004, 2021.

[23] A. P. Petrović, R. Lortz, G. Santi, C. Berthod, C. Dubois, M. Decroux, A. Demuer, A. B. Antunes, A. Paré, D. Salloum, *et al.*, "Multiband superconductivity in the Chevrel phases $SnMo_6S_8$ and $PbMo_6S_8$," *Physical review letters*, vol. 106, no. 1, p. 017003, 2011.

[24] X. X. Xi, "Two-band superconductor magnesium diboride," *Reports on Progress in Physics*, vol. 71, p. 116501, nov 2008.

[25] M. Zehetmayer, "A review of two-band superconductivity: materials and effects on the thermodynamic and reversible mixed-state properties," *Superconductor Science and Technology*, vol. 26, p. 043001, feb 2013.

[26] A. Shanenko, M. Milošević, F. Peeters, and A. Vagov, "Extended Ginzburg-Landau formalism for two-band superconductors," *Physical review letters*, vol. 106, no. 4, p. 047005, 2011.

[27] S. L. Bud'ko, G. Lapertot, C. Petrovic, C. E. Cunningham, N. Anderson, and P. C. Canfield, "Boron isotope effect in superconducting MgB_2," *Phys. Rev. Lett.*, vol. 86, pp. 1877–1880, Feb 2001.

[28] D. G. Hinks, H. Claus, and J. D. Jorgensen, "The complex nature of superconductivity in MgB_2 as revealed by the reduced total isotope effect," *Nature*, vol. 411, no. 6836, pp. 457–460, 2001.

[29] M. Eskildsen, M. Kugler, G. Levy, S. Tanaka, J. Jun, S. Kazakov, J. Karpinski, and Ø. Fischer, "Scanning tunneling spectroscopy on single crystal MgB_2," *Physica C: Superconductivity*, vol. 385, no. 1-2, pp. 169–176, 2003.

[30] S. Souma, Y. Machida, T. Sato, T. Takahashi, H. Matsui, S.-C. Wang, H. Ding, A. Kaminski, J. Campuzano, S. Sasaki, *et al.*, "The origin of multiple superconducting gaps in MgB_2," *Nature*, vol. 423, no. 6935, pp. 65–67, 2003.

[31] S. A. Kuzmichev, T. E. Kuzmicheva, and S. Tchesnokov, "Determination of the electron-phonon coupling constants from the experimental temperature dependences of superconducting gaps in MgB_2," *JETP Letters*, vol. 99, no. 5, pp. 295–302, 2014.

[32] H. Kim, K. Cho, M. A. Tanatar, V. Taufour, S. K. Kim, S. L. Bud'ko, P. C. Canfield, V. G. Kogan, and R. Prozorov, "Self-consistent two-gap description of MgB_2 superconductor," *Symmetry*, vol. 11, no. 8, 2019.

[33] T. Muranaka and J. Akimitsu, "Superconducitvity in MgB_2," *Z. Kristallogr.*, vol. 226, no. 4, pp. 385–394, 2011.

[34] C. Yang, R. R. Niu, Z. S. Guo, X. W. Cai, H. M. Chu, K. Yang, Y. Wang, Q. R. Feng, and Z. Z. Gan, "Lumped element kinetic inductance detectors based on two-gap MgB_2 thin films," *Applied Physics Letters*, vol. 112, no. 2, p. 022601, 2018.

[35] A. E. Karakozov, E. G. Maksimov, and Y. G. Ponomarev, "Theoretical analysis of tunneling experiments in the MgB_2 system," *JETP Letters*, vol. 91, no. 1, pp. 24–29, 2010.

[36] A. A. Golubov, J. Kortus, O. Dolgov, O. Jepsen, Y. Kong, O. Andersen, B. Gibson, K. Ahn, and R. Kremer, "Specific heat of MgB_2 in a one-and a two-band model from first-principles calculations," *Journal of physics: Condensed matter*, vol. 14, no. 6, p. 1353, 2002.

[37] J. Demsar, R. Averitt, A. Taylor, V. Kabanov, W. Kang, H. Kim, E. Choi, and S. Lee, "Pair-breaking and superconducting state recovery dynamics in MgB_2," *Physical review letters*, vol. 91, no. 26, p. 267002, 2003.

[38] A. J. Leggett, "Number-Phase Fluctuations in Two-Band Superconductors," *Progress of Theoretical Physics*, vol. 36, pp. 901–930, 11 1966.

[39] S. G. Sharapov, V. P. Gusynin, and H. Beck, "Effective action approach to the Leggett's mode in two-band superconductors," *The European Physical Journal B - Condensed Matter and Complex Systems*, vol. 30, no. 1, pp. 45–51, 2002.

[40] G. Blumberg, A. Mialitsin, B. S. Dennis, M. V. Klein, N. D. Zhigadlo, and J. Karpinski, "Observation of Leggett's collective mode in a multiband superconductor," *Physical Review Letters*, vol. 99, nov 2007.

[41] F. Giorgianni, T. Cea, C. Vicario, C. P. Hauri, W. K. Withanage, X. Xi, and L. Benfatto, "Leggett mode controlled by light pulses," *Nature Physics*, vol. 15, no. 4, pp. 341–346, 2019.

[42] A. Wyatt, V. Dmitriev, W. Moore, and F. Sheard, "Microwave-enhanced critical supercurrents in constricted tin films," *Physical Review Letters*, vol. 16, no. 25, p. 1166, 1966.

[43] A. Dayem and J. Wiegand, "Behavior of thin-film superconducting bridges in a microwave field," *Physical Review*, vol. 155, no. 2, p. 419, 1967.

[44] T. Klapwijk, J. Van Den Bergh, and J. Mooij, "Radiation-stimulated superconductivity," *Journal of Low Temperature Physics*, vol. 26, pp. 385–405, 1977.

[45] L. P. GOR'KOV and G. M. ELIASHBERG, "The behavior of a superconductor in a variable field," *Zh. Eksp. Tear. Fiz.*, vol. 55, pp. 2430–2442, December 1968.

[46] I. Rousseau, "Near-resonant pump-probe spectroscopy of superconducting NbN," Master's thesis, University of Konstanz, Feb 2012.

[47] M. Beck, M. Klammer, S. Lang, P. Leiderer, V. V. Kabanov, G. Gol'Tsman, and J. Demsar, "Energy-gap dynamics of superconducting NbN thin films studied by time-resolved terahertz spectroscopy," *Physical Review Letters*, vol. 107, no. 17, p. 177007, 2011.

[48] A. Rothwarf and B. Taylor, "Measurement of recombination lifetimes in superconductors," *Physical Review Letters*, vol. 19, no. 1, p. 27, 1967.

[49] R. Averitt, G. Rodriguez, A. Lobad, J. Siders, S. Trugman, and A. Taylor, "Nonequilibrium superconductivity and quasiparticle dynamics in YBCO," *Physical Review B*, vol. 63, no. 14, p. 140502, 2001.

[50] A. Rothwarf, G. Sai-Halasz, and D. Langenberg, "Quasiparticle lifetimes and microwave response in nonequilibrium superconductors," *Physical Review Letters*, vol. 33, no. 4, p. 212, 1974.

[51] W. H. Parker, "Modified heating theory of nonequilibrium superconductors," *Phys. Rev. B*, vol. 12, pp. 3667–3672, Nov 1975.

[52] W. Parker and W. Williams, "Photoexcitation of quasiparticles in nonequilibrium superconductors," *Physical Review Letters*, vol. 29, no. 14, p. 924, 1972.

[53] W. Parker, "Effective quasiparticle lifetime in superconducting Sn," *Solid State Communications*, vol. 15, no. 6, pp. 1003–1006, 1974.

[54] G. Sai-Halasz, C. Chi, A. Denenstein, and D. Langenberg, "Effects of dynamic external pair breaking in superconducting films," *Physical Review Letters*, vol. 33, no. 4, p. 215, 1974.

[55] A. Rothwarf, "G. a. sai-halasz, and dn langenberg," *Phys. Rev. Letters*, vol. 33, p. 212, 1974.

[56] V. Kabanov, J. Demsar, B. Podobnik, and D. Mihailovic, "Quasiparticle relaxation dynamics in superconductors with different gap structures: Theory and experiments on ybco," *Physical Review B*, vol. 59, no. 2, p. 1497, 1999.

[57] V. V. Kabanov, J. Demsar, and D. Mihailovic, "Kinetics of a superconductor excited with a femtosecond optical pulse," *Physical review letters*, vol. 95, no. 14, p. 147002, 2005.

[58] J. Jorgensen, D. Hinks, and S. Short, "Lattice properties of mgb 2 versus temperature and pressure," *Physical Review B*, vol. 63, no. 22, p. 224522, 2001.

[59] M. Beck, I. Rousseau, M. Klammer, P. Leiderer, M. Mittendorff, S. Winnerl, M. Helm, G. N. Gol'tsman, and J. Demsar, "Transient increase of the energy gap of superconducting NbN thin films excited by resonant narrow-band terahertz pulses," *Physical Review Letters*, vol. 110, no. 26, p. 267003, 2013.

[60] K. Isoyama, N. Yoshikawa, K. Katsumi, J. Wong, N. Shikama, Y. Sakishita, F. Nabeshima, A. Maeda, and R. Shimano, "Light-induced enhancement of superconductivity in iron-based superconductor FeSe0.5Te0.5," *Communications Physics*, vol. 4, no. 1, p. 160, 2021.

[61] L. D. Landau and E. M. Lifshitz, *Quantum mechanics: non-relativistic theory*, vol. 3. Elsevier, 2013.

[62] F. Blanchard, L. Razzari, H.-C. Bandulet, G. Sharma, R. Morandotti, J.-C. Kieffer, T. Ozaki, M. Reid, H. F. Tiedje, H. K. Haugen, and F. A. Hegmann, "Generation of 1.5 μJ single-cycle terahertz pulses by optical rectification from a large aperture ZnTe crystal," *Opt. Express*, vol. 15, pp. 13212–13220, Oct 2007.

[63] Y. Sasaki, A. Yuri, K. Kawase, and H. Ito, "Terahertz-wave surface-emitted difference frequency generation in slant-stripe-type periodically poled linbo3 crystal," *Applied Physics Letters*, vol. 81, no. 18, pp. 3323–3325, 2002.

[64] M. Beck, H. Schäfer, G. Klatt, J. Demsar, S. Winnerl, M. Helm, and T. Dekorsy, "Impulsive terahertz radiation with high electric fields from an amplifier-driven large-area photoconductive antenna," *Opt. Express*, vol. 18, pp. 9251–9257, Apr 2010.

[65] K. Reimann, "Table-top sources of ultrashort THz pulses," *Reports on Progress in Physics*, vol. 70, pp. 1597–1632, sep 2007.

[66] V. A. Andreeva, O. G. Kosareva, N. A. Panov, D. E. Shipilo, P. M. Solyankin, M. N. Esaulkov, P. González de Alaiza Martínez, A. P. Shkurinov, V. A. Makarov, L. Bergé, and S. L. Chin, "Ultrabroad terahertz spectrum generation from an air-based filament plasma," *Phys. Rev. Lett.*, vol. 116, p. 063902, Feb 2016.

[67] H. Roskos, M. Thomson, M. Kreß, and T. Löffler, "Broadband thz emission from gas plasmas induced by femtosecond optical pulses: From fundamentals to applications," *Laser & Photonics Reviews*, vol. 1, no. 4, pp. 349–368.

[68] T. Seifert, S. Jaiswal, U. Martens, J. Hannegan, L. Braun, P. Maldonado, F. Freimuth, A. Kronenberg, J. Henrizi, I. Radu, E. Beaurepaire, Y. Mokrousov, P. M. Oppeneer, M. Jourdan, G. Jakob, D. Turchinovich, L. M. Hayden, M. Wolf, M. Münzenberg, M. Kläui, and T. Kampfrath, "Efficient metallic spintronic emitters of ultrabroadband terahertz radiation," *Nature Photonics*, vol. 10, no. 7, pp. 483–488, 2016.

[69] C. D. Mosley, D. S. Lake, D. M. Graham, S. P. Jamison, R. B. Appleby, G. Burt, and M. T. Hibberd, "Large-area periodically-poled lithium niobate wafer stacks optimized for high-energy narrowband terahertz generation," *Optics Express*, vol. 31, no. 3, pp. 4041–4054, 2023.

[70] K. Y. Kim, A. J. Taylor, J. H. Glownia, and G. Rodriguez, "Coherent control of terahertz supercontinuum generation in ultrafast laser–gas interactions," *Nature Photonics*, vol. 2, no. 10, pp. 605–609, 2008.

[71] A. D. Koulouklidis, C. Gollner, V. Shumakova, V. Y. Fedorov, A. Pugžlys, A. Baltuška, and S. Tzortzakis, "Observation of extremely efficient terahertz generation from mid-infrared two-color laser filaments," *Nature Communications*, vol. 11, no. 1, p. 292, 2020.

[72] K. Miyamoto, S. Ohno, M. Fujiwara, H. Minamide, H. Hashimoto, and H. Ito, "Optimized terahertz-wave generation using bna-dfg," *Opt. Express*, vol. 17, pp. 14832–14838, Aug 2009.

[73] J. Huang, Z. Rao, and F. Xie, "Cascaded dfg via quasi-phase matching with cherenkov-type ppln for highly efficient terahertz generation," *Opt. Express*, vol. 27, pp. 17199–17208, Jun 2019.

[74] M. Beck, *Non-Equilibrium Phenomena in Conventional and High-Temperature Superconductors Probed by Time-Domain Terahertz-Spectroscopy Non-Equilibrium Phenomena in Conventional and High-Temperature Superconductors Probed by Time-Domain Terahertz-Spectroscopy*. PhD thesis, University of Konstanz, December 2013.

[75] B. B. Hu, J. T. Darrow, X.-C. Zhang, D. H. Auston, and P. R. Smith, "Optically steerable photoconducting antennas," *Applied physics letters*, vol. 56, no. 10, pp. 886–888, 1990.

[76] C. Bull, S. M. Hewett, R. Ji, C.-H. Lin, T. Thomson, D. M. Graham, and P. W. Nutter, "Spintronic terahertz emitters: Status and prospects from a materials perspective," *APL Materials*, vol. 9, no. 9, p. 090701, 2021.

[77] A. A. Kolokolov, "Fresnel formulas and the principle of causality," *Phys. Usp.*, vol. 42, no. 9, p. 931, 1999.

[78] S. Kovalev, T. Dong, L.-Y. Shi, C. Reinhoffer, T.-Q. Xu, H.-Z. Wang, Y. Wang, Z.-Z. Gan, S. Germanskiy, J.-C. Deinert, I. Ilyakov, P. H. M. van Loosdrecht, D. Wu, N.-L. Wang, J. Demsar, and Z. Wang, "Band-selective third-harmonic generation in superconducting MgB_2: Possible evidence for the Higgs amplitude mode in the dirty limit," *Phys. Rev. B*, vol. 104, p. L140505, Oct 2021.

[79] H. M. Bretscher, P. Andrich, Y. Murakami, D. Golež, B. Remez, P. Telang, A. Singh, L. Harnagea, N. R. Cooper, A. J. Millis, P. Werner, A. K. Sood, and A. Rao, "Imaging the coherent propagation of collective modes in the excitonic insulator Ta2NiSe5 at room temperature," *Science Advances*, vol. 7, no. 28, p. eabd6147, 2021.

[80] J. Graf, C. Jozwiak, C. L. Smallwood, H. Eisaki, R. A. Kaindl, D.-H. Lee, and A. Lanzara, "Nodal quasiparticle meltdown in ultrahigh-resolution pump–probe angle-resolved photoemission," *Nature Physics*, vol. 7, no. 10, pp. 805–809, 2011.

[81] J. Schmidt, S. Winnerl, E. Dimakis, R. Hübner, H. Schneider, and M. Helm, "All-thz pump-probe spectroscopy of the intersubband ac-stark effect in a wide gaas quantum well," *Optics Express*, vol. 28, no. 17, pp. 25358–25370, 2020.

[82] M. Helm, "Semiconductor spectroscopy using thz free-electron lasers," in *2013 38th International Conference on Infrared, Millimeter, and Terahertz Waves (IRMMW-THz)*, pp. 1–2, IEEE, 2013.

[83] C. Zhang, Y. Wang, D. Wang, Y. Zhang, Q.-R. Feng, and Z.-Z. Gan, "Hybrid physical - chemical vapor deposition of ultrathin MgB_2 films on MgO substrate with high T_c and J_c," *IEEE Transactions on Applied Superconductivity*, vol. 23, no. 3, pp. 7500204–7500204, 2013.

[84] M. Eichberger, H. Schäfer, M. Krumova, M. Beyer, J. Demsar, H. Berger, G. Moriena, G. Sciaini, and R. Miller, "Snapshots of cooperative atomic motions in the optical suppression of charge density waves," *Nature*, vol. 468, no. 7325, pp. 799–802, 2010.

[85] M. Beck, M. Klammer, I. Rousseau, M. Obergfell, P. Leiderer, M. Helm, V. Kabanov, I. Diamant, A. Rabinowicz, Y. Dagan, *et al.*, "Melting the superconducting state in the electron doped cuprate $Pr_{1.85}Ce_{0.15}CuO_{4-\delta}$ with intense near-infrared and terahertz pulses," *arXiv preprint arXiv:1603.04155*, 2016.

[86] M. Beck, M. Klammer, I. Rousseau, M. Obergfell, P. Leiderer, M. Helm, V. V. Kabanov, I. Diamant, A. Rabinowicz, Y. Dagan, *et al.*, "Energy dependence of the electron-boson coupling strength in the electron-doped cuprate superconductor $Pr_{1.85}Ce_{0.15}CuO_{4-\delta}$," *Physical Review B*, vol. 95, no. 8, p. 085106, 2017.

[87] G. Blumberg, A. Mialitsin, B. Dennis, N. Zhigadlo, and J. Karpinski, "Multi-gap superconductivity in MgB_2: Magneto-raman spectroscopy," *Physica C: Superconductivity*, vol. 456, no. 1-2, pp. 75–82, 2007.

[88] W. Li, Y. Li, R. Chen, R. Zeng, M. Zhu, H. Jin, and S. Dou, "Electron–phonon coupling properties in MgB_2 observed by raman scattering," *Journal of Physics: Condensed Matter*, vol. 20, no. 25, p. 255235, 2008.

[89] A. R. Pokharel, S. Y. Agustsson, V. V. Kabanov, F. Iga, T. Takabatake, H. Okamura, and J. Demsar, "Robust hybridization gap in the Kondo insulator YbB_{12} probed by femtosecond optical spectroscopy," *Phys. Rev. B*, vol. 103, p. 115134, 2021.

[90] C. Kittel, *Introduction to solid state physics*. John Wiley & Sons, Inc., eighth edition ed., 2005.

[91] R. A. Kaindl, M. A. Carnahan, J. Orenstein, D. S. Chemla, H. M. Christen, H.-Y. Zhai, M. Paranthaman, and D. H. Lowndes, "Far-infrared optical conductivity gap in superconducting MgB_2 films," *Physical review letters*, vol. 88, no. 2, p. 027003, 2001.

[92] J. Fiore, M. Udina, M. Marciani, G. Seibold, and L. Benfatto, "Contribution of collective excitations to third harmonic generation in two-band superconductors: The case of MgB_2," *Physical Review B*, vol. 106, no. 9, p. 094515, 2022.

[93] P. Peumans, A. Yakimov, and S. R. Forrest, "Small molecular weight organic thin-film photodetectors and solar cells," *Journal of Applied Physics*, vol. 93, no. 7, pp. 3693–3723, 2003.

[94] Y. R. Koh, J. Shi, B. Wang, R. Hu, H. Ahmad, S. Kerdsongpanya, E. Milosevic, W. A. Doolittle, D. Gall, Z. Tian, *et al.*, "Thermal boundary conductance across epitaxial metal/sapphire interfaces," *Physical Review B*, vol. 102, no. 20, p. 205304, 2020.

[95] J. Chen, X. Xu, J. Zhou, and B. Li, "Interfacial thermal resistance: Past, present, and future," *Reviews of Modern Physics*, vol. 94, no. 2, p. 025002, 2022.

LIST OF FIGURES

Acknowledgments

Removed in the electronic version of this thesis due to data protection regulations.
In der elektronischen Version entfernt aufgrund datenschutzrechtlicher Bestimmungen.

PUBLICATIONS LIST

1. **S. Sobolev**, A. Lanz, T. Dong, A.R. Pokharel, V. Kabanov, Z.Z. Gan, L.Y. Shi, N.L. Wang, A. Pashkin, S. Winnerl, M. Helm, and J. Demsar. Time-resolved Studies of the Energy Gap Dynamics of Superconducting MgB_2Thin Films Excited by Resonant Narrow-Band Terahertz Pulses. *in preparation with coauthors, to be submitted in Phys. Rev. Lett.*

2. Vladimir Grigorev, Mariia Filianina, Yaryna Lytvynenko, **Sergei Sobolev**, Amrit Raj Pokharel, Amon P. Lanz, Alexey Sapozhnik, Armin Kleibert, Stanislav Bodnar, Petr Grigorev, Yurii Skourski, Mathias Kläui, Hans-Joachim Elmers, Martin Jourdan, and Jure Demsar. Optically Triggered Néel Vector Manipulation of a Metallic Antiferromagnet Mn_2Au under Strain. *ACS Nano*, vol. 16, no. 12, pp. 20589–20597, 2022.

3. V. Grigorev, M. Filianina, S. Yu. Bodnar, **S. Sobolev**, N. Bhattacharjee, S. Bommanaboyena, Y. Lytvynenko, Yurii Skourski, D. Fuchs, M. Kläui, M. Jourdan, J. Demsar. Optical Readout of the Néel Vector in the Metallic Antiferromagnet Mn_2Au. *Phys. Rev. Applied* **16**, 014037 (2021).

4. A.F. Kornev, A.S. Davtian, A.S. Kovyarov, A.M. Makarov, D.O. Oborotov, V.P. Pokrovskii, A.A. Porozov, **S. S. Sobolev**, V.K. Stupnikov, G.S. Kurskiev, E.E. Mukhin, S.Yu.Tolstyakov, P. Andrew, M. Kempenaars, G. Vayakis, M. Walsh. Nd:YAG lasers for ITER divertor Thomson scattering. Fusion Engineering and Design, **146**, Part A, (2019)

Curriculum Vitae

Removed in the electronic version of this thesis due to data protection regulations.
In der elektronischen Version entfernt aufgrund datenschutzrechtlicher Bestimmungen.